1994

An investigation of the image edit and reconstruct technique using non-uniform point source targets

Robert Anthony Clemens
University of Dayton

AN INVESTIGATION OF THE IMAGE EDIT AND RECONSTRUCT TECHNIQUE USING NON-UNIFORM POINT SOURCE TARGETS

Thesis

Submitted to the School of Engineering of the

UNIVERSITY OF DAYTON

In Partial Fulfillment of the Requirements of

The Degree

Master of Science in Electrical Engineering

by

Robert Anthony Clemens

UNIVERSITY OF DAYTON

Dayton, Ohio

August 1994

AN INVESTIGATION OF THE IMAGE EDIT AND RECONSTRUCT TECHNIQUE USING NON-UNIFORM POINT SOURCE TARGETS.

Approved by:

[redacted]

Gary A. Thiele, Ph.D.
Tait Professor of Electrical Engineering
Committee Chairperson

[redacted]

Krishna M. Pasala, Ph.D.
Associate Professor of Electrical Engineering
Committee Member

[redacted]

Richard J. Kee, D. Eng ., P.E.
Assistant Professor of Electrical Engineering
Committee Member

[redacted]

Donald L. Moon, Ph.D.
Associate Dean
Graduate Engineering & Research
School of Engineering

[redacted]

Joseph Lestingi, D. Eng., P.E.
Dean
School of Engineering

ABSTRACT

AN INVESTIGATION OF THE IMAGE EDIT AND RECONSTRUCT TECHNIQUE USING NON-UNIFORM POINT SOURCE TARGETS.

Clemens, Robert Anthony
University of Dayton, 1994

Advisor: Dr. G.A. Thiele

The technique referred to as image edit and reconstruct (IER) is a post processing procedure used to minimize the errors due to background sources in a radar cross section (RCS) measurement. This report rigorously examines the errors associated with the technique in three steps. First, the principles of RCS measurements and imaging are introduced with an emphasis on the uniform point source scattering behavior assumption used in the imaging algorithm. Second, the IER technique is developed mathematically and it is shown that two error sources are always present in the resulting RCS data. Third, the technique is examined analytically using synthetic scattering sources other than uniform point sources and the magnitudes of the resulting errors vary widely. The report draws two major conclusions. 1) Analyses of the technique with uniform point source targets are not adequate for determining general limitations and guidelines for its proper use. 2) The technique is useful for reducing the effects of unwanted background sources in an RCS measurement, but due to the varying and unpredictable error magnitude observed in the analysis, the technique is not recommended for absolute signature measurements.

ACKNOWLEDGMENTS

My foremost thanks goes to Dr. Frederick A. Tokarz of the Defensive Avionics Branch, Aeronautical Systems Center, Wright-Patterson AFB, OH for the generous aid provided throughout this project. My thanks to him especially for helping to instill in me the motivation and confidence to bring this work to a close.

I thank Dr. Gary A. Thiele, my advisor, for supporting the research and leading me through the university's process. Thanks also go to the two other committee members, Dr. Krishna M. Pasala and Dr. Richard J. Kee.

I would like to express my appreciation to Dr. Brian M. Kent of the Signature Technology Office, Wright Laboratories, Wright-Patterson AFB, OH for the technical discussions that helped to finalize the topic of research.

Finally, I wish to acknowledge the support of my wife, Ann. Had it not been for her patience and understanding, I would never have finished. In gratitude, I promise to her and my daughter Kristen, that I will repay the attention they lost while I completed this thesis.

TABLE OF CONTENTS

APPENDICES

LIST OF ILLUSTRATIONS

LIST OF TABLES

INTRODUCTION

To introduce the topic of research for this thesis, a background section is provided followed by the problem statement.

Background

As low radar cross section (RCS) technology has advanced, the need for high quality, accurate RCS measurements has become increasingly important. During the development of a low RCS vehicle, each radar scattering component of the vehicle must be accounted for to assure the aggregate vehicle radar signature is at or below its maximum allowable value. These component RCS measurements require the use of a test fixture which must meet two conditions: First, it must accurately simulate the surrounding vehicle structure in material and form and second, it must not contribute appreciably to the measured RCS. The acceptable contribution of the test fixture varies with each application. Conservative measurements use a test fixture at least 20 dB (decibels) below the target RCS but some in the industry accept a 10 dB separation. As technology advances and vehicle RCS levels decrease, the component signatures must also decrease, so meeting the second test fixture condition is increasingly difficult and expensive. It becomes a complex development in itself to design and build low RCS test fixtures for component measurements.

An alternative component RCS measurement technique called IER (image edit and reconstruct) has been proposed by some with limited documentation. The technique

involves three basic steps. First, the scattered field of the target mounted in the test fixture is measured and processed to form an image. Second, the image is edited to remove scattering sources located outside the target area. Third, the edited image is reverse processed and interpreted as the scattered field of the target without the test fixture. The references [1,2,3,4] provide demonstrations of the technique on limited cases with general guidelines for its use but there are still open issues related to its potential errors and limitations.

Problem Statement

A technique has been proposed in the RCS measurement community to use IER to determine the RCS of a target on a test fixture with little or no separation between the RCS of the target and the test fixture. The references [1,2,3,4] provide general guidelines for use of the technique and demonstrate its usefulness with point source type scatterers, but they do not adequately address the limitations imposed by non-ideal scatters. This paper attempts to examine the validity of the IER technique when used with various non-ideal sources and to develop further understanding of the technique's limitations.

In an effort to thoroughly analyze the problem, the paper is arranged as follows. First, an overview of RCS measurements and imaging is presented which includes general concepts and definitions, basic techniques for obtaining two dimensional resolution, and other processing considerations related to the IER technique. Second, the image edit and reconstruct algorithm is presented and includes a mathematical development of the technique and a review of previous work. Third, is an analysis section. This section forms the bulk of the paper and examines the results of an analysis of the technique when used with various non-ideal sources. Fourth, conclusions of the paper are presented, and finally, recommendations for future work close the report.

CHAPTER 1

RCS MEASUREMENTS AND IMAGING

In order to understand the Image Edit and Reconstruct Technique, background information is required on RCS measurements and image processing.

Basics of RCS Measurements

The RCS "relates the transmitted power to the power reradiated by a target in the direction of the receiver [5]." It is a function of radar frequency, angle of incidence, and polarization. By definition, the RCS of a target is given as [6]:

$$\sigma = \lim_{r \to \infty} 4\pi r^2 \left| \frac{E_s}{E_i} \right|^2 \tag{1}$$

where,

r = range to the target in meters

E_s = far field scattered electric field in volts/meter

E_i = incident electric field in volts/meter

In this equation, the incident field is a plane wave and the scattered field has a range dependence of $\exp\{-jkr\}/r$, ($\exp\{j\omega t\}$ dependence is assumed) so a new variable $\tilde{E}_s$, is defined which is range independent:

$$\tilde{E}_s = r \exp\{jkr\} E_s \tag{2}$$

where,

$k = 2\pi f/c$ = propagation constant in rad/m

f = frequency in Hz

c = propagation velocity in meters/sec.

$\tilde{E}_s$ now has the units of volts and represents the reflected voltage at the target. With this range independent parameter, the scattered field from the target at any far-field range is easily calculated from (2).

When making RCS measurements, a calibration standard is needed whose range independent scattered field $\tilde{E}_s^{cal,exact}$, is known (or calculated) exactly to within a required accuracy. The typical calibration standard used is a sphere since its RCS is aspect independent and is easily calculated with an eigenfunction series. The radar receiver measures the scattered fields of the calibration standard $E_s^{cal,meas}$, and the target $E_s^{tar,meas}$ from which the target's calibrated, range independent scattered field $\tilde{E}_s^{tar}$, (assuming no background subtraction) is derived with:

$$\tilde{E}_s^{tar} = \frac{E_s^{tar,meas}}{E_s^{cal,meas}} \cdot \tilde{E}_s^{cal,exact} \tag{3}$$

Using (2) and (3) in (1), the target RCS is calculated with:

$$\sigma^{tar} = 4\pi \left| \tilde{E}_s^{tar} \right|^2 . \tag{4}$$

In general, $|E_i|^2$ should appear in the denominator of (4), but it does not since the calculation of the calibration target's exact field usually assumes $|E_i| = 1.0$. Equations (3) and (4) can also be combined to give:

$$\sigma^{tar} = 4\pi \left| \frac{E_s^{tar,meas}}{E_s^{cal,meas}} \right|^2 \left| \tilde{E}_s^{cal,exact} \right|^2 = \left| \frac{E_s^{tar,meas}}{E_s^{cal,meas}} \right|^2 \sigma^{cal,exact} . \tag{5}$$

Using (5) is sufficient for calculating the RCS of the target which is a real valued term, but the coherency derived from the calculation of $\tilde{E}_s^{tar}$ in (3) is lost. As discussed later, coherent data is required to process an image. Within equations (1) through (5), the functional dependence of the scattered field and the RCS on frequency, polarization, and aspect angle is not explicitly shown to simplify the equations. Awareness of this dependence is important, however, especially when examining (3) and (5). What these equations say is that every change in frequency, polarization, or aspect angle requires a new (and unique) calibration.

RCS data is typically presented in one of two formats: RCS vs. angle at a fixed frequency (e.g., Figure 1) or RCS vs. frequency at a fixed angle. As long as each data point is calibrated per (5) the absolute RCS of the target in either format is preserved [7]. In the case of measuring the RCS of a target mounted on a test fixture, the calibrated RCS resulting from the implementation of (5) is a combination of three scattering sources: the target, the test fixture, and interactions between the target and test fixture. Proper test fixtures are designed to minimize the impacts of the latter two scattering sources to the measured RCS. To determine an acceptable separation between the target and test fixture RCS the assumption of coherent summation of scatterers is used. In this way, error estimates are expressed in terms of the maximum and minimum as given by perfect constructive and destructive interference, respectively [8]. Figure 2 provides a plot of this error as a function of background-to-target separation in dB, where the background in this case is the returns of the test fixture and the interactions. From the figure, it is seen that a 10 dB separation introduces errors from -3.3 dB to +2.4 dB, and a 20 dB separation gives errors from -0.9 to +0.8 dB. The errors for the 20 dB separation are used as a benchmark in the analysis section.

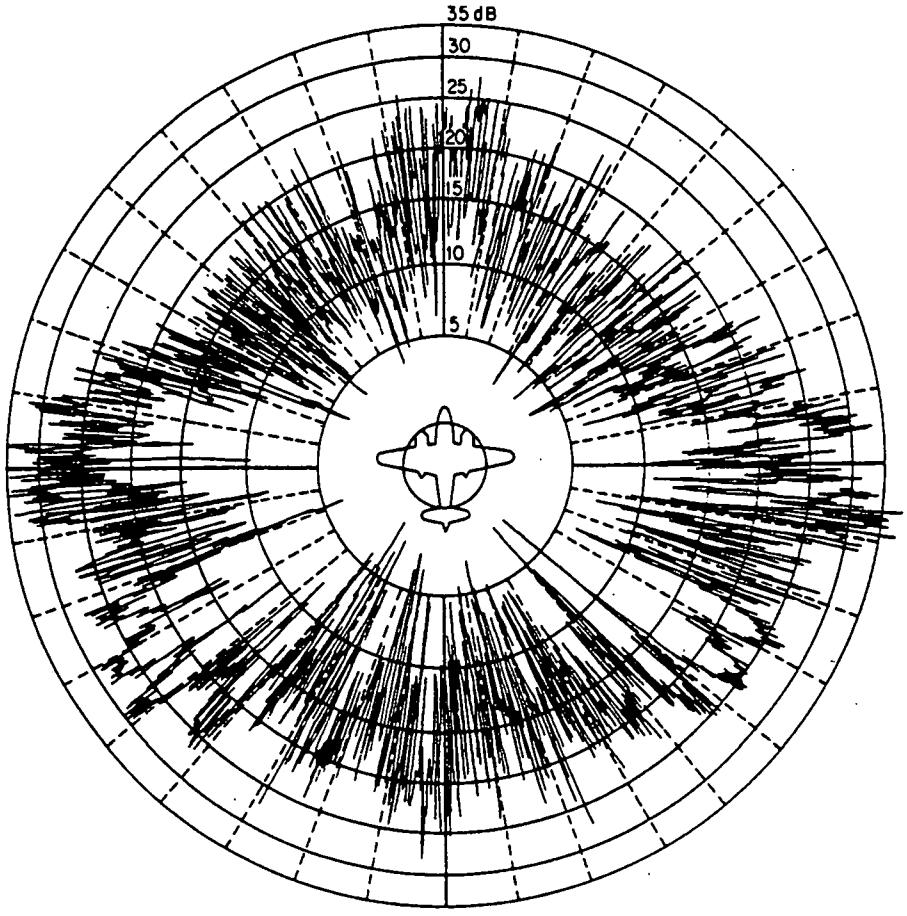

Figure 1.

Experimental RCS of the B-26 Bomber at 3 GHz as a Function of Azimuth Angle [9].

RCS Imaging

A definition of an RCS image is, "the spatial distribution of reflectivity corresponding to the object [11]." The measure of the ability provided by an image to distinguish scattering sources from those nearby is called *resolution.* Images provide range resolution in one or more dimensions. In most cases, images are two dimensional (2-D), meaning scatterers are resolvable in both down range and cross range. Figure 3 provides a 2-D RCS image example of a target presented in two amplitude formats.

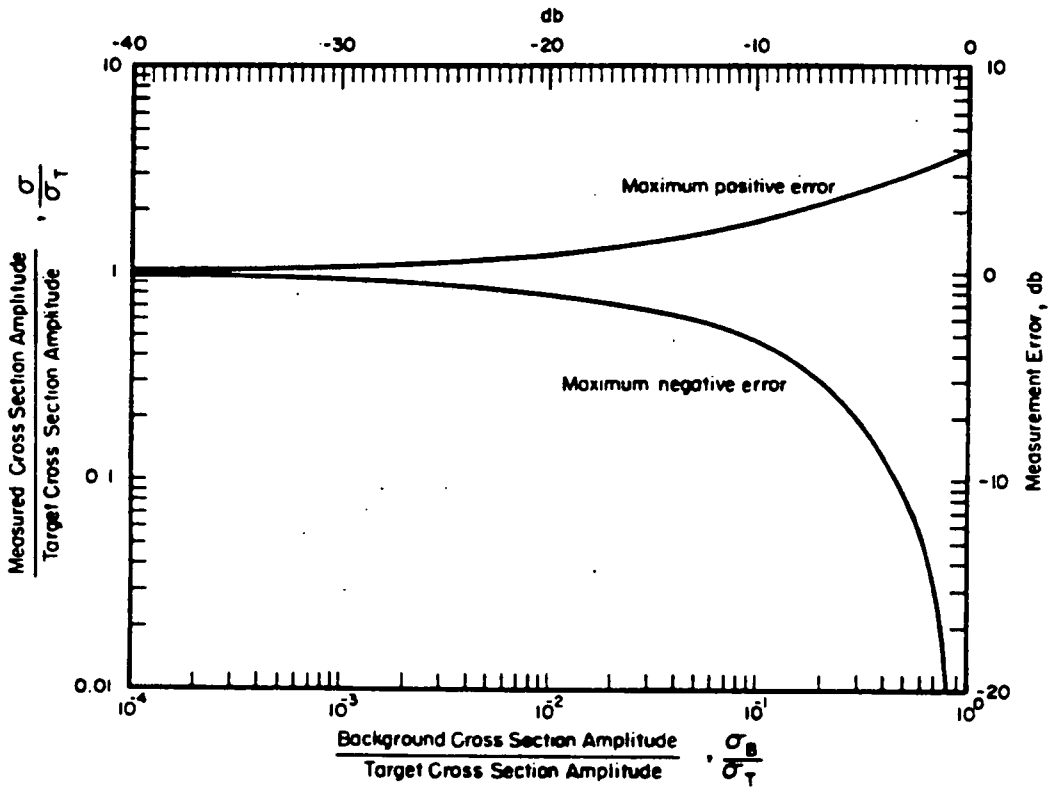

Figure 2

Measurement Error as a Function of Background to Target RCS Amplitudes [10].

Calculated image amplitude units are volts, but images are most often displayed on a logarithmic scale as is the case for both formats of Figure 3. One dimensional (1-D) images are also frequently used and typically provide resolution in down range only, but can also be formed with resolution in cross range only. The domain of the image is often referred to as the *spatial domain*, since scattering centers are spatially resolvable. Obtaining spatial resolution is achieved through processing of scattered field data measured in the *spectral domain* (frequency and aspect angle). The spatial domain is not a format for presenting absolute RCS data. This is strictly limited by the definition of RCS given in (1) to the spectral domain, since the RCS is a function of frequency, aspect

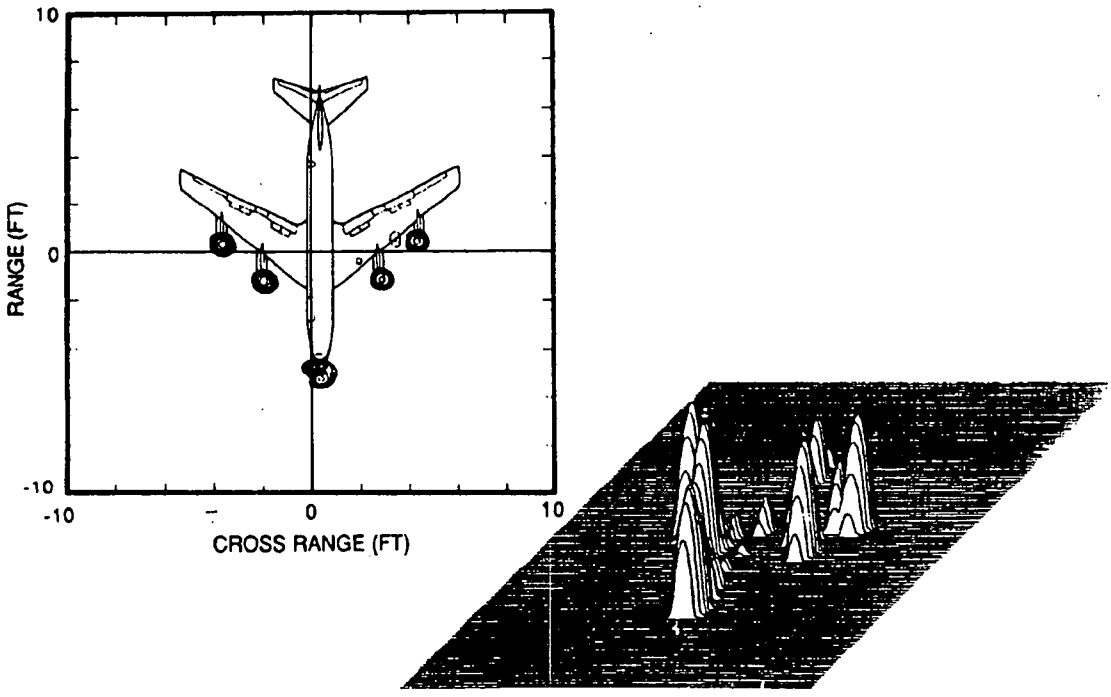

Figure 3

15 GHz Image at 1:10 Scale Model Viewed from Front Aspect [12].

angle, and polarization. A description of the processing involved in deriving down range and cross range resolution follows.

Down Range Processing

Down range resolution is classically derived by measuring the time delay between the scattering sources of the target. The simplest system for performing this measurement is a pulsed radar where the leading and trailing edges of the pulse provide time references to measure the delay. For a source at a range R, the propagation delay from the radar to the target and back is given by $\Delta t = 2R/c$, where c is still the velocity of propagation. Therefore, a pulse of length T, is equivalent to a range separation (or resolution) of

$\Delta R = cT/2$. For a matched filter, the bandwidth of the radar B, is equal to $1/T$, and the resolution equation becomes:

$$\Delta R = c/2B. \tag{6}$$

Obtaining range resolution in this manner is easy to understand, but it becomes impractical when high resolution (i.e., large bandwidth) is required. An alternative, more practical method is to use discrete Fourier Transform (DFT) processing of the target's scattering measured at discrete frequencies. This technique is discussed next and is the one used to create images in the analysis section.

For a description of how down range resolution is obtained with DFT processing, imagine, as shown in Figure 4, a radar viewing a target comprised of an array of point sources. If the array is divided into N total range cells, the measured range independent scattered field (after calibration in accordance with (3)) as a function of frequency is given as:

$$\tilde{E}_s^{tar}(f) = \sum_{n=-N/2}^{N/2-1} a(r_n)\exp\{-j4\pi f r_n/c\} \tag{7}$$

where,

f = frequency in Hz

$a(r_n)$ = range independent scattering strength in volts of contributors in the n^{th} range cell

r_n = distance from radar to the n^{th} range cell in meters (r_0 is at the center of the target).

The appearance of r_n in (7), may lead one to believe the scattered field is not the range independent version, but in fact it is, since the range appears in the argument of the

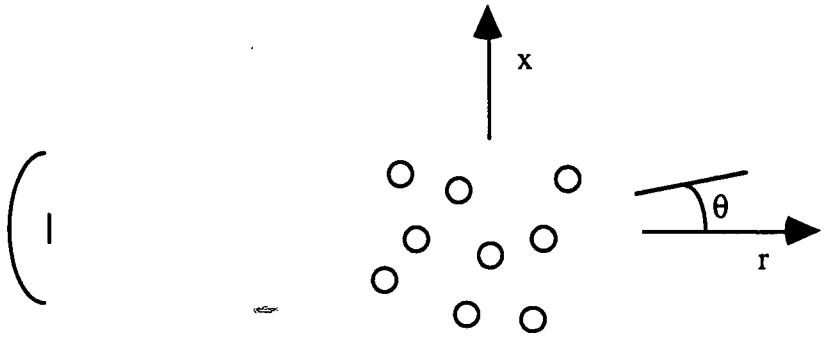

Figure 4

Illustration of Radar Viewing An Array of Point Sources.

exponent only to assure proper phasor addition of the range cell returns referenced to the center of the target. Now, if the scattered field is measured over N discrete frequencies each separated by Δf, and we use the symbols $f_k = k\Delta f$ (where k is indexed from $-N/2$ to $N/2-1$) and $t_n = 2r_n/c = n\Delta t$, (7) becomes:

$$\tilde{E}_s^{tar}(f_k) = \sum_{n=-N/2}^{N/2-1} a(t_n)\exp\{-j2\pi f_k t_n\} \tag{8}$$

Notice, t_n corresponds to the time segment given by the range r_n and Δt is the time domain resolution. To this point the resolution is arbitrary, so if we let

$$\Delta t = 1/(N\Delta f), \tag{9}$$

then $f_k t_n = kn/N$ and (8) can be arranged as:

$$\tilde{E}_s^{tar}[k] = \sum_{n=-N/2}^{N/2-1} a[n]\exp\{-j2\pi kn/N\} \tag{10}$$

Which is nearly the DFT sum. (Note: brackets are used to indicate a discrete series). To force the relation to a DFT sum, we need only to multiply the right side of (10) by $1/N$.

So the DFT relationship between time domain cell scattering strength $a[n]$ and frequency domain measured range independent scattering strength $\tilde{E}_s^{tar}[k]$ is:

$$\tilde{E}_s^{tar}[k] = N \cdot DFT\{a[n]\} \tag{11}$$

The coefficients, $a[n]$ calculated with (11) approximate the impulse response of the function $\tilde{E}_s^{tar}[k]$. For the impulse response, $h(t)$ the approximation is:

$$a[n] \approx h(t_k)\Delta t.$$

For this reason, the calculated coefficients are often displayed as the impulse response of the target. The plots provided in the analysis section of this report use this convention.

The resolution in time derived with this relation is given directly from (9), and since $B = N\Delta f$ the resolution is

$$\Delta t = 1/B. \tag{12}$$

In terms of down range, the resolution is given as:

$$\Delta r = c/2B \tag{13}$$

which is identical to the relation derived above for the pulsed radar. Notice that the range independent scattered field is used to calculate the time domain coefficients, not the RCS. Often, the RCS and time domain response are grouped as Fourier Transform pairs but this derivation demonstrates they are not.

Cross Range Processing

The development of the theory behind obtaining cross range resolution is similar to that of down range, but while down range resolution is obtained through processing of frequency data, cross range resolution is achieved by processing aspect angle data. As

with the down range development, a somewhat classical method of obtaining resolution is presented first with the development of a more practical method following.

It is known in antenna theory that a beam from a uniform aperture has a peak-to-null beamwidth of $\lambda r/D$ radians, where λ is wavelength, r is the range to the target, and D is the lateral dimension of the aperture [13]. Therefore, if this beam is swept across a target, adjacent scatterers in a plane normal to the direction of the antenna are resolvable if their separation is equivalent to or greater than this beamwidth. This equates to the Rayleigh resolution criterion applied in optical systems [14]. To obtain fine resolution with this method, then, requires a large aperture which is often impractical. A method to overcome this, is to sample the radar returns of the target with a smaller aperture as it is moved along the contour of the desired large aperture. This effectively synthesizes the large aperture and thus the name synthetic aperture radar or SAR. There are three general forms of SAR: In linear SAR the synthesized antenna forms a straight line. In spotlight SAR it forms an arc around the target, and in inverse SAR (ISAR) the antenna remains still and the target rotates. In a clutter free environment, data from SAR and ISAR measurements are mathematically equivalent. This paper does not address linear SAR since spotlight SAR and ISAR provide better resolution and are the preferred techniques in most applications.

Similar to down range, processing SAR data into a cross range image can be accomplished with DFTs. Refer back to Figure 4 which illustrates a radar viewing a target comprised of an array of point sources. If the array is now divided into M total cross range cells, the measured range independent scattered field as a function of angle is given as:

$$\tilde{E}_s^{tar}(\theta) = \sum_{m=-M/2}^{M/2-1} b(x_m)\exp\{+j4\pi \sin\theta x_m f/c\} \tag{14}$$

where,

$b(x_m)$ = range independent scattering strength in volts of contributors in the mth cross range cell

x_m = distance from radar to the mth range cell in meters (x_0 is at the center of the target).

Since $R_0 >> x_m$ for most applications we can use the small angle approximation $\sin\theta \approx \theta$. Also, if the scattered field is measured over M discrete angles each separated by $\Delta\theta$, and we use the symbols $\theta_l = l\Delta\theta$ (where l is indexed from $-M/2$ to $M/2-1$) and $\delta_m = 2x_m f/c = m\Delta\delta$, (14) becomes:

$$\tilde{E}_s^{tar}(\theta_l) = \sum_{m=-M/2}^{M/2-1} b(\delta_m)\exp\{j2\pi\theta_l\delta_m\} \tag{15}$$

Notice, δ_m corresponds to the angular Doppler frequency (or measure of phase change as a function of angle θ) of the return at the cross range location x_m and $\Delta\delta$ is the Doppler frequency domain resolution. To this point the resolution is arbitrary, so if we let

$$\Delta\delta = 1/(M\Delta\theta), \tag{16}$$

then $\theta_l\delta_m = lm/M$ and (15) can be arranged as:

$$\tilde{E}_s^{tar}[l] = \sum_{m=-M/2}^{M/2-1} b[m]\exp\{j2\pi lm/M\} \tag{17}$$

Which is the inverse DFT sum. So the DFT relationship between Doppler frequency domain cell scattering strength $b[m]$ and the spectral domain (vs. angle) measured range independent scattering strength $\tilde{E}_s^{tar}[l]$ is:

$$\tilde{E}_s^{tar}[l] = DFT^{-1}\{b[m]\} \tag{18}$$

The resolution in Doppler frequency derived with this relation is given directly from (16), and if we let the total angular extent be given as $\Theta = M\Delta\theta$ the resolution is

$$\Delta\delta = 1/\Theta$$

or in terms of cross range, it is given as:

$$\Delta x = \lambda/2\Theta \tag{19}$$

which is not identical to the Rayleigh resolution provided with a real aperture. With the small angle approximation for a real aperture, $\Theta \approx D/r$ and the Rayleigh resolution is $\Delta x = \lambda/\Theta$, which is twice that obtained with a synthetic aperture. Therefore, a synthetic aperture only needs to be half the length of a real aperture to provide identical resolution.

Clearly, down range and cross range processing are very similar. Creating a 2-D image is simply a linear combination of these two similar processes on wideband, synthetic aperture data. For example, a target's range independent scattered field is measured at N frequencies over M aspect angles. A range profile of length N is then calculated using (11) at each aspect angle. These range profiles are then used in place of $\tilde{E}_s^{tar}[l]$ in (18) to process cross range profiles at each down range location.

It is important to recognize a major assumption used in the development of all down range and cross range processing algorithms is that all scattering source returns behave as a uniform point source. There are two implications to this assumption. First, it implies that the scattered fields within an image cell do not vary with frequency or angle. Of course this is not true and correct interpretation of an image requires knowledge of how non-ideal sources behave in the spatial domain. Second, the assumption implies that all range independent scattered fields are real (i.e., no phase component). For some perfect conductors, this is true, but for any source with a complex impedance, the range

independent scattered field has a non-zero phase component. The analysis section of this report addresses the behavior of a few non-ideal sources.

Additional Image Processing

The previous section described RCS image generation as basically DFT processing of wideband synthetic aperture data. While this does create an image, additional processing of the data usually occurs to "clean-up" the image.

The spectral domain files are often zero padded before DFT processing to increase the *granularity* in the spatial domain. Granularity describes the sample spacing in the spatial domain and can always be improved by increasing the sample space extent in the spectral domain. For a 1-D down range image, the granularity in time is given as:

$$\Delta g = 1/B_z \tag{20}$$

where B_z is the bandwidth after zero padding.

Windows or weighting functions are often applied to the spectral domain data to reduce the leakage in the spatial domain associated with processing a DFT over a finite interval. By tapering the spectral domain data to zero at the endpoints, weighting functions provide a more continuous transition and thus reduce the Gibb's phenomena in the spatial domain. There is an analogy in antenna theory with the use of tapered currents to reduce the sidelobes in the radiation pattern from those associated with a uniform current source. Numerous weighting functions are available and are listed in [15] but the most frequently used in RCS imaging are the Hann (also called Hanning) and Hamming windows due to their computational simplicity. The weighting function selection is generally dictated by tradeoffs between three spatial domain parameters: resolution,

sidelobe level, and sidelobe falloff. These parameters along with others for numerous weighting functions are available in [15]. Weighting functions are discussed more in the mathematical development of the image edit and reconstruct algorithm and in the analysis section.

Focusing of the image is often performed if large aperture angles (>10°) are used to process cross range profiles. The necessity for and implementation of is easily described with the illustration in Figure 5. Using ISAR or spotlight SAR, the available frequency samples extend radially outward for each angle, but DFT processing assumes the samples are on a rectangular grid. If the radial samples are used in the image generation, then smearing occurs in the spatial domain. But if the available samples are interpolated to a rectangular grid, the smearing is removed or the image is focussed. Simply put, the focusing algorithm interpolates the sampled data and resamples it such that it appears the range to the target was infinite. Figure 6 presents an example of a data set processed without and with focusing.

The implementation of a *zero Doppler filter* is sometimes used to reduce the effects of clutter in the image with ISAR measurements. In last section it was shown how the cross range profiles are derived from angular Doppler frequency measurements. With ISAR measurements, only the target is moving, so clutter responses from the environment have no Doppler shift and can be eliminated with a filter. This technique is not applicable to SAR measurements since the motion of the radar induces a Doppler shift on the scattering from all sources, whether target or background.

One final processing technique is the *near-to-far field transformation.* Imaging assumes a plane wave incident field on the target. When the incident field is not a plane

wave, two problems occur. First, 2-D images are warped due to the curved phase front of the field. Second, amplitude errors occur in the down range due to the $1/R^2$ fall off in field strength. These two problems are minimal when measurements are made in the far-field and are usually corrected with techniques like those presented in [18] when near-field measurements are made.

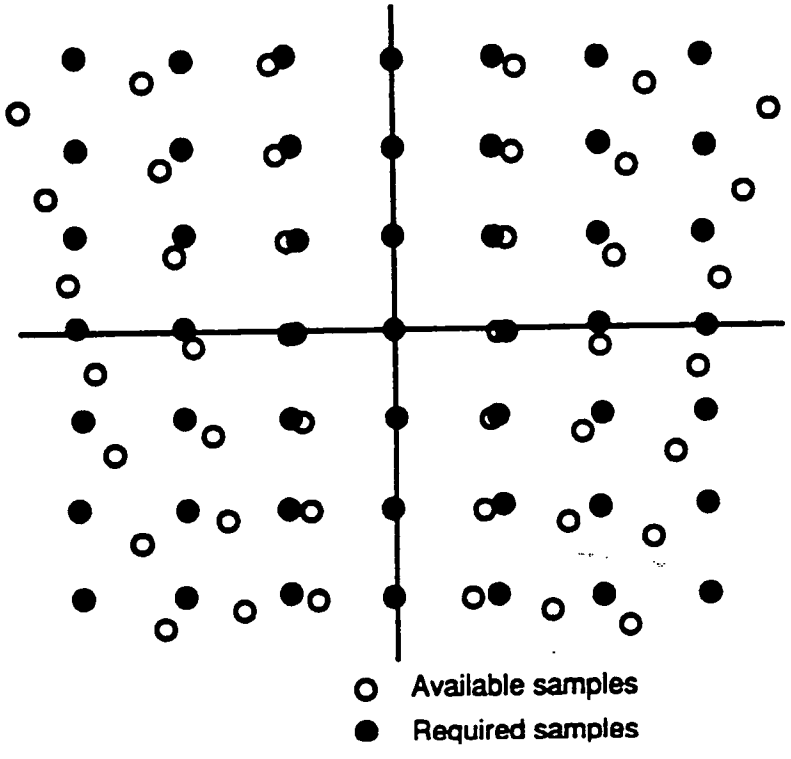

Figure 5

Raster of Available Polar and Required Rectangular Sample Locations [16].

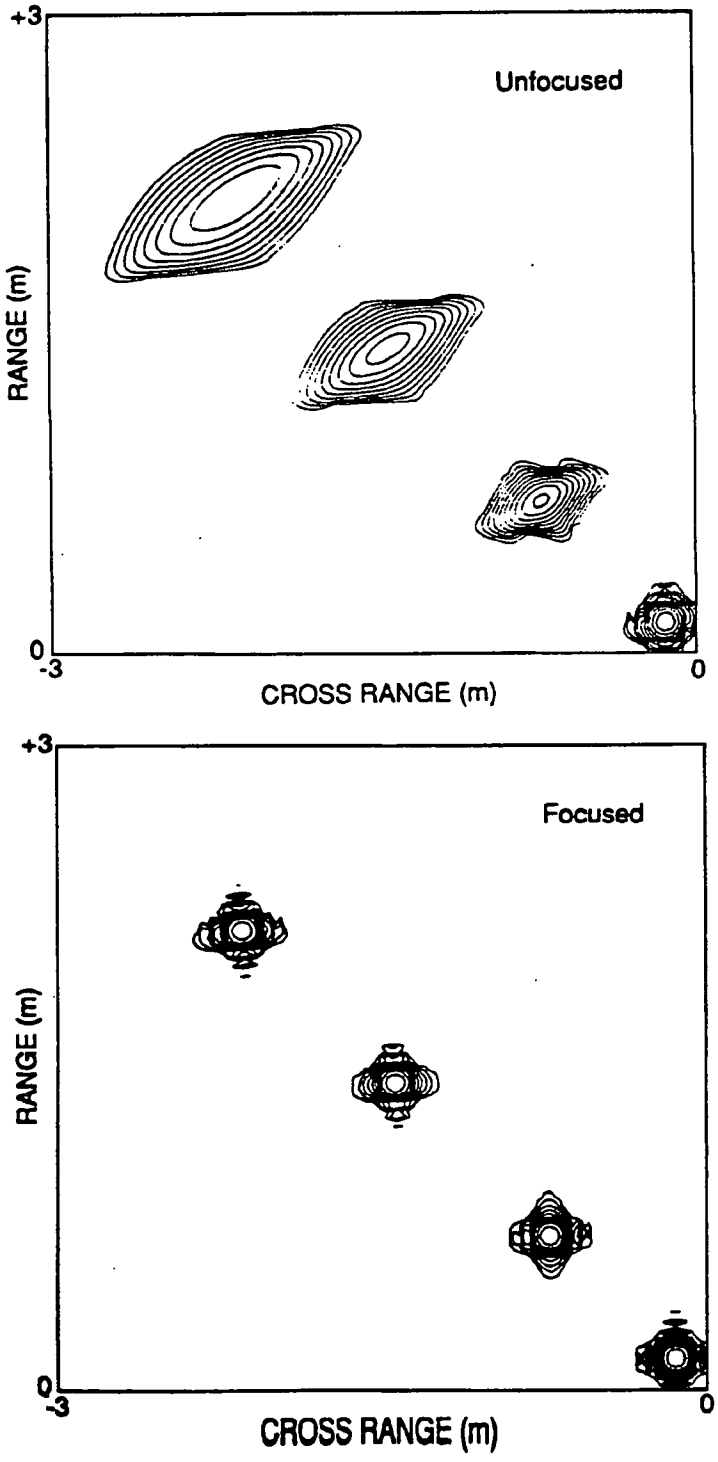

Figure 6

Example of an Unfocused and Focused Image [17]

CHAPTER 2

IMAGE EDIT AND RECONSTRUCT

This chapter introduces the IER concept with a mathematical development of the technique and a review of the related open literature.

Mathematical Development

It was described previously how the RCS of an object is defined in the spectral domain and how spectral domain data is processed using discrete Fourier Transforms to form a spatial domain image. The image edit and reconstruct algorithm makes use of the spatial separation of scatterers provided in the image to identify which sources are from the target and which are from the background. All sources not attributable to the target are then forced to zero and the inverse of the imaging process is applied to transform the truncated spatial domain to an estimate of the target only scattered field. The estimated RCS is then calculated using the scattered field estimate in (4). Following is a mathematical development of the IER algorithm when used with a 1-D down range image. The extension to cross range follows an identical development since both are processed with DFTs.

Invoking the IER technique on a down range image implies the time domain response is multiplied by a mask function to zero out the unwanted returns. Typically, this mask function is a rectangular window centered around the target return and is referred to as a time gate. Mathematically, multiplication in the time domain is equivalent to convolution

in the frequency domain so the estimated target range independent scattered field after the application of the time domain mask function is,

$$\tilde{E}_{est}^{tar}(f) = T(f) * \left\{ \tilde{E}^{tar}(f) + \tilde{E}^{bkgd}(f) \right\} \tag{21}$$

where,

$T(f)$ = the DFT of the mask function

$\tilde{E}^{tar}(f)$ = the true value of the target only range independent scattered field

$\tilde{E}^{bkgd}(f)$ = the range independent scattered field of the background (includes test fixture, chamber, interactions, etc.).

For the estimated field to be exact (i.e., $\tilde{E}_{est}^{tar}(f) = \tilde{E}^{tar}(f)$), two conditions are necessary:

$$T(f) * \tilde{E}^{bkgd}(f) = 0 \text{ and} \tag{22a}$$

$$T(f) * \tilde{E}^{tar}(f) = \tilde{E}^{tar}(f). \tag{22b}$$

To meet the first condition, either $T(f)$ or $\tilde{E}^{bkgd}(f)$ must be identically zero. If $T(f)$ is zero, then the time domain mask function is also zero and the entire image is wiped out. This of course is not desired, so meeting the first condition must imply $\tilde{E}^{bkgd}(f)$ is zero. Yet, if the background contribution is zero, there is no target RCS contamination, and there is no need to use the IER technique. To meet the second condition of (22), $T(f)$ must be an impulse function by the sifting property of convolution [19]. But an impulse in the frequency domain is a uniform function in the time domain, so there is no mask function. Since neither condition of (22) is met, two sources of error are always present with the use of IER to generate target RCS:

a. The contamination of the background response retained by gating.

b. The elimination of the target response lost by gating.

Mathematically, the two errors are expressed as:

$$\varepsilon_1 = T(f) * \tilde{E}^{bkgd}(f) \tag{23a}$$

$$\varepsilon_2 = \tilde{E}^{tar}(f) - T(f) * \tilde{E}^{tar}(f) \tag{23b}$$

With the total error in the scattered field being the vector sum of the two and the error in RCS from (4) being:

$$\varepsilon_\sigma = 4\pi \left| \varepsilon_1 + \varepsilon_2 \right|^2 \tag{24}$$

Applying a weighting function to the spectral domain data prior to forming the image reduces spreading of the image responses. Therefore, the target and background responses are easier to separate in the image and the errors of (23) are reduced. With a weighting function applied, (21) becomes:

$$\tilde{E}^{tar}_{est}(f) = T(f) * \left\{ W(f) \left[\tilde{E}^{tar}(f) + \tilde{E}^{bkgd}(f) \right] \right\} \tag{25}$$

where,

$W(f)$ = the weighting function.

This estimate is now that of the target scattered field weighted by $W(f)$, so a correction of the weighting function inverse is applied to (25), to get:

$$\tilde{E}^{tar}_{est}(f) = \left[1/W(f) \right] \cdot \left\{ T(f) * \left\{ W(f) \left[\tilde{E}^{tar}(f) + \tilde{E}^{bkgd}(f) \right] \right\} \right\}, \tag{26}$$

and the conditions of exactness of (22) become:

$$\left[1/W(f) \right] \cdot \left\{ T(f) * \left[W(f) \cdot \tilde{E}^{bkgd}(f) \right] \right\} = 0 \text{ and} \tag{27a}$$

$$\left[1/W(f) \right] \cdot \left\{ T(f) * \left[W(f) \cdot \tilde{E}^{tar}(f) \right] \right\} = \tilde{E}^{tar}(f). \tag{27b}$$

These conditions are again not met for the same reasons as (22), so the two scattered field error sources present with IER when weighting functions are used are:

$$\varepsilon_1 = [1/W(f)] \cdot \left\{ T(f) * \left[W(f) \cdot \tilde{E}^{bkgd}(f) \right] \right\} \tag{28a}$$

$$\varepsilon_2 = \tilde{E}^{tar}(f) - [1/W(f)] \cdot \left\{ T(f) * \left[W(f) \cdot \tilde{E}^{tar}(f) \right] \right\}, \tag{28b}$$

with the RCS error given by (28) in (24).

In words, the IER technique cannot exactly produce the RCS of a target when background sources are present. Errors arise from two sources related to the fact that the spatial domain data derived from finite spectral domain data is spread over the limits of its domain. The first error given in (28a) relates to the amount of background response contained within the time gate, and the second error given by (28b) relates to the amount of target response located outside the gate. These two errors share an inverse relationship in that minimization of one results in maximization of the other, and the optimization of the IER technique is accomplished by reducing the vector sum of the two errors.

Literature Review

The earliest literature found to cover the subject was a 1989 General Dynamics report by Hines and Brown[1]. In the section "Image Post Processing", they describe using a 2-D image gate to isolate a scattering source and then transform it back to the spectral domain. They include an example of a 2-D gate around a single point source located in an evenly spaced array of point sources and show good correlation with the theoretical RCS in the center 75% of the frequency band. They do not provide information on gate size, scatterer spacing, or measurement parameters.

Hines also teamed with Latham from McDonnel Douglas in 1990 to prepare a briefing on the subject and refers to the technique as "Image Reconstruction" [2]. They present reconstructed data of ideal point sources with time gates on the order of 400 times

the time domain resolution, $1/B$ and again achieve good results in the center of the band. They also provide reconstructed data of a measured flat plate to show the low level scattering of multiple interactions between the corners are removable. Alternate weighting functions are available with their software package, but they prefer the Hamming.

The most comprehensive paper found on the subject was a report by Fliss out of the Pacific Missile Test Center [3]. He presents an analysis of the error given by (28b) using 1-D time domain gating on uniform scatterers with various weighting functions. The error of (28a) is not included since all source returns are calculated and no test fixtures are used. He examines the percent truncated energy verses edit window size to show which weighting functions spread the energy in the spatial domain the least. The top performers in this noise free analysis were the 4-term Blackman-Harris and the Kaiser-Bessel ($\alpha = 3.5$) weighting functions which is expected, since they are both "optimal" windows in that they maximize energy in the main-lobe for a given minimum side-lobe level. He also examines the error spectrum (a plot of (28b) squared as a function of frequency) and truncated RCS as a function of frequency for a number of weighting functions. Results show the Blackman-Harris and Kaiser-Bessel are again the top performers but only the center 50% of the band is useful no matter which weighting function is applied. To overcome these band edge limitations, he advocates the technique of overlap processing as shown in Figure 7. Here the center 50% of the reconstructed spectral domain is used for each successive image. He does perform a limited noise analysis in that he shows "usable" data is obtained with a 10 range resolution cell gate centered on one of two equal amplitude scatterers also separated by 10 range cells. He does not define criteria for "usable" but his data is accurate to within 0.1 dB in the center

60 % of the band for 40, 50, and 90 dB signal-to-noise ratios (SNR) all using a Dolph-Chebyshev ($\alpha = 3.5$) weighting function.

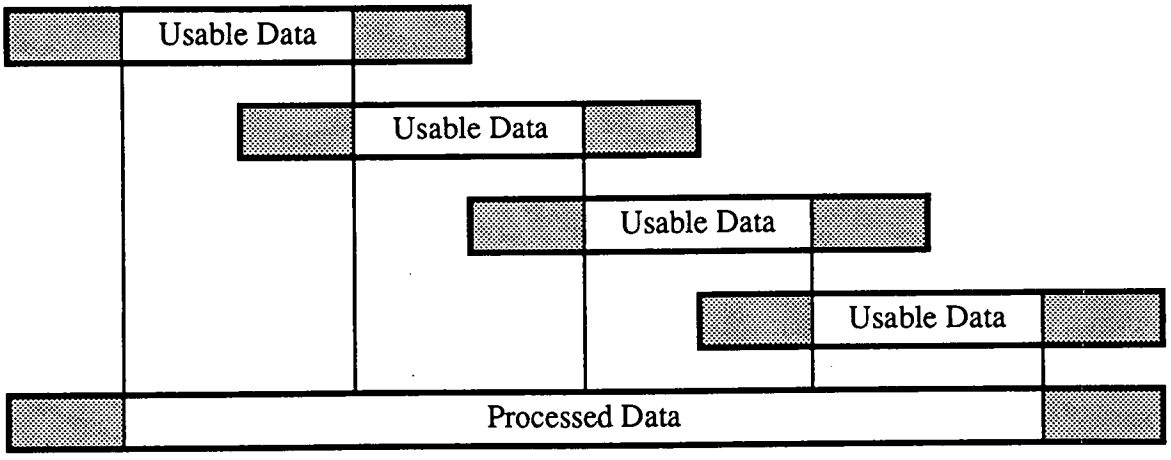

Figure 7

Overlap Processing.

The final paper discovered on the subject was a joint effort by Henry, Taylor, and Brumley [4]. Their purpose appears to be an introduction of the technique, not a validation. They describe the procedures and state a gate size rule-of-thumb as 10 to 15 range cells. An imperfect test fixture was constructed and it was shown they could edit and reconstruct the RCS of two 0.371 inch hemispheres and a piece of copper tape from actual measurements on the fixture. They do not provide information on the test parameters such as test fixture RCS (other than an image), background levels, or true target RCS so it is impossible to determine the accuracy of the technique or guidelines for implementation.

So the majority of the analyses done on the IER technique involve the use of point sources. The few test cases that do not (Hines and Latham [2] and Henry et. al. [4]) still use simple sources such as tape edges and low level plate diffraction. Recall from the development of the imaging algorithm that all sources are assumed to behave as point sources so the work to date has not realistically tested the limits of the IER technique. The analysis to follow attempts to further develop the understanding of the technique by testing it with scatterers other than point source.

CHAPTER 3

IMAGE EDIT AND RECONSTRUCT ANALYSIS

This chapter presents the development and results of the analysis performed using the IER technique with several non-ideal sources.

Development

To reduce the complexity of the analysis, all images generated were 1-D with resolution in the down range. As shown in chapter 1, generating images with resolution in both down range and cross range is accomplished with independent DFTs of far-field frequency and angle data, respectively, so extension of the results of this analysis to 2-D follows directly. Five variables to be analyzed were identified: signal-to-noise ratio (SNR), weighting function, image edit gate size, scattering source behavior, and test fixture. Variables which pertain to measurement accuracy (i.e., calibration, clutter, field-taper, etc.) were excluded by using calculations instead of measurements for the source signatures. The design of the analysis using the five variables is described next.

Signal-to-Noise Ratio

The SNR was held constant for the analysis. The purpose of including this variable was not to quantify the effects of noise, but rather to examine the IER technique in the presence of noise. Fliss stated that a 50 dB SNR was typical in RCS measurements [4], yet 30 dB was chosen for this analysis to simulate measurements of lower order scatterers. A single -30 dBsm noise file was generated using the RNNOA and SSCAL

routines of IMSL [20] and injected into each source RCS. Using the same noise file throughout the analysis eliminates variation in the results due to changing noise.

Weighting Functions

Four weighting functions were chosen: the uniform, Hann, Hamming, and 4-Term Blackman-Harris functions. Each is described in detail in [15]. The first three were chosen due to their popularity in the RCS measurement community and the fourth was chosen based on the favorable results achieved by Fliss [4]. Each of the four weighting functions are applied to each scattering source.

Edit Gate Size

The optimal gate size for reducing errors is variable for each application. Recall from chapter 2, the total error is the sum of that due to removing too much of the target response and that arising from not removing enough of the background response. In practice, it is usually not possible to optimize the gate size for each application since the true target response is not known. So in this analysis, a constant gate size was used with all test sources and weighting functions. The gate size was derived by optimizing the error resulting from using IER on a point source. Details of the derivation of the gate size are found in the Results.

Scatterering Source Behavior

All sources were created synthetically and their RCS was calculated at increments of 10 MHz over a 4 GHz bandwidth centered at 10 GHz which gave a time domain resolution of 0.25 nsec. The frequency files were zero padded to fill 0 to 20 GHz with the same 10 MHz increment, so the time domain granularity was 0.05 nsec. In order to hold the SNR constant for all sources, the RCS of each source was adjusted to a one square meter (zero dBsm) arithmetic average over the center 75% of the band before the -30

dBsm noise was injected. Only the center 75% was chosen based on the earlier work which showed the band edges were not usable after reconstruction. This adjustment in the target scattering to a 0 dBsm average is referred to as normalization in following discussions. Plots of each source are provided before normalization without noise and after normalization with noise.

The generated sources attempt to model scattering behaviors likely to cause problems for the IER technique. As identified in (27b), a source of error is the elimination of target response outside the time gate. Therefore, the more spread in time domain response, the higher the potential for error. Three general scattering types were selected which fall into this category. They are sources with: 1) highest RCS at the band edges, 2) antenna resonances, and 3) frequency bandpass characteristics. Each source and how they were created are described below.

Highest RCS weighted at band edges. Discontinuities in the domain of one Fourier transform variable induce spreading in the domain of the other transform variable. Therefore, an ideal source was created with a large discontinuity at the band edges as pictured in Figure A1. The source is referred to as an inverted cosine since it was created in dB with 40 times the negative of a cosine function. The inverted cosine normalized to 0 dBsm with the -30 dBsm rms noise is provided in Figure A2.

Antenna resonances. Any target which induces a phase shift on the range independent scattered field violates an assumption in the development of the RCS image algorithm. Therefore, when a scattering center induces a phase shift on the returned signal, the imaging algorithm associates the shift with propagation delay and displaces the source in the image from its true location. When the phase shift changes as a function

of frequency as is the case for resonant returns, the imaging algorithm spreads the source in the spatial domain. Three sources with resonant responses were modeled:

Half-wave dipole. Since the frequency band used for the analysis was 8 to 12 GHz, the dipole was modeled to have a half-wavelength resonance near 10 GHz. The dipole used had a length of 1.34 cm and radius of 0.0167 cm. The scattered fields of the dipole were calculated with NEC-MOM [21] using the input file included in Figure B1. The RCS as a function of frequency for the dipole at broadside as calculated by NEC-MOM is given in Figure A3, and the RCS normalized to 0 dBsm from 8.5 to 11.5 GHz with the -30 dBsm noise added is given in Figure A4.

Ten wavelength dipole. The half-wave dipole goes through only one resonance from 8 to 12 GHz, so a dipole of Ten wavelengths was created to introduce multiple resonances within the band. The dipole had a length of 26.8 cm and the same radius of 0.0167 cm. The scattered fields were again calculated for broadside with NEC-MOM using the input file given in Figure B2. The calculated RCS is plotted in Figure A5, and the normalized RCS with the noise added is plotted in Figure A6.

Multiple resonant wires. Mutual coupling associated with antennas having multiple elements changes the individual scattering behaviors of the elements. Since the coupling relates to interactions amongst the antenna elements, its response in an image is delayed. An array of three parallel, resonant dipoles was modeled to simulate a resonant antenna with strong mutual coupling. The three wires each had a radius of 0.0167 cm, were centered at the time origin and equally spaced by 7.62 cm, and had lengths of 1.24 cm, 1.34 cm, and 1.44 cm, respectively. Figure 8 (not drawn to scale) shows pictorially the wire configuration. The RCS calculated with NEC-MOM using the input file of

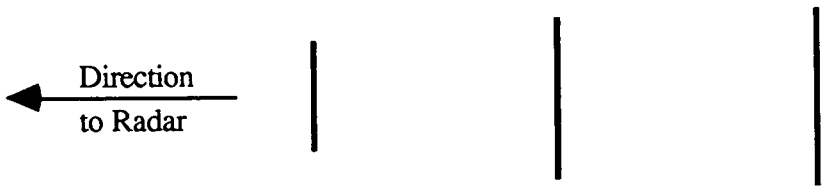

Figure 8

Multiple Resonant Wires

Figure B3 is plotted in Figure A7. The normalized RCS with noise added is plotted in Figure A8.

Frequency selective surface (FSS) scattering. A scattering source which presents a bandpass or bandstop frequency response is not imaged properly since it violates the point source assumption used in deriving the imaging algorithm. The transition regions between bandpass and bandstop in the frequency response become discontinuities in the DFT processing which causes the time domain response to spread. Two general frequency selective scattering sources were modeled: a step and a dip. For each type, an ideal and a more realistic source was created. These are described following.

Step source. An ideal source was generated with a 10 dB step located at the center frequency as shown in Figure A9. The source after normalization and with noise added is provided in Figure A10. Since this source is ideal, a second more realistic source was created by using PMM [22] to calculate the reflection coefficient of two dipole array layers separated by air. The PMM input file is provided in Figure B4. The calculated reflection coefficient amplitude is provided in Figure A11. To generate an image consistent with the other sources, however, requires the range independent

scattered field, not the reflection coefficient. Yet, if it is assumed the FSS is placed on a 0 dBsm uniform source, then the reflection coefficient becomes the scattered field. Using this assumption, the normalized RCS with noise added is shown in Figure A12.

Dip source. An ideal source was generated with a 10 dB dip located between 9 and 11 GHz as shown in Figure A13. The source after normalization and with noise added is provided in Figure A14. A more realistic source was once again created with PMM by calculating the reflection coefficient of a single slot array. The PMM input file is provided in Figure B5, and the calculated reflection coefficient amplitude is provided in Figure A15. With the same assumption as the Step Source to convert the reflection coefficient to a scattered field, the normalized RCS with noise added is shown in Figure A16.

Test Fixture

A generic test fixture was designed with no first order returns within the selected range gate. The planform of the fixture is given in Figure 9. Low RCS fixtures normally do not have specular returns so the fixture was designed to have only diffraction scattering. The RCS of the fixture was calculated with RCSBSC [23] with the input file provided in Figure B6. The calculated RCS was adjusted to a +10 dBsm arithmetic average over the center 75% of the band. With this method, the test fixture diffraction sources are modeled correctly as a function of frequency while the total RCS is controlled to an average that is 10 dB higher than the test sources. The test fixture was not included in most of the simulations, however. Recall from (24), the total error is the vector sum of the two error sources corresponding to the test fixture response contamination and the target response elimination, respectively. In this analysis, the two errors are examined independently for all sources to avoid confusion in determining the source of error. For

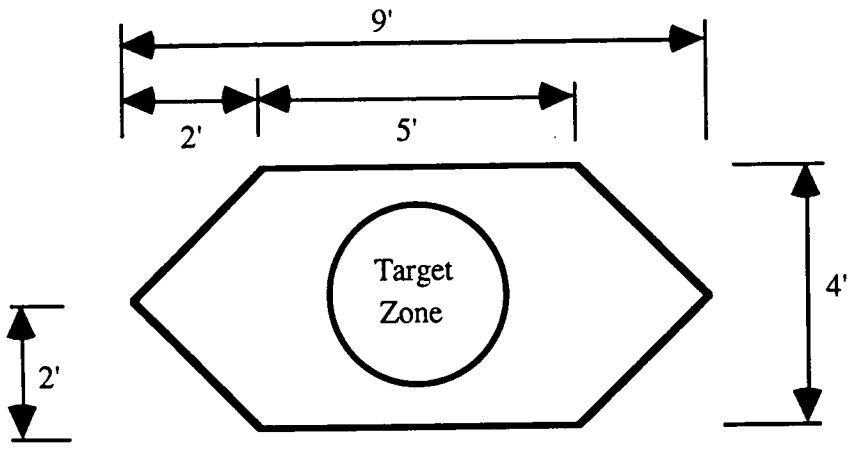

Figure 9

Generic Test Fixture Planform View

one of the resonant antenna sources, however, the total error is examined per (24) by using the IER technique on a single target plus fixture configuration. The multiple resonant wires source was chosen for this test since it is the most realistic in terms of scattering behavior.

Results

Before the results, some conventions in output data format are discussed. The RCS plots are all provided as RCS in dBsm (decibels relative to one square meter) vs. frequency and the image plots are provided as Impulse Response Envelope in dBV (decibels relative to one volt) vs. time. Error plots are provided as the ratio of true RCS without noise to edited RCS with noise and are plotted in dB. Error plot resolution is identical to the 10 MHz resolution of the target RCS files. Every attempt is made to keep the amplitude scales constant for all plots, and changes in scales are called out for the exceptions.

The edit window size or mask function used throughout the analysis was derived by varying the gate size for a uniform point source. The error given by (28b) due to the test fixture is not used in determining the common gate size since its impulse response was low in the target region. This becomes evident later in this section when the test fixture results are provided. Figure A17 gives the RCS vs. frequency of a 0 dBsm uniform point source from 8 to 12 GHz with the -30 dBsm noise injected. Figures A18 through A20 give the point source RCS after weighting with a Hann, Hamming, and 4-Term Blackman-Harris function, respectively. Of course, applying a uniform weighting does not affect the data of Figure A17 so it is not presented as a separate plot. Figures A21 through A24 give the point source time domain plots for the four weighting functions. To minimize the effects of Gibb's phenomena in the frequency domain, the time domain gate edges correspond to nulls in the impulse response of the uniform source. With this criteria, four gate sizes were attempted: 8/B (2 nsecs), 10/B (2.5 nsecs), 12/B (3 nsecs), and 14/B (4 nsecs), with each centered at the time reference. The error plots for each window size for the four weighting functions are plotted in Figures A25 through A40. Using the format of the error plots, an error figure for the estimated RCS is given as:

$$\sigma_\varepsilon = \sigma^{tar} / \sigma^{est} \tag{29}$$

where σ^{tar} is the true target RCS without noise and σ^{est} is the estimated RCS using IER. The rms of this error figure was calculated using the data from 8.5 to 11.5 GHz for each weighting function and window size and is provided in Table 1. From the table, the lowest rms error occurs with a 12/B window for three of the four weighting functions, so it was chosen as the gate size used for the entire analysis. Using this common gate size, the IER results for the eight sources and four weighting functions are now discussed.

Table 1

Rms Error Over Center 75% of Band After Image Edit and Reconstruct of a 30 dB SNR Uniform Source for Given Weighting Function and Window Size.

Window	Weighting Function			
	Uniform	Hann	Hamming	Blackman-Harris
8/BW	-10.49 dB	-20.07 dB	-18.21 dB	-21.38 dB
10/BW	-11.59 dB	-21.48 dB	-19.74 dB	-21.91 dB
12/BW	-12.29 dB	-22.08 dB	-19.79 dB	-21.05 dB
14/BW	-12.79 dB	-20.57 dB	-19.26 dB	-17.38 dB

Source Only Results

This section covers the errors found when the IER algorithm is applied to the sources with noise. There are no test fixture contributions evaluated in this section. To facilitate evaluation of the IER technique on the source, plots of both the time domain response and the RCS error figure defined in (29) are provided. Each of the time domain plots are compared to the point source time domain plots given in Figures A21 through A24 for the four weighting functions, respectively. Also, the absolute value of maximum amplitude error for each source with all weighting functions is provided in Table 2. The baseline for determining acceptable performance of the technique with the source is the error derived from a target to fixture cross section separation of 20 dB. The maximum error with this separation is 0.9 dB which is given by perfect destructive interference.

Inverted cosine. The time domain impulse response envelope for the inverted cosine source with the four weighting functions are shown in Figures A41 through A44. The

Table 2

Absolute Value of Maximum Error After IER

for All Sources with Each Weighting Function

Source	Absolute Value in dB of Max. Error for Given Weighting Function			
	Uniform	Hann	Hamming	Black-Harris
Point	0.49	0.05	0.10	0.11
Inv. Cosine	31.67	0.22	1.82	0.11
Short Wire	0.34	0.08	0.09	0.22
Long Wire	15.39	15.64	15.61	15.55
Three Wires	4.92	1.31	0.80	4.13
Ideal Step	5.96	6.24	6.22	6.95
FSS Step	1.11	0.86	0.88	2.22
Ideal Dip	6.94	5.92	6.08	5.34
FSS Dip	32.46	19.20	19.64	18.92

sidelobes of the cosine source are up from those of the uniform source, but the mainlobe width is narrower. From the time domain plots it appears only the Blackman-Harris window will provide good results since it is the sole weighting function to push the sidelobes down to the noise level within the +/- 1.5 nsec gate. The error plots provided in Figure A45 through A48 somewhat confirm this, since the Blackman-Harris results are the best. Both the Uniform and Hamming weighting functions do not pass the error requirement. Notice the Uniform weighting result is plotted on a ten times scale (ordinate scale is ten times the normal scale).

Single wire resonant near 10 GHz. The impulse response plots for this source are presented in Figures A49 through A52. For all four weighting functions, the peak of the response is displaced in time corresponding to the phase shift induced on the scattered field by the complex impedance of the dipole. The sidelobe levels and fall off are similar to the point source responses so the errors are expected to be minimal. Observing the error plots of Figures A53 through A56 shows they are minimal and all four weighting functions pass the error requirement, with the Hann function performing the best. Table 2 lists the error calculations in the row "Short Wire".

Single wire resonant near 500 MHz. The time domain plots for this multi-resonant dipole are exhibited in Figures A57 through A60. The mainlobe is not displaced from the time reference as with the last source, but the sidelobes are definitely up from the point source responses. In fact, for all but the Uniform weighting, the response outside the main lobe is more of a constant than a lobing pattern. With this spread in energy, the errors using IER are predicted to be higher than those with the point source. The error plots for the wire are provided in Figures A61 through A64 and are all on a ten times scale. Referring back to the frequency response of the source in Figure A6, sharp transitions are evident near 9.5 and 10.7 GHz. In the error plots, the largest errors occur at the same transition points. Fourier analysis readily explains this phenomena. The transition regions in the frequency response approximate delta functions which have a broad time domain response. The energy truncated when the image is edited, then, is mostly from the delta functions, so the reconstructed frequency domain is least accurate in their vicinity. Of all the resulting error plots, the Blackman-Harris weighting performs the best, but none of them pass the criteria. The maximum errors are listed under "Long Wire" in Table 2.

Multiple wires resonant near 10 GHz. Figures A65 through A68 give the impulse response plots for this source. The three wires were placed 0.25 feet apart which corresponds to a two way propagation time of 0.5 nsecs. With the Uniform weighting, the three independent sources with this spacing are evident, but just like with the single wire, their responses are shifted in time. The degradation in resolution with the remaining three weighting functions is apparent in the respective time domain plots. Mutual coupling effects are barely noticeable at 1 nsec with the Uniform weighting and 1.5 nsec with the Hann and Hamming weightings. Still, the sidelobe fall off is similar to the point source response. The error plots are displayed in Figures A69 through A72 on a two times scale. Each plot exhibits the worst error near 11.2 GHz which corresponds to a deep null in the source frequency response shown The large error here may again be due to the spread in time domain energy of the sharp transition at the null, or it may be an artifact of the noise on this low level scattering area. To determine which was the cause, the analysis for this source was redone without noise. Comparing the error plots for the noise free case given in Figures A73 through A76 with those in Figures A69 through A72 reveals the noise is not the dominant factor, so the cause for error must be the sharp transition. In the noise analysis, the Hamming was the only one of the four weighting functions to pass the error criteria as shown in Table 2..

Ten dB ideal step source. Impulse response plots are provided in Figures A77 through A80. The responses are definitely spread from those of the point source with the sidelobe structure again disappearing for all but the Uniform weighting. The errors plots are given in Figures A81 through A84 all on a ten times scale. Each weighting function result has its largest error at the 10 dB step in the frequency response of Figure A10. None of the weighting function results pass the error requirement. Notice, however, from

both the table and the error plots that the Uniform weighting has the least error of the four.

FSS step source. Figures A85 through A88 display the time domain plots of the source. The FSS was created with dipole arrays so the displacement in time of the main lobe due to the dipole impedance occurs again. The two layers were separated by 0.59 cm which corresponds to a two way time delay of 0.04 nsecs so the separate returns of the layers are not resolvable. The sidelobe levels are comparable to those of the point source, so the errors are expected to be minimal. The error plots of Figures A89 through A92 somewhat confirm this. Each weighting function has small errors but only the Hann and Hamming pass the criteria.

Minus ten dB ideal dip source. Time domain impulse response plots for the source are exhibited in Figures A93 through A96. The resolution is improved for each weighting function over that of the point source but the sidelobes have increased. The error plots (on a ten times scale) of Figures A97 through A100 show that large errors occur at the transition regions of the frequency response of the source. The maximum error criteria is not met for any of the weighting functions.

FSS dip source. Figures A101 through A104 show the time domain plots for the source. The source was created with a single array of slots but from the impulse response plots it appears as if there are two scattering sources. Still, the sidelobe levels fall off like those of the point source so errors are expected to be minimal. The error plots are provided in Figures A105 through A108 on a ten times scale with the ordinate shifted. The errors are minimal through most of the band but are quite large at the dip in frequency response of Figure A16. Once again, this large error is explained with the

Fourier analysis argument used with the Long Wire source. None of the weighting functions pass the acceptance criteria due to this large dip.

Test Fixture Results

This section addresses the results of using the IER technique on the test fixture alone. The test fixture RCS as calculated by RCSBSC is provided in Figure A109 and its RCS after normalizing to +10 dBsm and adding noise is given in Figure A110. Figures A111 through A114 display the impulse response plots of the test fixture with the four weighting functions applied. The four sources of diffraction return from the corners of the fixture are evident in all four plots. The same time gate of +/- 1.5 nsecs (or 12/B) was applied to all four impulse responses and the resulting RCS after reverse processing is plotted in Figures A115 through A118. These are plots of edited RCS in dBsm vs. frequency, not the error plots presented in the source only results. The average RCS calculated from the four plots is provided in Table 3. Since the average is calculated over the same 8.5 to 11.5 GHz, a direct comparison of the values of Table 3 to the original average RCS of 10 dBsm demonstrates the reduction in the background return using IER on this model test fixture. Also, since all the test sources were normalized to 0 dBsm, the numbers in Table 3 can be interpreted as fixture to target RCS separation. All of which are below the -20 dB accepted value.

Source Plus Test Fixture Results

In the test fixture only results, it was shown how the test fixture RCS was reduced to at least 20 dB below the target signature with the IER technique. One could imply from this that using IER on a source plus test fixture configuration with this magnitude of separation would result in errors very similar to those of the source only. In this section, the error is determined for the Three Resonant Wires target with the test fixture to see if a difference with the source only results occurs. The target plus test fixture RCS was

Table 3

Average RCS in dBsm from 8.5 to 11.5 GHz of Edited Test Fixture Response

	Weighting Function			
	Uniform	Hann	Hamming	Black-Harris
Average RCS	-21.75	-42.49	-36.90	-44.76

created with a coherent combination of the respective range independent scattered fields. The resulting RCS with the -30 dBsm noise added is given in Figure A119. The impulse response plots for target plus test fixture are provided in Figures A120 through A123. The target and test fixture features are discernible in all four plots, but are slightly overlapping with the Blackman-Harris weighting. It appears that the Hann and Hamming functions will perform the best since the target and test fixture responses have both died down to the noise level at the gate edges. The error plots are exhibited in Figures A124 through A127 on the same two times scale as the target only error plots of Figures A69 through A72. The scales are equivalent to make comparisons easier, even though the result for the Uniform weighting function extends beyond the scale boundaries. Comparing the results with and without the test fixture shows the errors are increased for all cases when the fixture is present. What is interesting, is that the error plots are nearly the same pattern, just with higher amplitude in the test fixture case. The amplitude increases are small in most cases, but seem quite high for the Uniform weighting since they are higher than expected for the target to background scattering level separations given in Table 3 even if coherent addition is assumed. This is due to the fact brought out in (24) that the RCS error is the absolute value of the coherent sum of the errors. For additional comparison, Table 4 provides the maximum errors for the target plus fixture case and a repeat of the data in Table 2 for the target only case. The largest error in all

four cases occurs at the deep null in the target RCS plot shown in Figure A8, so the increased error for the Hamming weighting is not as drastic as the data in Table 4 would imply. The point to be made is, the target to test fixture ratios given in Table 3 are not a reliable estimate of the total error involved with using IER on a target with a test fixture. The inclusion of the test fixture appears to amplify the error plots for the target only case in a non-linear fashion. The larger the error in the target only case, the larger the amplification in the target plus test fixture case.

Table 4

Errors After IER with Each Weighting Function for the Three Wire Source With and Without the Test Fixture.

Source	Absolute Value in dB of Max. Error for Given Weighting Function			
	Uniform	Hann	Hamming	Black-Harris
Three Wires Plus Test Fixture	9.89	1.19	2.60	4.11
Three Wires	4.92	1.31	0.80	4.13

CHAPTER 4

CONCLUSIONS

The purpose of this report was to examine the image edit and reconstruct method of generating component RCS signatures and to develop a further understanding of its limitations. Before the conclusions of the analysis performed for this purpose are presented, the major points of the paper are summarized.

Summary

An imaging algorithm was traced in chapter 1 and it was discussed how with any imaging algorithm, the processing assumes all scattering sources on the target behave as uniform point sources. Target scattering centers which do not behave in this manner are imaged improperly and can lead to incorrect interpretations of the image.

The IER algorithm was developed mathematically in chapter 2 and it was shown how two error sources are always present when the technique is used to remove background sources from a measurement. The errors are due to: 1) eliminating the portion of the target response which lies outside the edit gate, and 2) retaining the portion of the background response which lies inside the edit gate.

The available open literature on the IER technique was also reviewed in chapter 2 and it was shown how the majority of the analyses of the technique studied the results when uniform point sources are used. All showed favorable results but experimental details

were not adequate to form general conclusions on the technique's limitations.

In chapter 3, an analysis of the IER technique was performed using eight non-uniform test sources and four weighting functions. A common edit gate used with all sources and weighting functions was developed using the IER technique on a point source. The favorable results found with the point source were not consistently evident with the other sources. Their results show the errors varied dramatically for the different configurations with most having far greater error than that of the point source.

An analysis of using the IER technique on a test fixture plus target was reported in a section of chapter 3. It was shown that the inclusion of the test fixture amplifies the errors resulting from the target only tests. The amplified errors were higher than expected, given the low cross section of the edit test fixture alone also reported in chapter 3.

Conclusions

Examining the accuracy of the image edit and reconstruct technique using uniform point sources alone is not adequate for determining general guidelines for its use. The test sources used in the analysis section of this report modeled potential error causing scattering behaviors not found with a uniform point source and the results were widely varied. Some in the literature attempt to provide guidelines for edit gate size [3,4], but these results demonstrate a common gate size is not applicable to all scattering sources.

An indication for success of the technique is found in the image domain. Some of the down range responses in the analysis (e.g., long wire and ideal step) had high sidelobe structures which caused a considerable portion of the target response to be removed with

the edit gate. Many of the other sources had sidelobes which died down to the noise level within the time gate so predictably their errors were small (e.g., short wire and FSS step). Reexamining the FSS dip results, however, show low sidelobes in the time domain, but large errors in the edited RCS. So sidelobe falloff does not always provide an accurate measure of the techniques accuracy.

The use of weighting functions reduced the error for all sources except the long wire and ideal step . From this, it appears that as long as the target response is not spread in the time domain, the use of weighting functions improves the performance of the IER technique. Of the four weighting functions used, one is not always the best. Intuitively, the Blackman-Harris function should outperform the others since it has the highest percent energy in the main lobe, but it only does in two of the nine cases listed in Table 2.

The magnitude of the total error is not predictable from an analysis of the test fixture alone. It is true that the lower the edited RCS of the test fixture alone, the smaller the error to a test fixture plus target configuration, but the coherent combination of error sources makes it impossible to determine total error from such a test. However, the errors after the IER technique was applied were greatly reduced from those of the target plus test fixture before editing and reconstruction.

Finally, the IER technique is without question a useful tool for reducing the errors associated with background responses in a target RCS measurement. But, there will always be an error involved of which the magnitude is not predictable, so the technique is not recommended when absolute signatures are desired.

CHAPTER 5

RECOMMENDATIONS FOR FUTURE WORK

This report concentrated on studying the impacts of the Image Edit and Reconstruct method when non uniform point sources are used and showed that the results vary widely. There are other important points which need to be addressed to develop further understanding of the technique.

In the end of chapter 1 was a discussion of 2-D processing often used to clean up an image. Examples covered were focusing, zero-doppler filter, and near-to-far field transformation. Use of these techniques alters the image and thus the IER process so their impacts need to be studied.

Also, this report only addressed the use of a rectangular window for editing. What are the effects of multiple gates and/or non-rectangular gates such as a circle? Or what are the effects of using a weighting function on the mask function to reduce oscillations in the reconstructed RCS?

A further understanding of noise is required. This report use a single SNR with all test sources, but what are the limits and what is expected with more or less noise?

Other research areas can also be found, but the important point is much still needs to be learned. This further reinforces the statement in the previous chapter about the unpredictability of the technique and that other techniques should be considered if available.

APPENDIX A

PLOTS OF IMAGE EDIT AND RECONSTRUCT ANALYSIS

Included in the following figures are plots for each source referenced in chapter 3 of the main body of the report. Plots include source RCS, time domain responses with the four weighting functions applied, and the resulting RCS error after image edit and reconstruct.

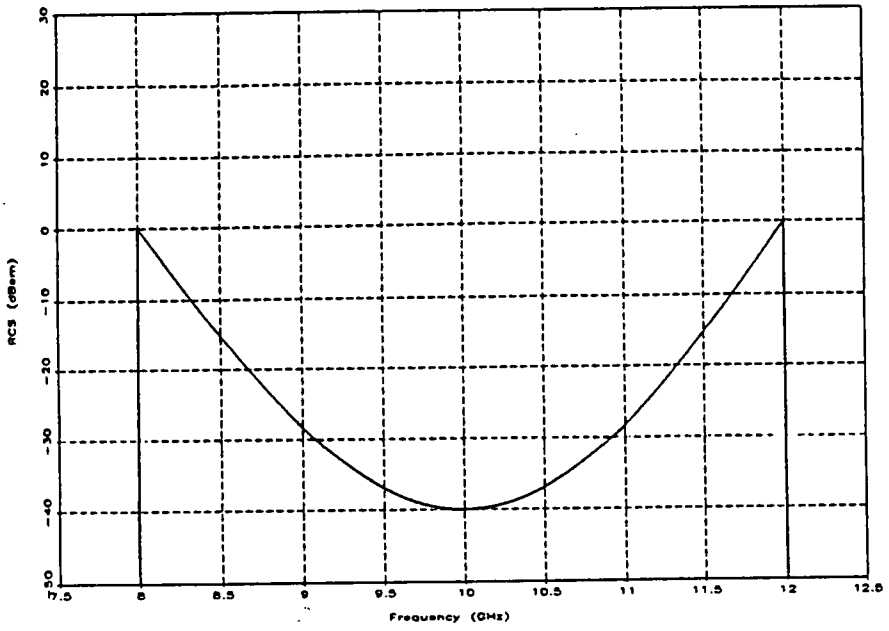

Figure A1

Inverted Cosine Source Before Normalization

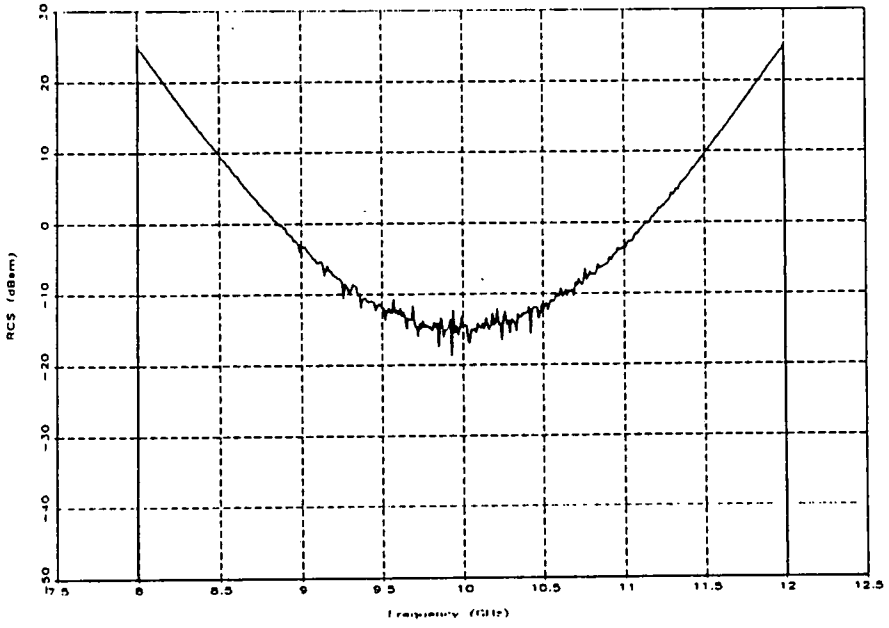

Figure A2

Inverted Cosine Source with -30 dBsm Noise

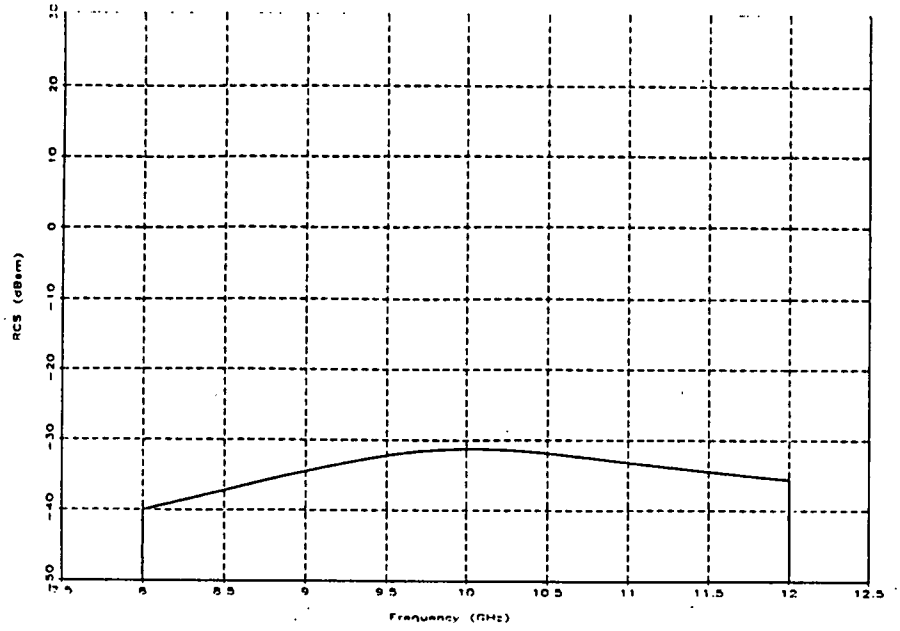

Figure A3

Single Wire Resonant Near 10 GHz Before Normalization

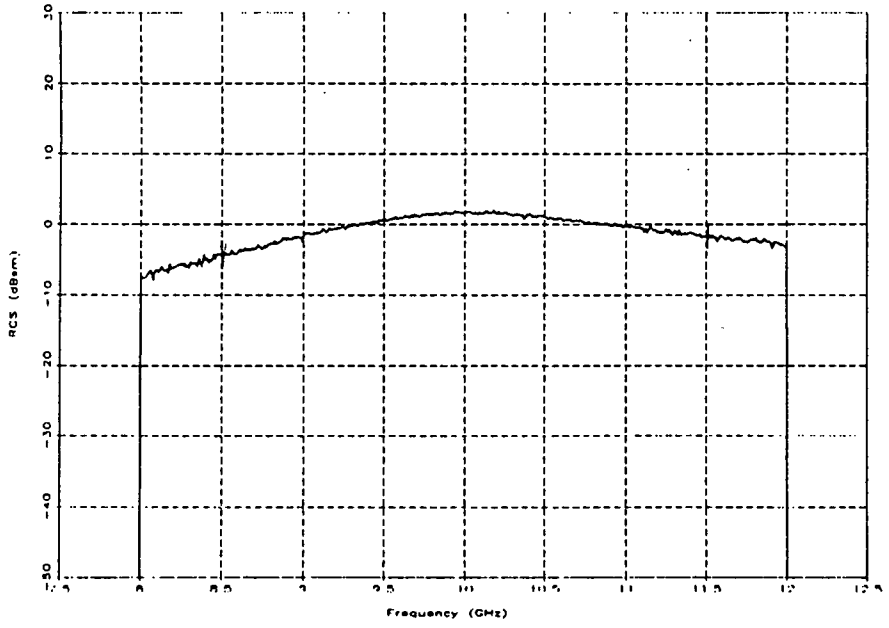

Figure A4

Single Wire Resonant Near 10 GHz with -30 dBsm Noise

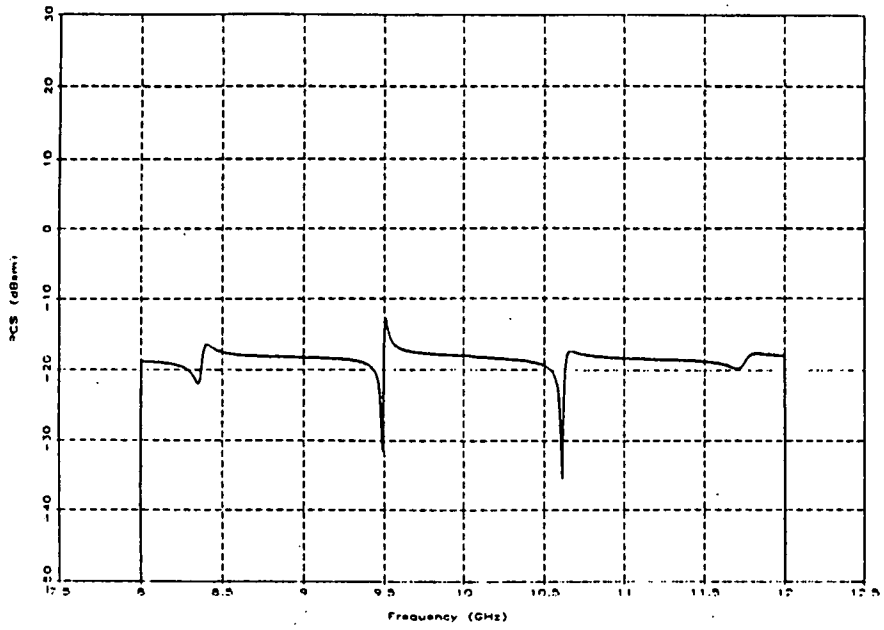

Figure A5

Single Wire Resonant Near 500 MHz Before Normalization

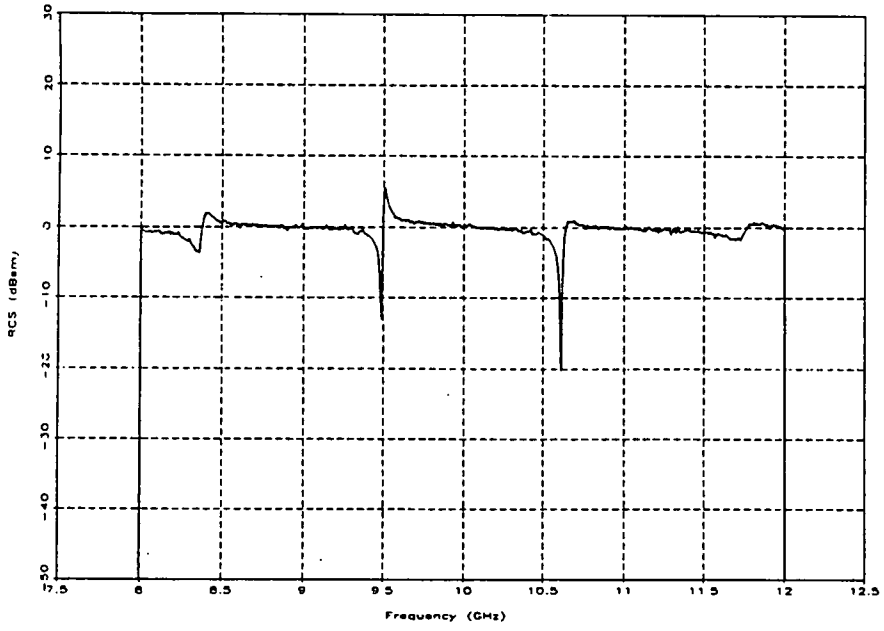

Figure A6

Single Wire Resonant Near 500 MHz with -30 dBsm Noise

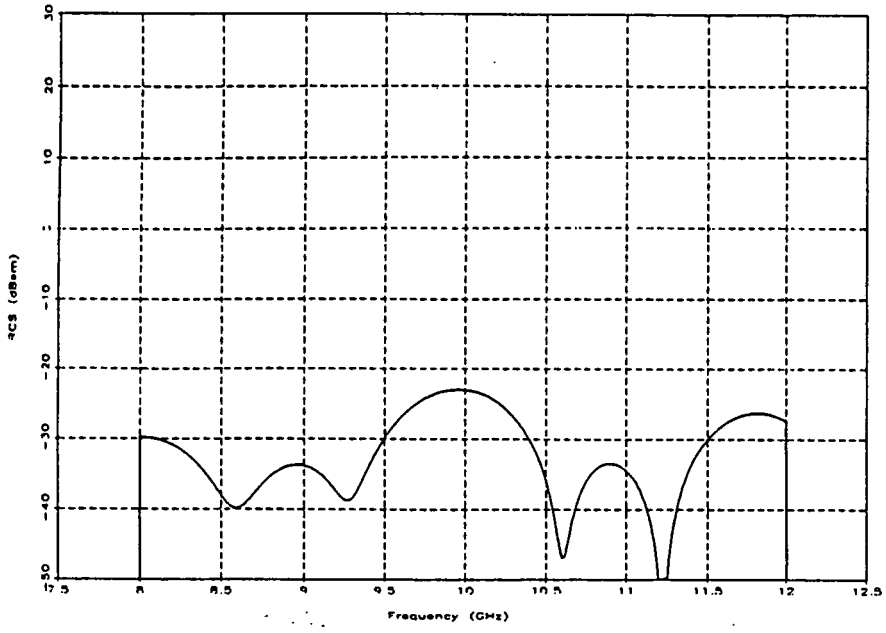

Figure A7

Three Wires Resonant Near 10 GHz Before Normalization

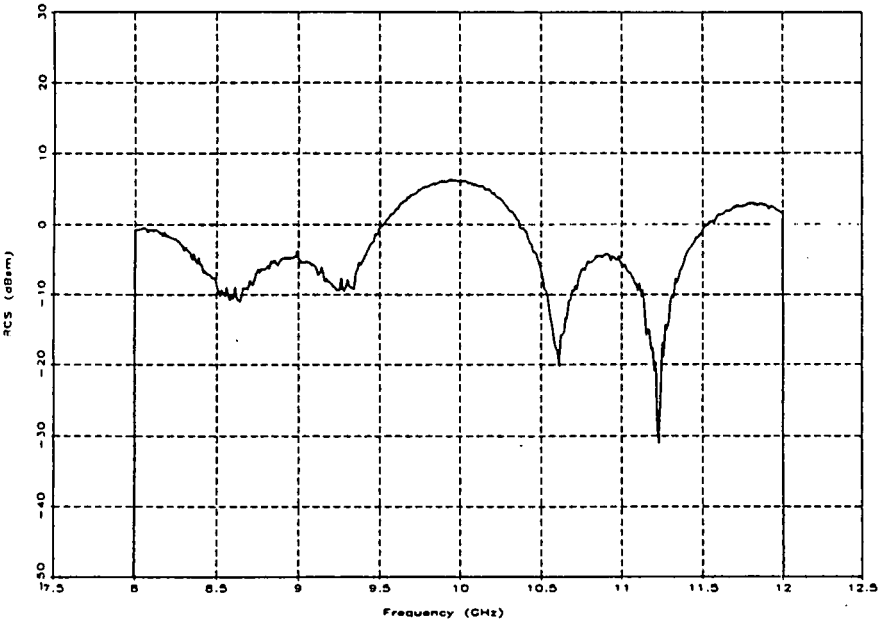

Figure A8

Three Wires Resonant Near 10 GHz with -30 dBsm Noise

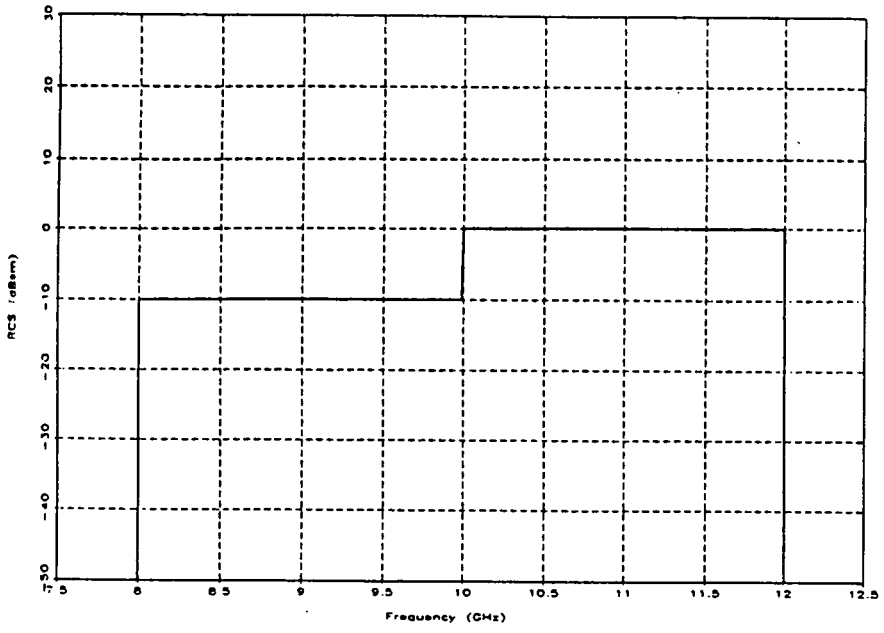

Figure A9

10 dB Ideal Step Source Before Normalization

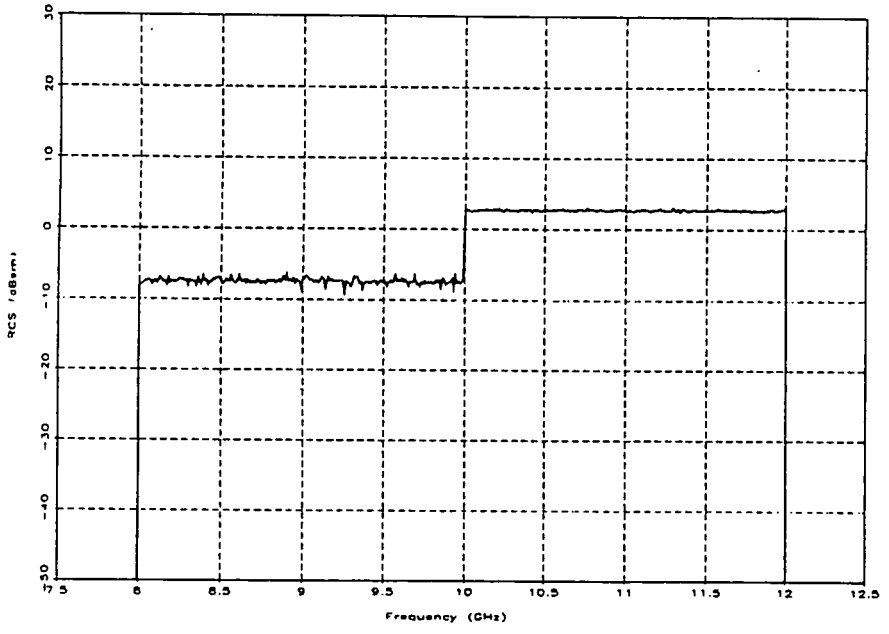

Figure A10

10 dB Ideal Step Source with -30 dBsm Noise

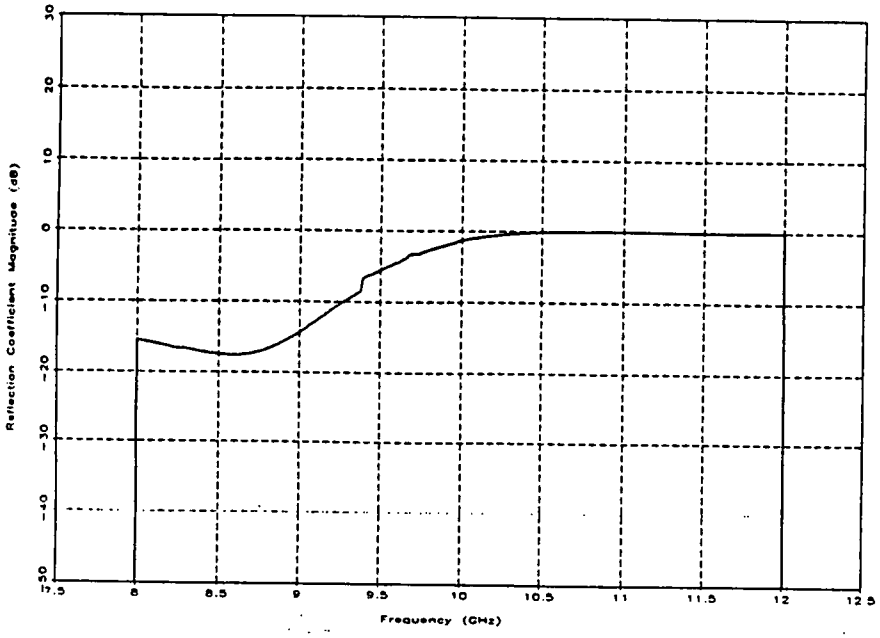

Figure A11

FSS Step Source Before Normalization

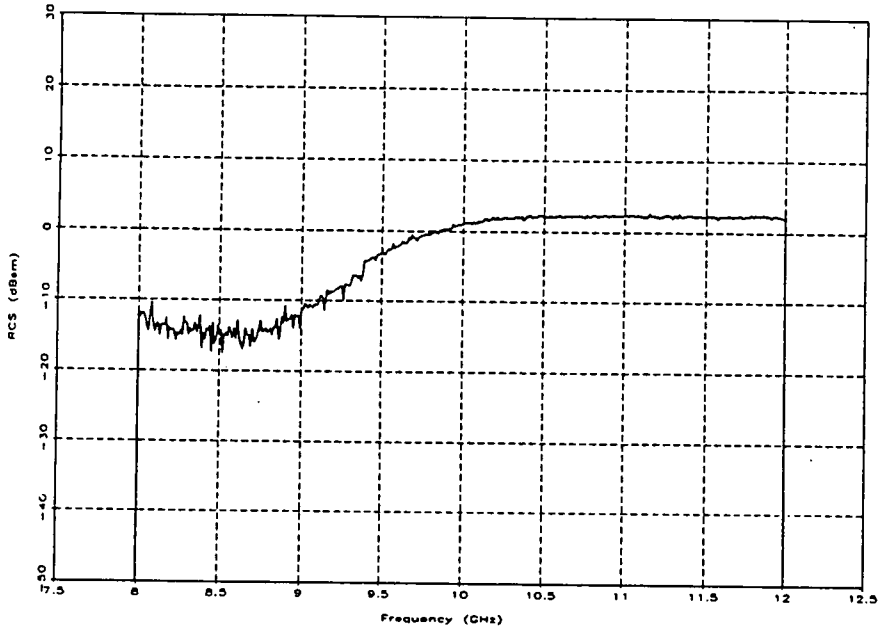

Figure A12

FSS Step Source with -30 dBsm Noise

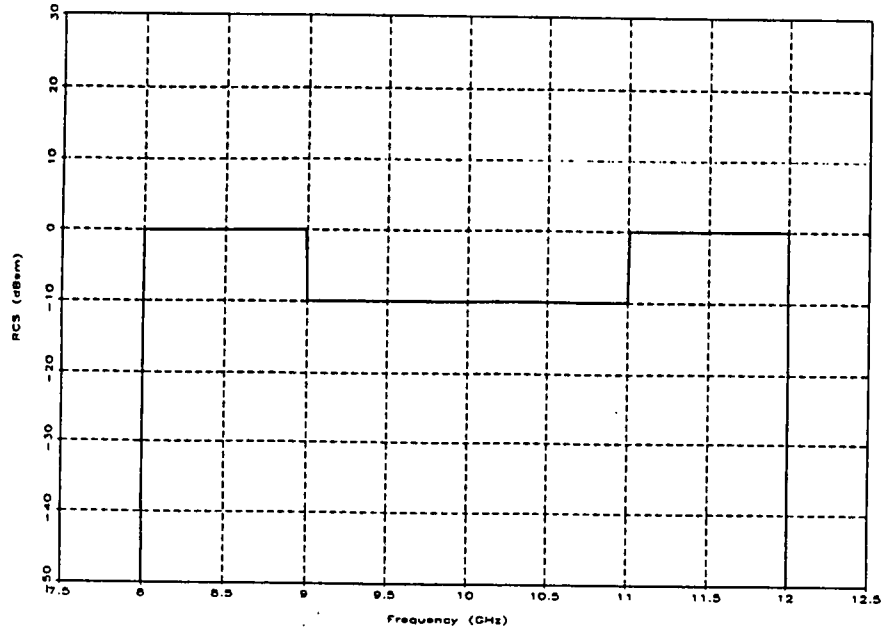

Figure A13

-10 dB Ideal Dip Source Before Normalization

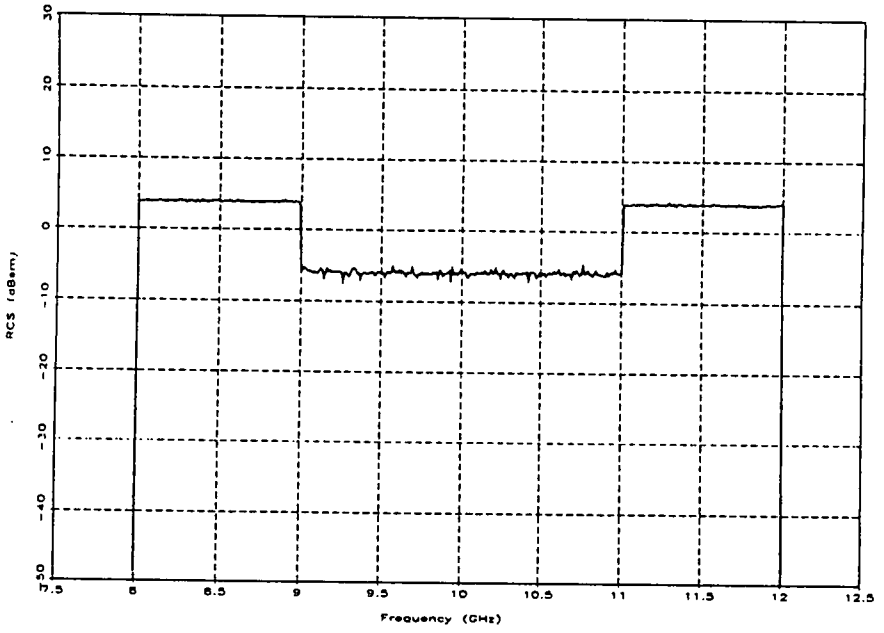

Figure A14

-10 dB Ideal Dip Source with -30 dBsm Noise

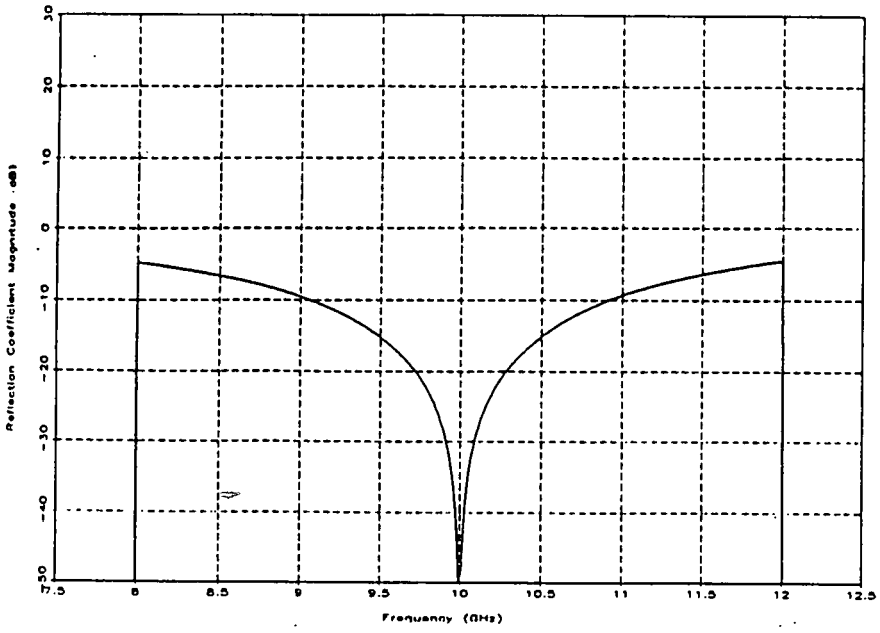

Figure A15
FSS Dip Source Before Normalization

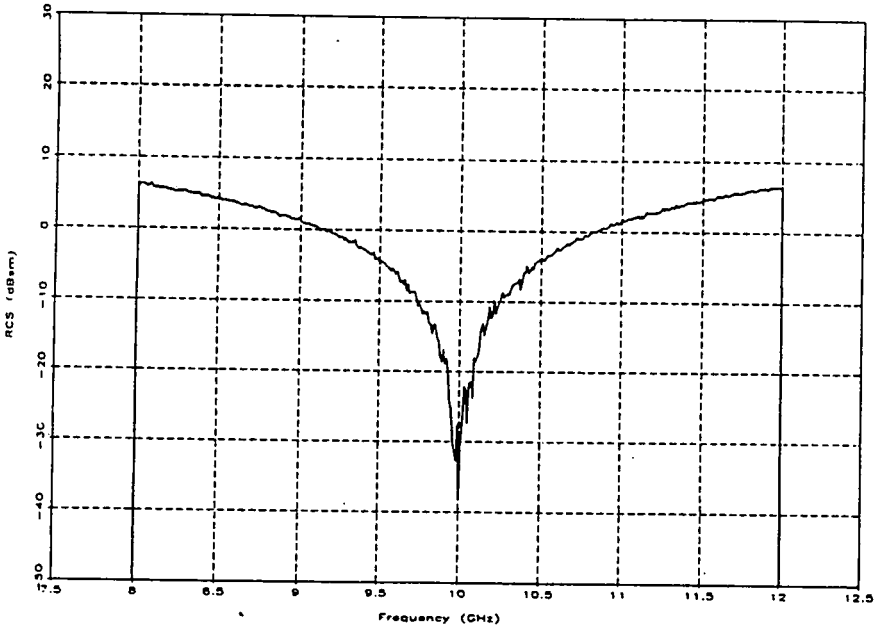

Figure A16
FSS Dip Source with -30 dBsm Noise

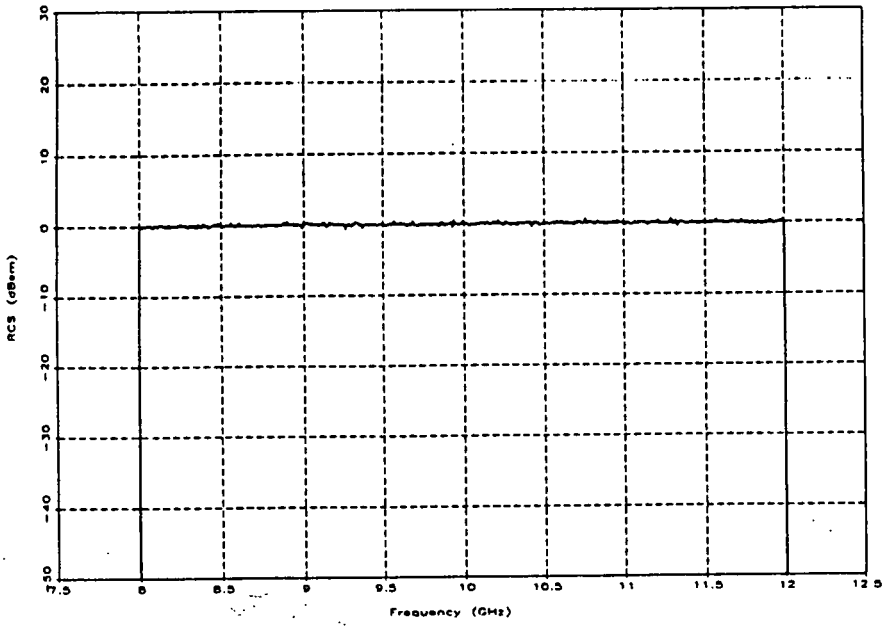

Figure A17

Zero dBsm Point Source with -30 dBsm Noise

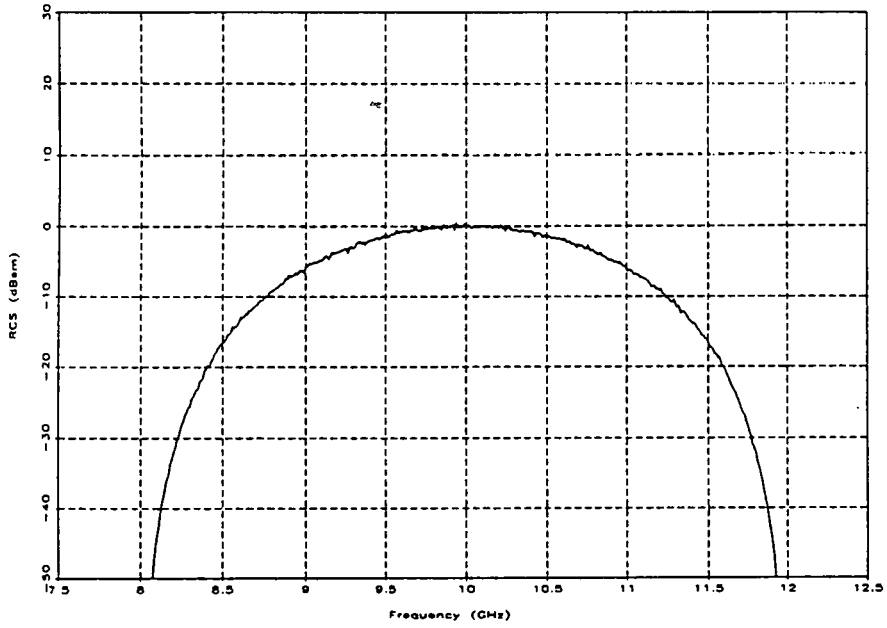

Figure A18

Zero dBsm Source with -30 dBsm Noise
Hann Weighting

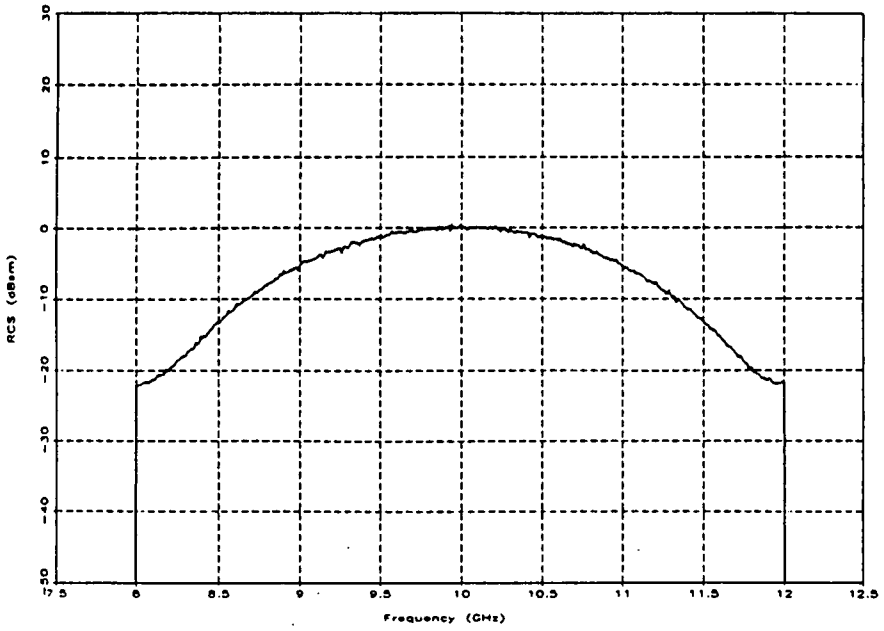

Figure A19

Zero dBsm Point Source with -30 dBsm Noise
Hamming Weighting

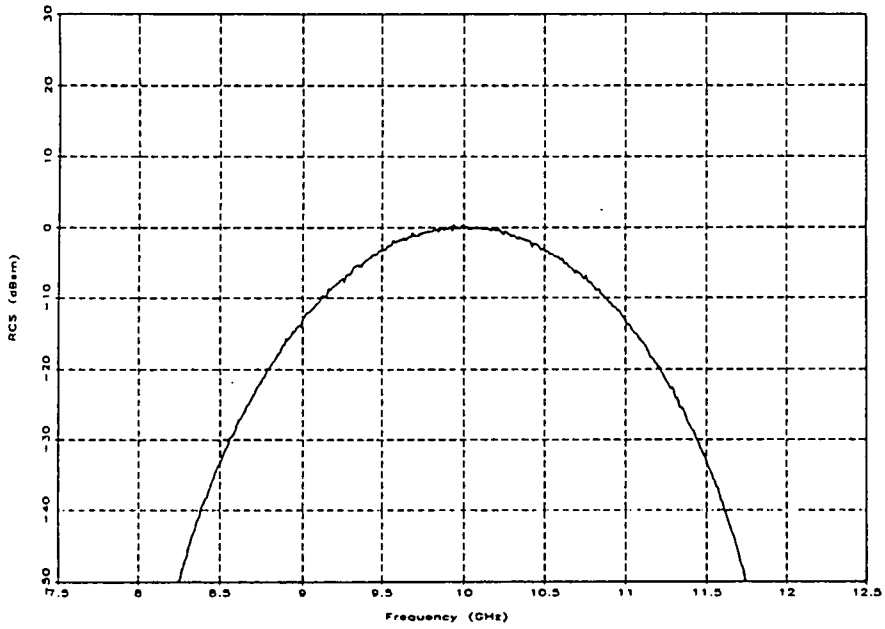

Figure A20

Zero dBsm Source with -30 dBsm Noise
Blackman-Harris Weighting

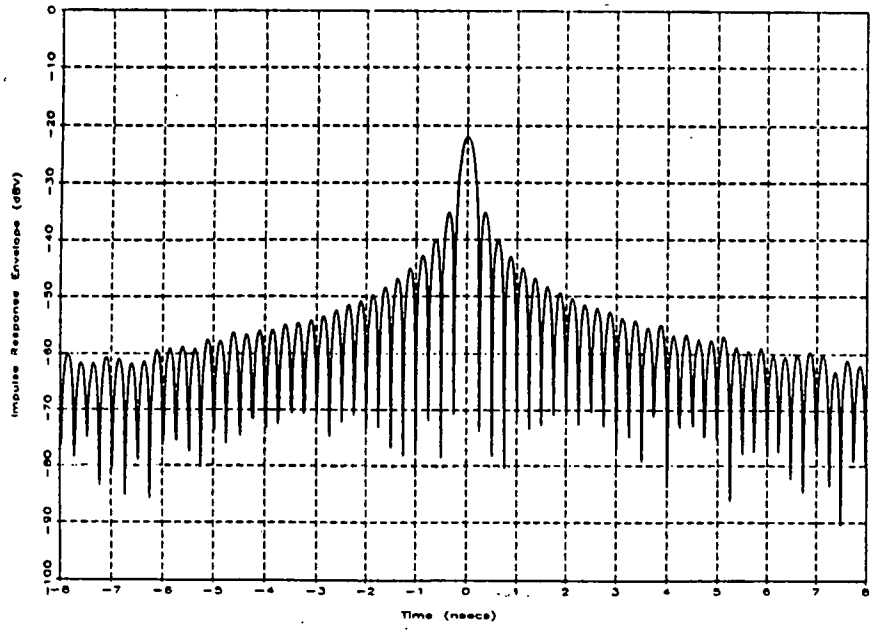

Figure A21

Zero dBsm Point Source with -30 dBsm Noise
Uniform Weighting

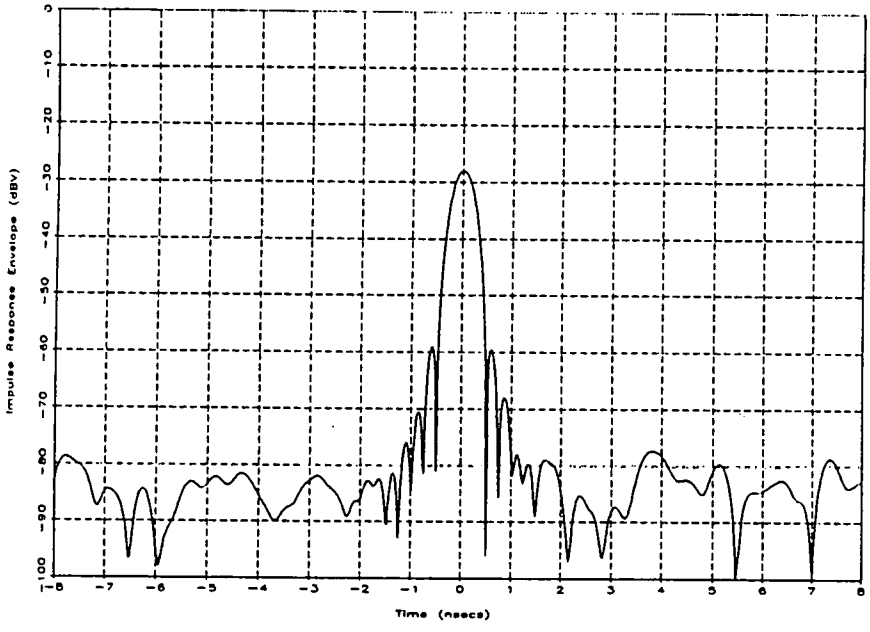

Figure A22

Zero dBsm Source with -30 dBsm Noise
Hann Weighting

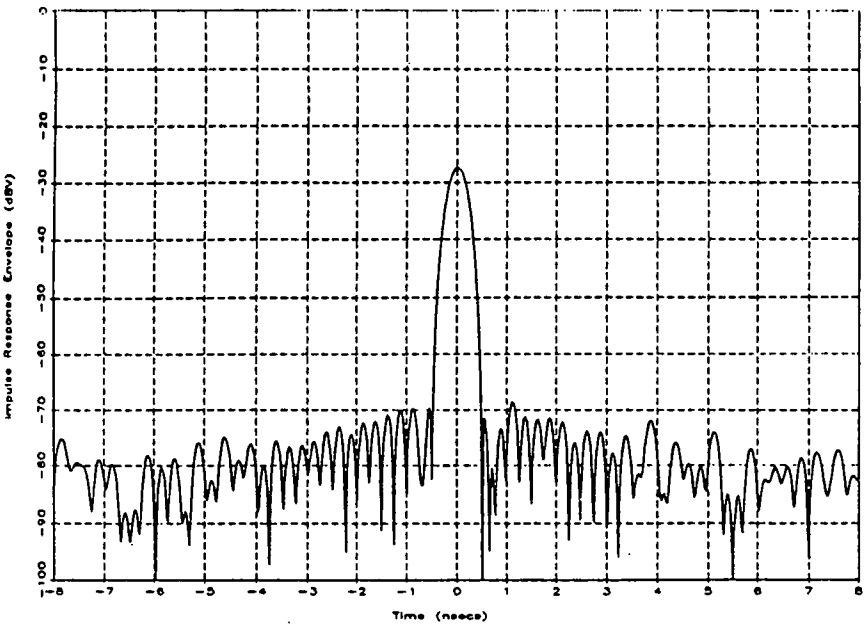

Figure A23

Zero dBsm Point Source with -30 dBsm Noise
Hamming Weighting

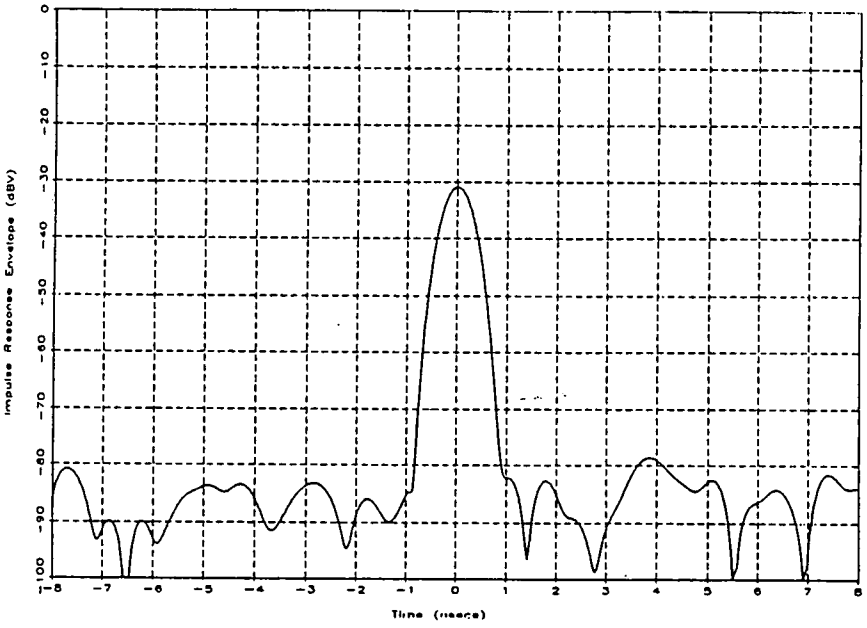

Figure A24

Zero dBsm Source with -30 dBsm Noise
Blackman-Harris Weighting

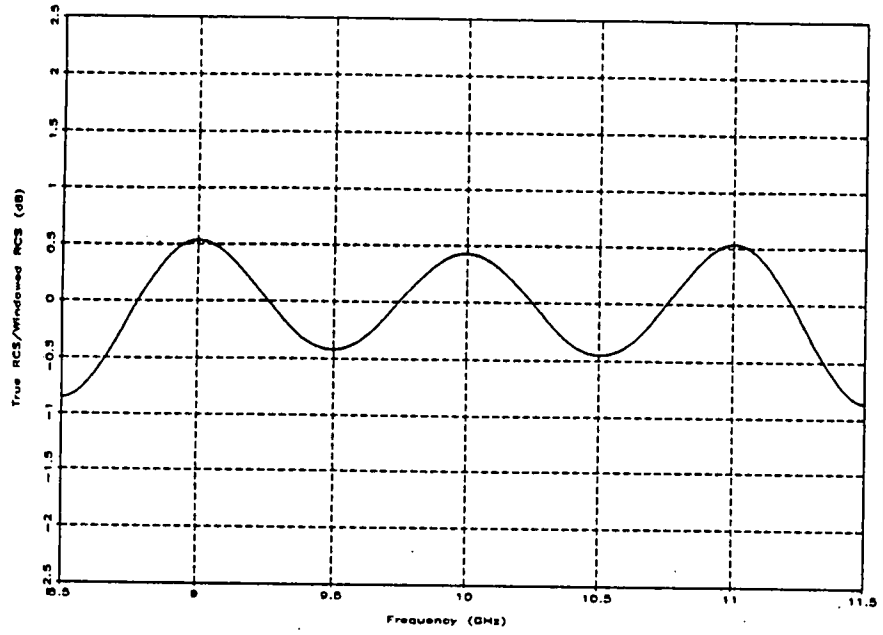

Figure A25

Zero dBsm Point Source with -30 dBsm Noise
Uniform Weighting Edit Gate = .8/B

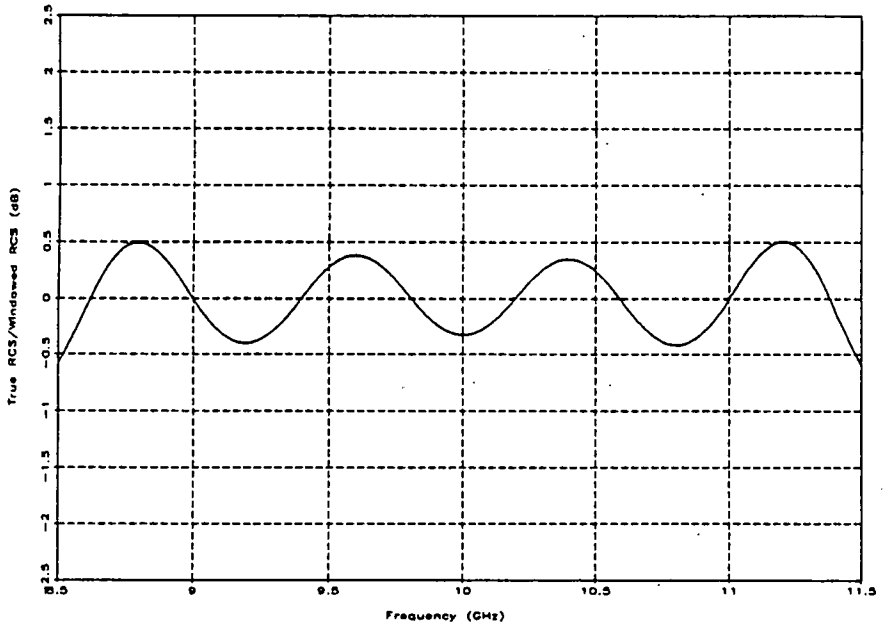

Figure A26

Zero dBsm Source with -30 dBsm Noise
Uniform Weighting Edit Gate = 10/B

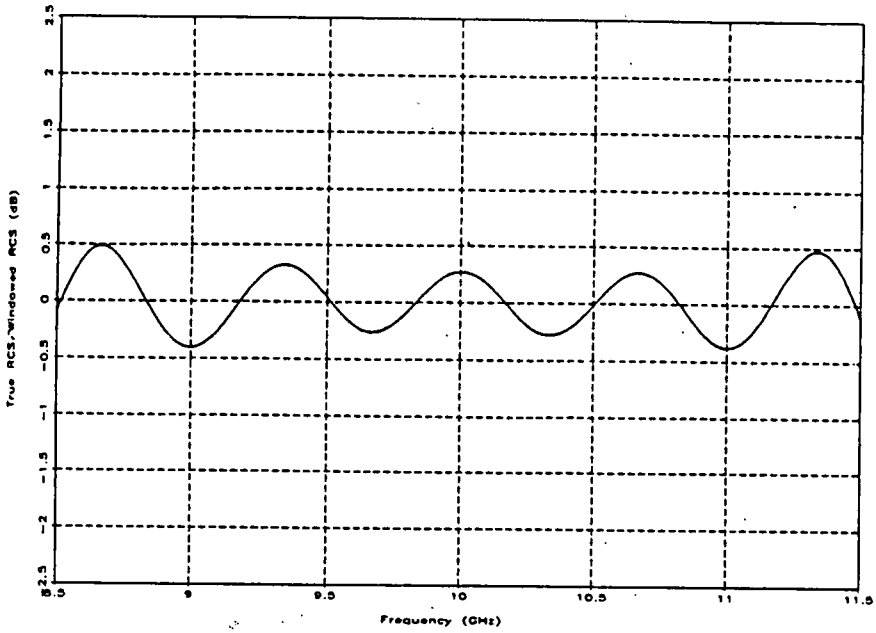

Figure A27

Zero dBsm Point Source with -30 dBsm Noise
Uniform Weighting Edit Gate = 12/B

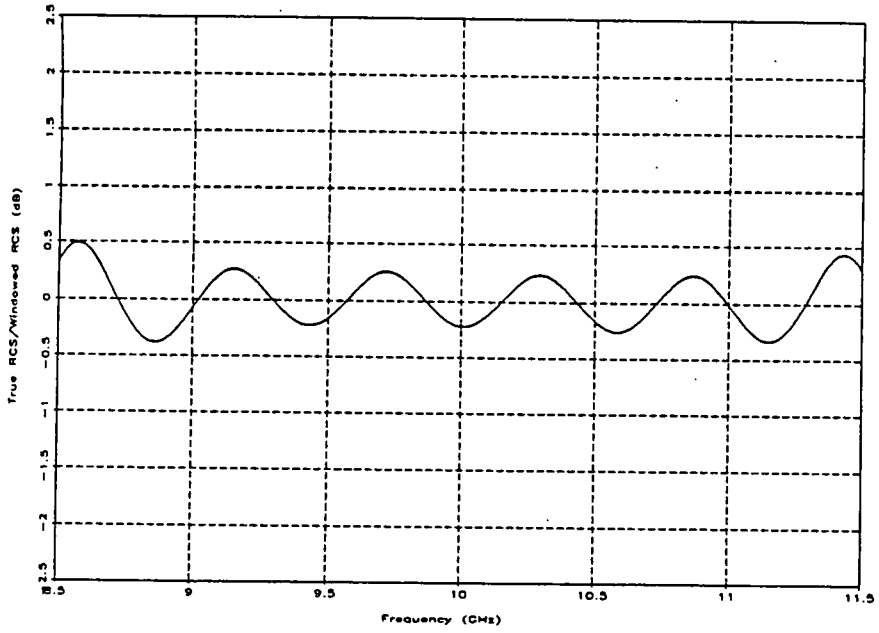

Figure A28

Zero dBsm Source with -30 dBsm Noise
Uniform Weighting Edit Gate = 14/B

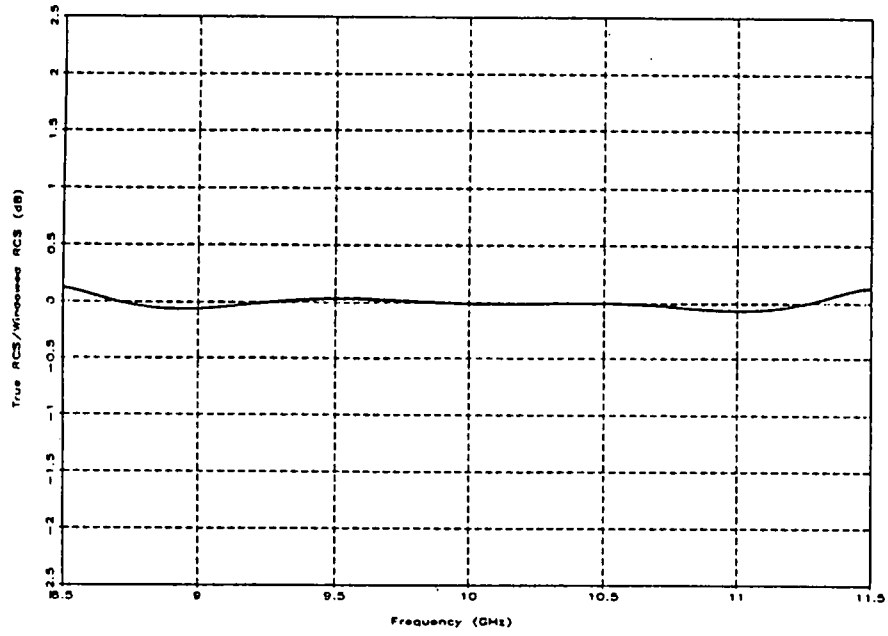

Figure A29

Zero dBsm Point Source with -30 dBsm Noise
Hann Weighting Edit Gate = 8/B

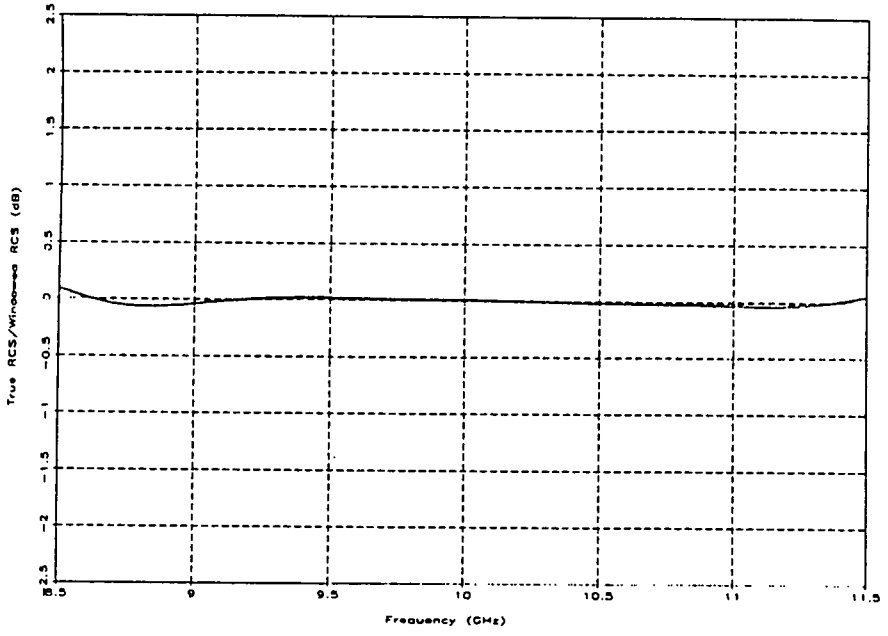

Figure A30

Zero dBsm Source with -30 dBsm Noise
Hann Weighting Edit Gate = 10/B

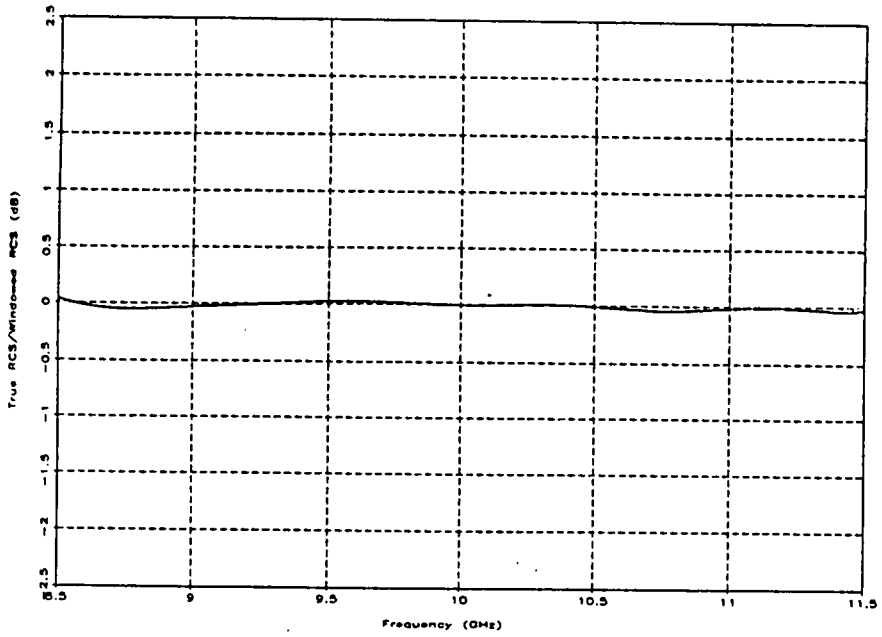

Figure A31

Zero dBsm Point Source with -30 dBsm Noise
Hann Weighting Edit Gate = 12/B

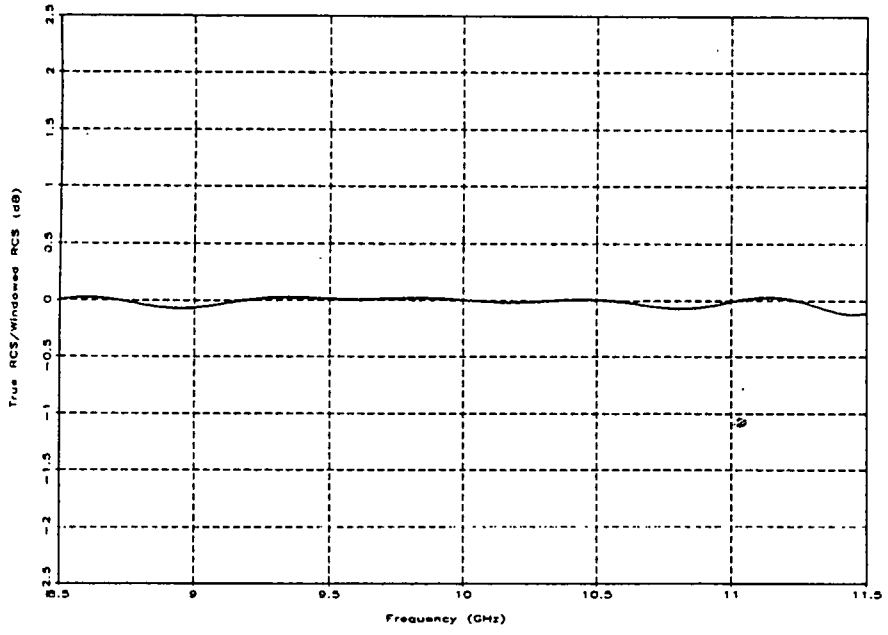

Figure A32

Zero dBsm Source with -30 dBsm Noise
Hann Weighting Edit Gate = 14/B

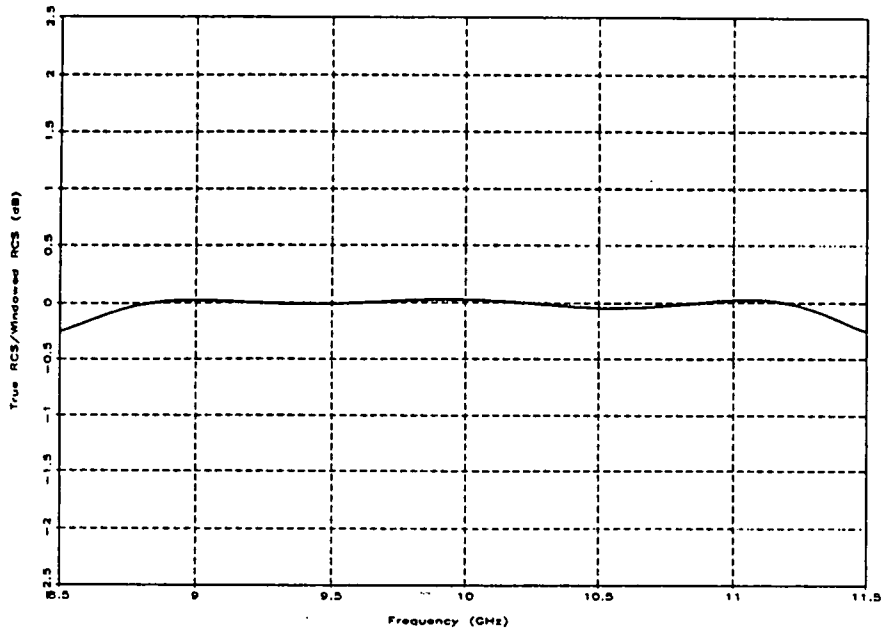

Figure A33

Zero dBsm Point Source with -30 dBsm Noise
Hamming Weighting Edit Gate = 8/B

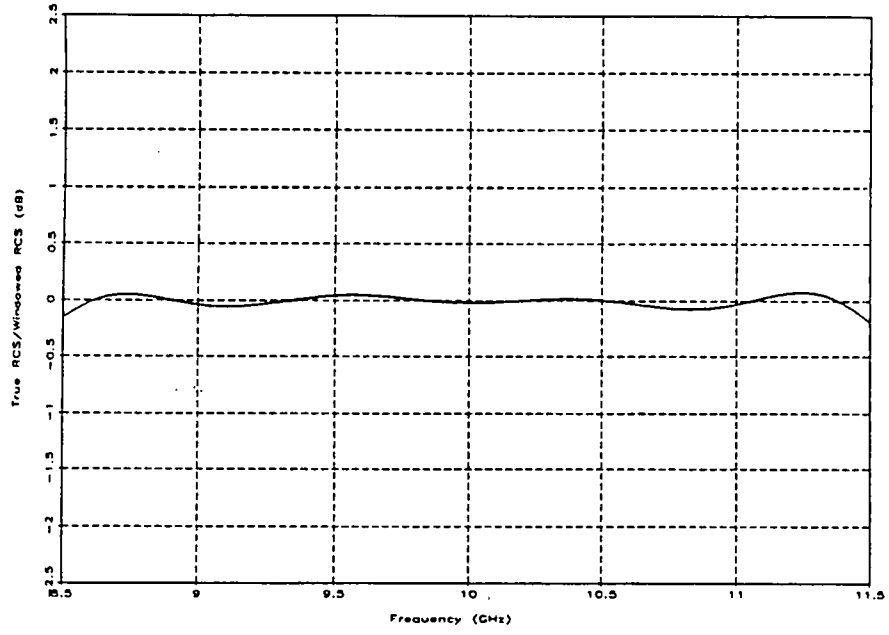

Figure A34

Zero dBsm Source with -30 dBsm Noise
Hamming Weighting Edit Gate = 10/B

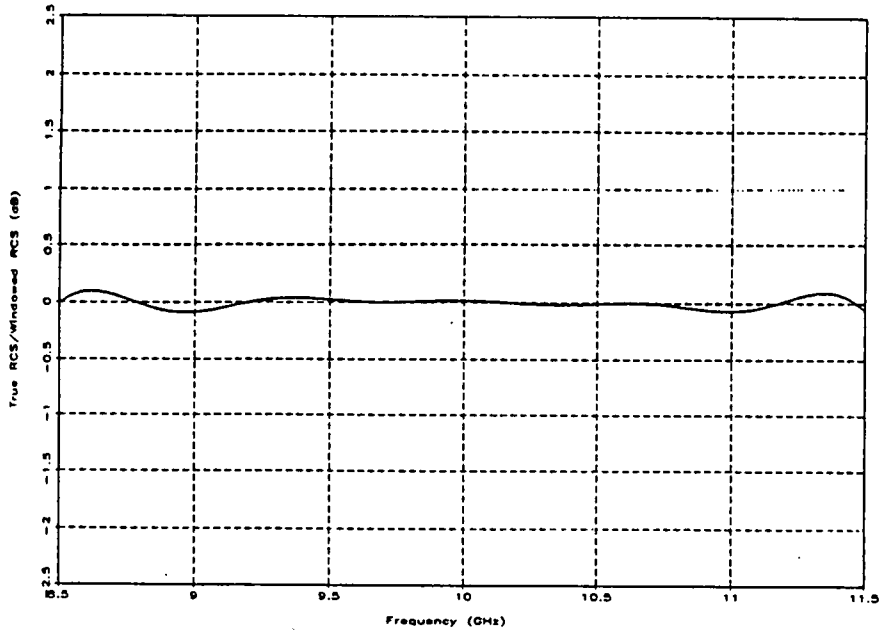

Figure A35

Zero dBsm Point Source with -30 dBsm Noise
Hamming Weighting Edit Gate = 12/B

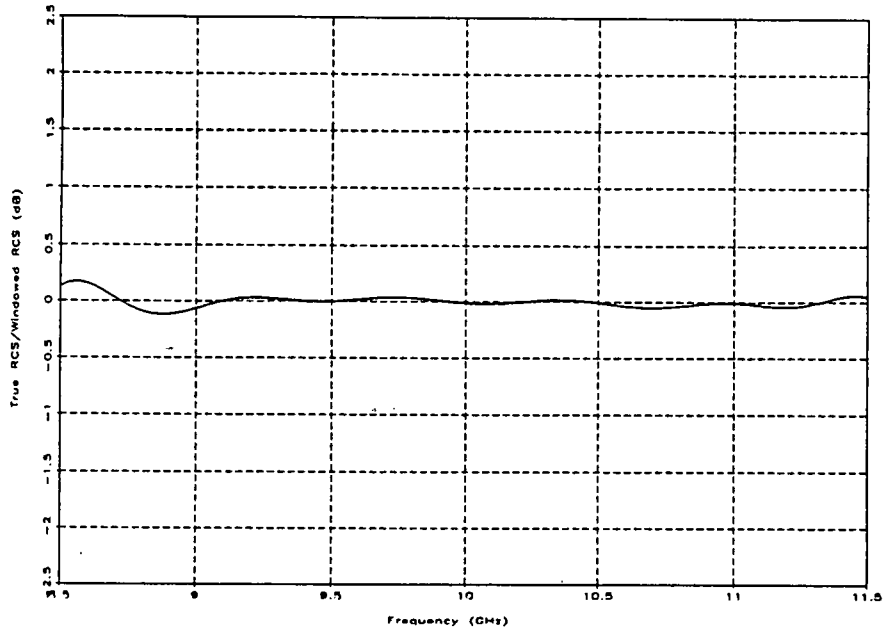

Figure A36

Zero dBsm Source with -30 dBsm Noise
Hamming Weighting Edit Gate = 14/B

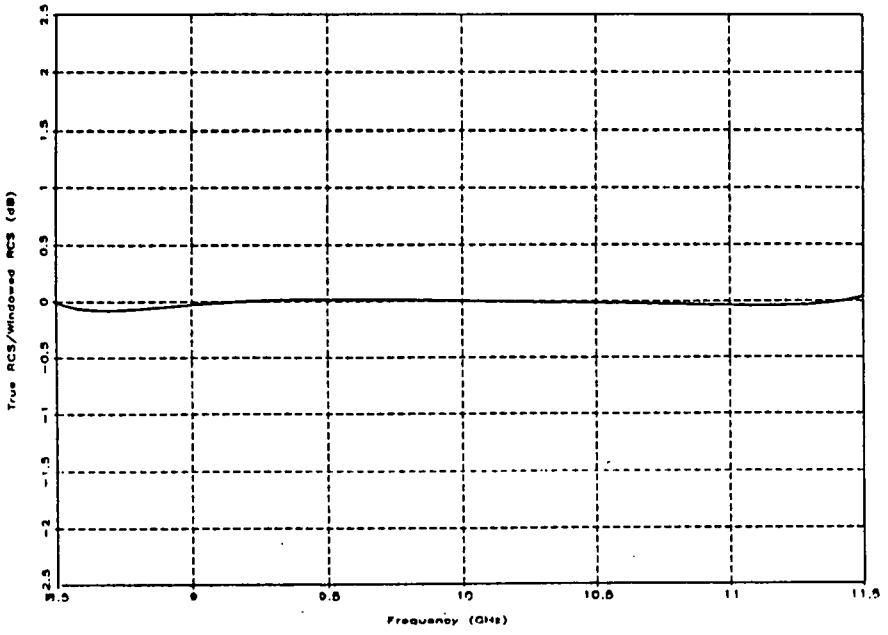

Figure A37

Zero dBsm Point Source with -30 dBsm Noise
Blackman-Harris Weighting Edit Gate = 8/B

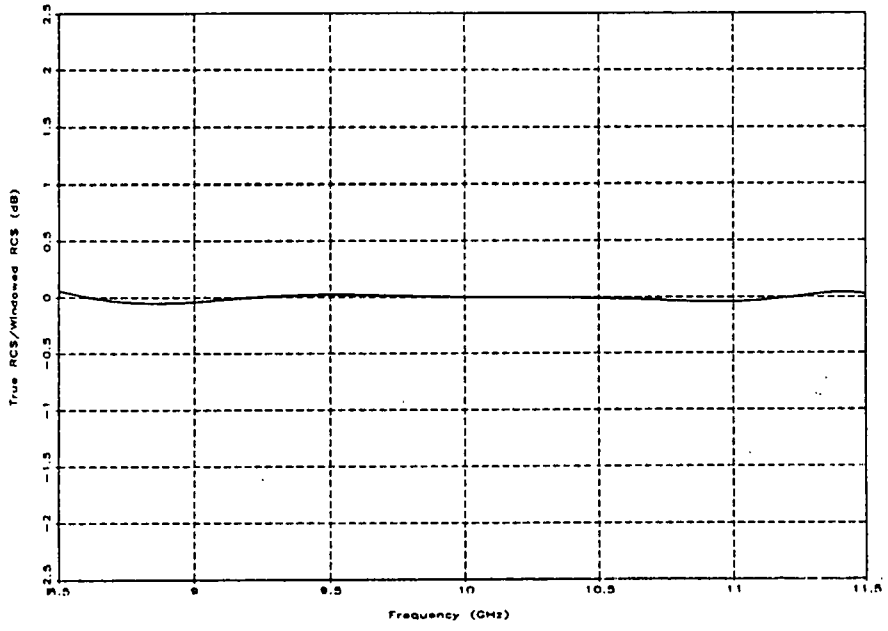

Figure A38

Zero dBsm Source with -30 dBsm Noise
Blackman-Harris Weighting Edit Gate = 10/B

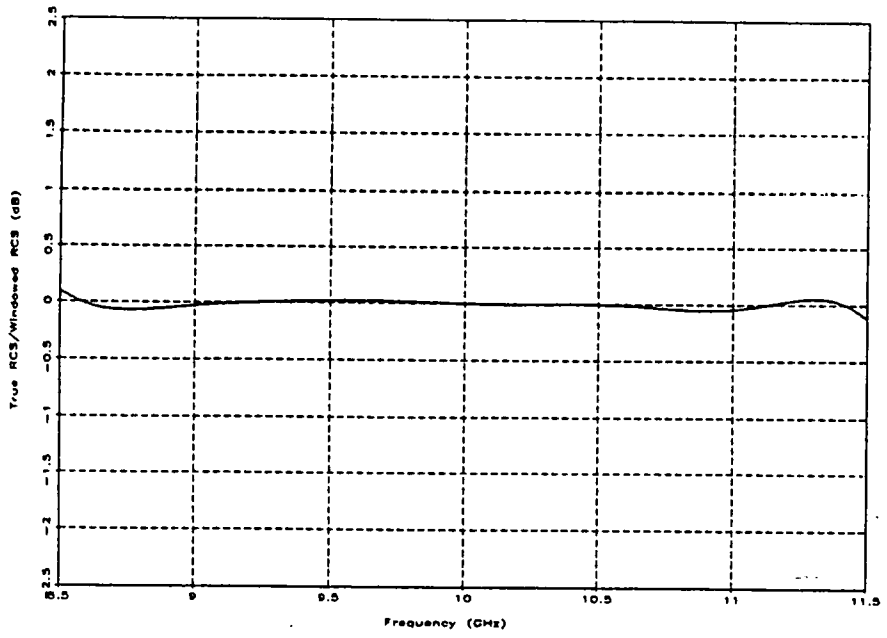

Figure A39

Zero dBsm Point Source with -30 dBsm Noise
Blackman-Harris Weighting Edit Gate = 12/B

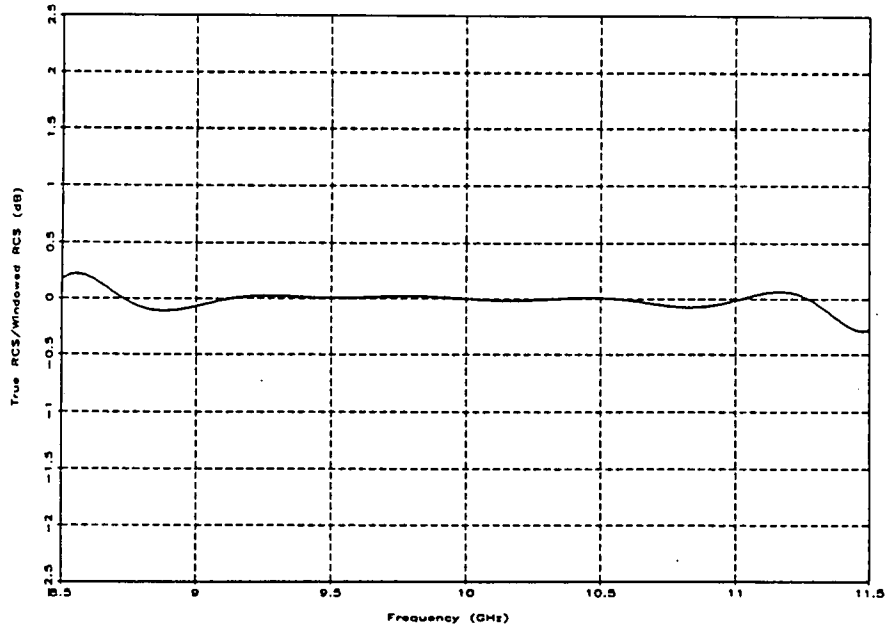

Figure A40

Zero dBsm Source with -30 dBsm Noise
Blackman-Harris Weighting Edit Gate = 14/B

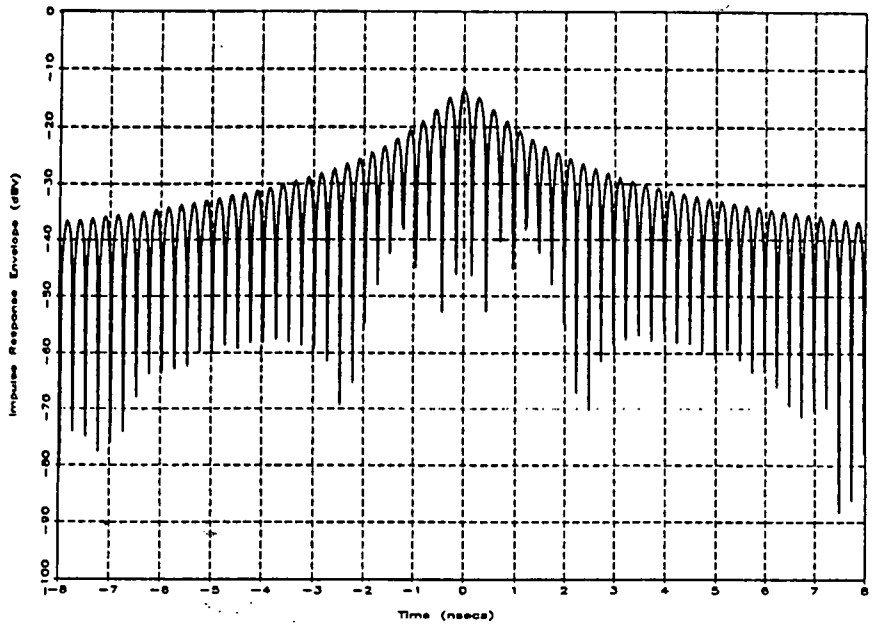

Figure A41

Inverted Cosine Source with -30 dBsm Noise
Uniform Weighting

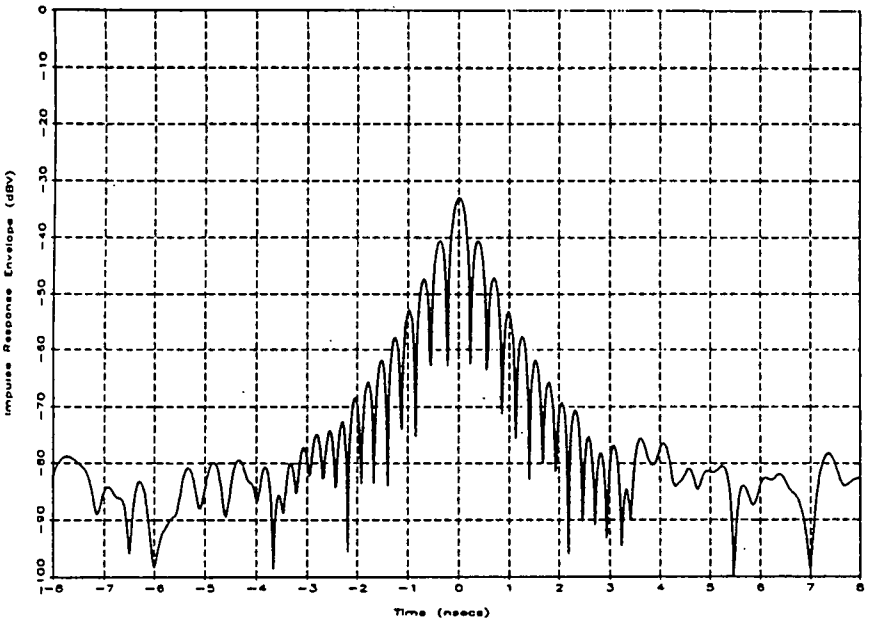

Figure A42

Inverted Cosine Source with -30 dBsm Noise
Hann Weighting

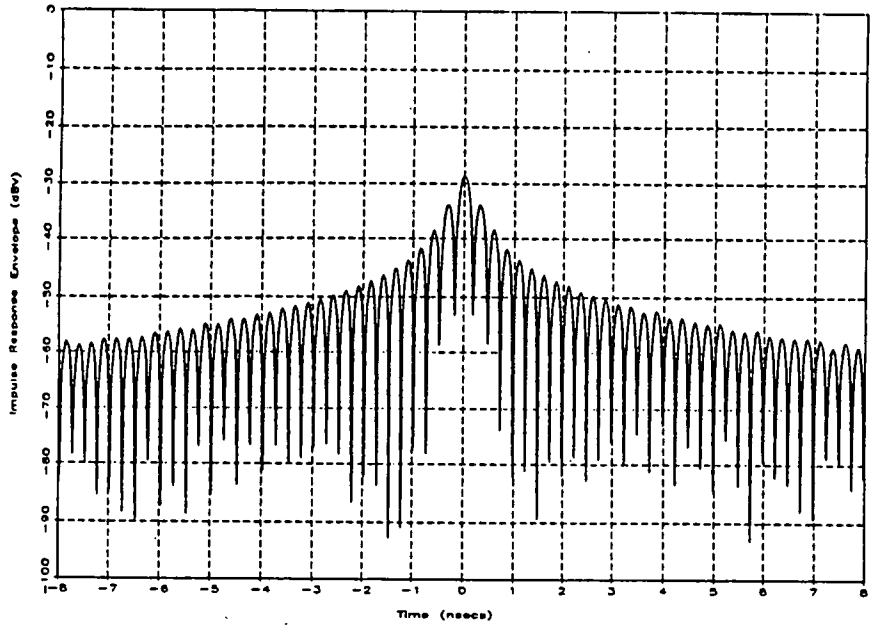

Figure A43

Inverted Cosine Source with -30 dBsm Noise
Hamming Weighting

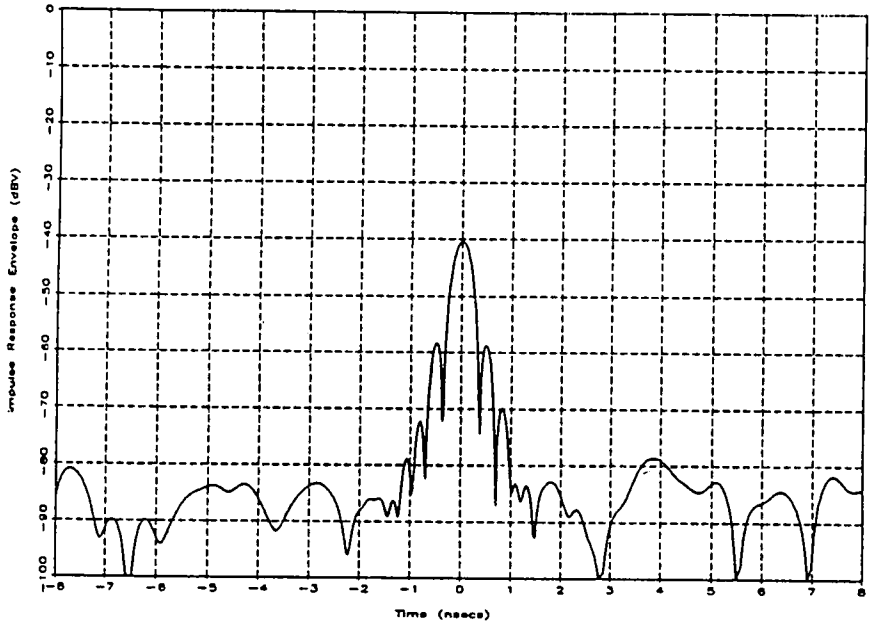

Figure A44

Inverted Cosine Source with -30 dBsm Noise
Blackman-Harris Weighting

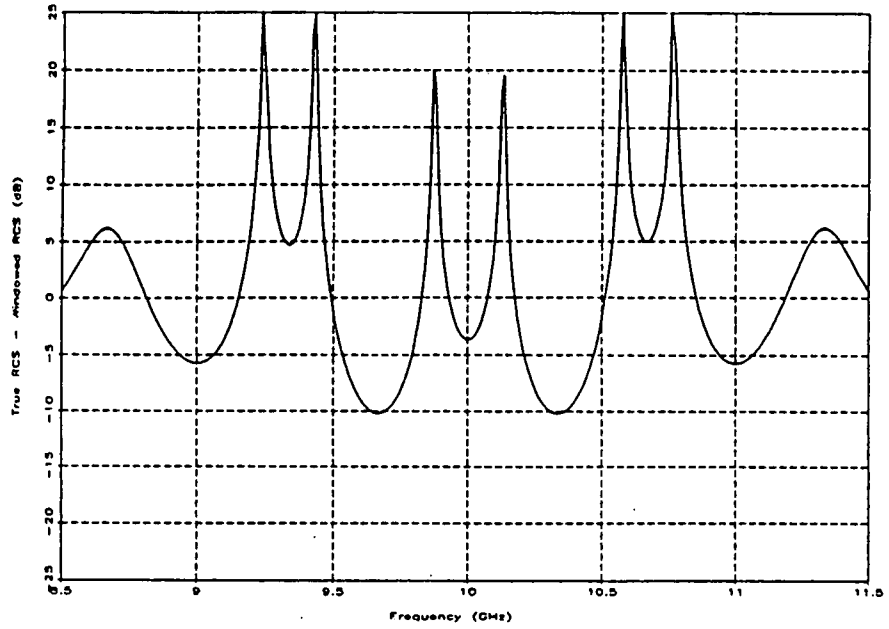

Figure A45

Inverted Cosine Source with -30 dBsm Noise
Uniform Weighting Edit Gate = 12/B

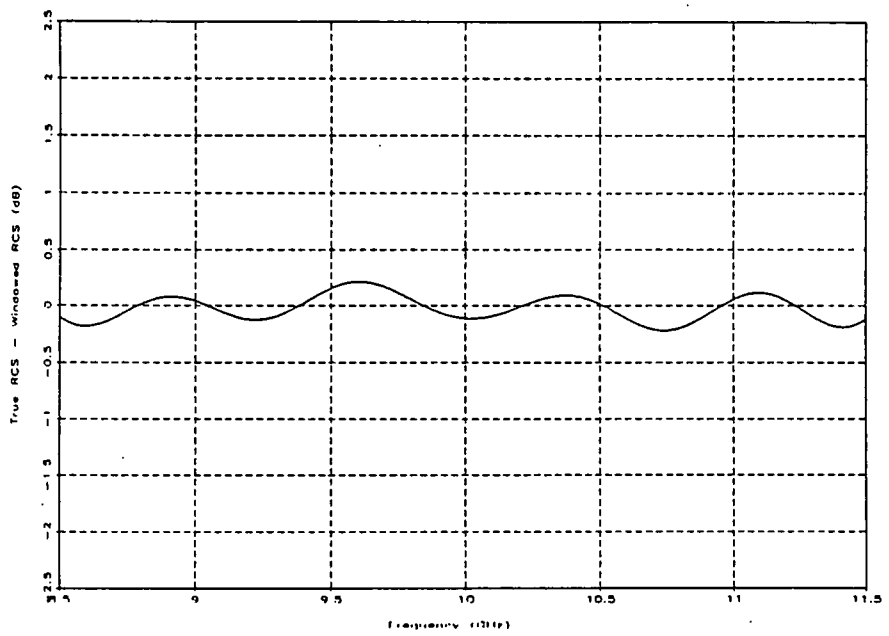

Figure A46

Inverted Cosine Source with -30 dBsm Noise
Hann Weighting Edit Gate = 12/B

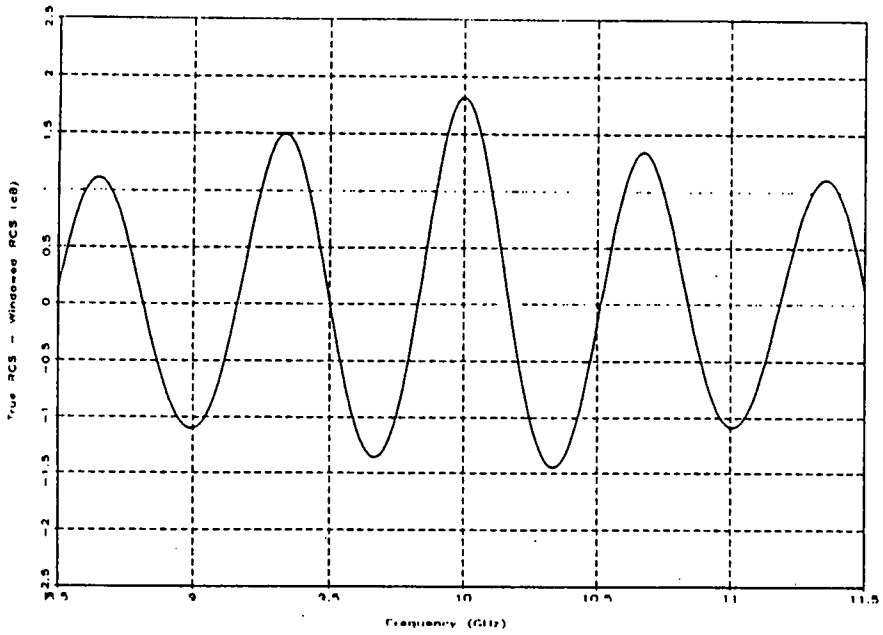

Figure A47

Inverted Cosine Source with -30 dBsm Noise
Hamming Weighting Edit Gate = 12/B

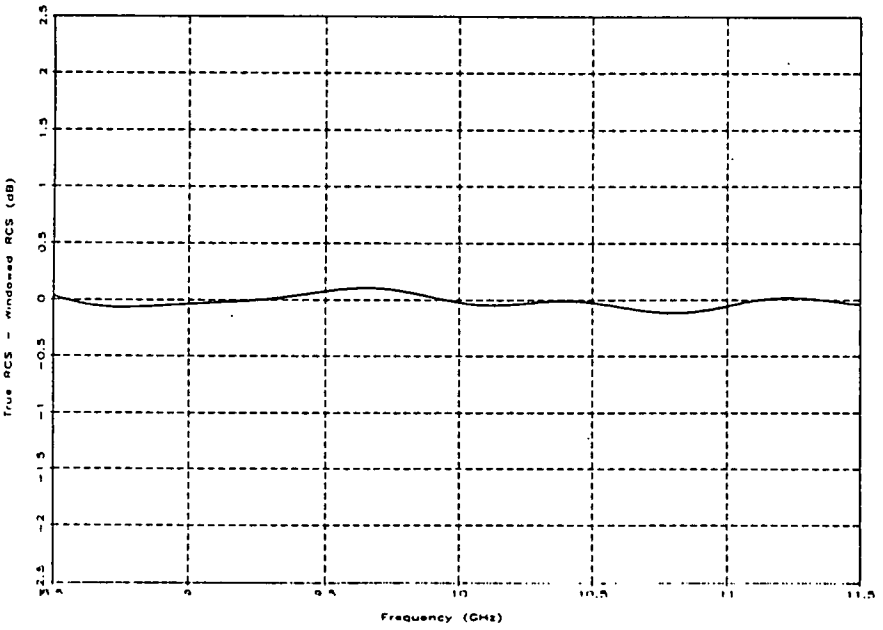

Figure A48

Inverted Cosine Source with -30 dBsm Noise
Blackman-Harris Weighting Edit Gate = 12/B

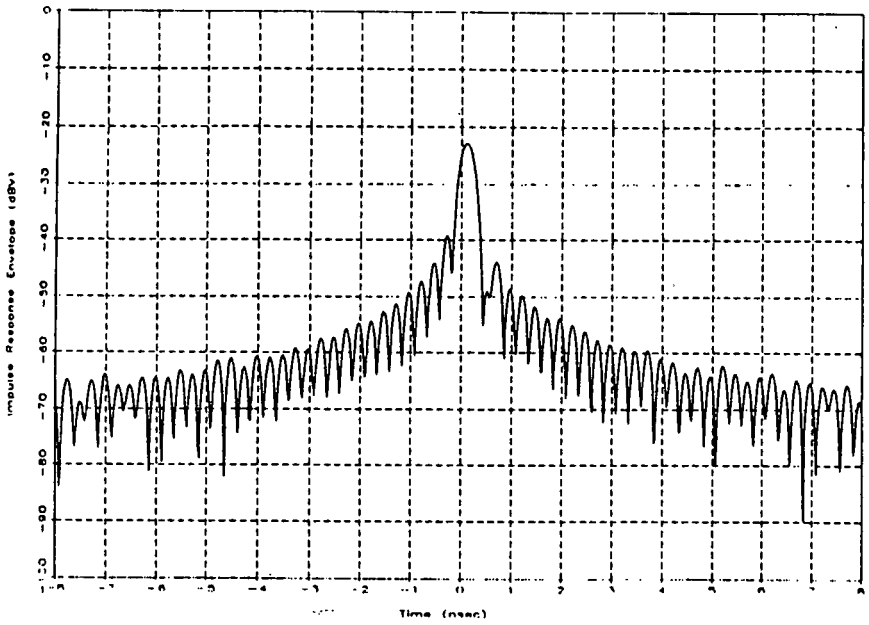

Figure A49

Single Wire Resonant Near 10 GHz with -30 dBsm Noise
Uniform Weighting

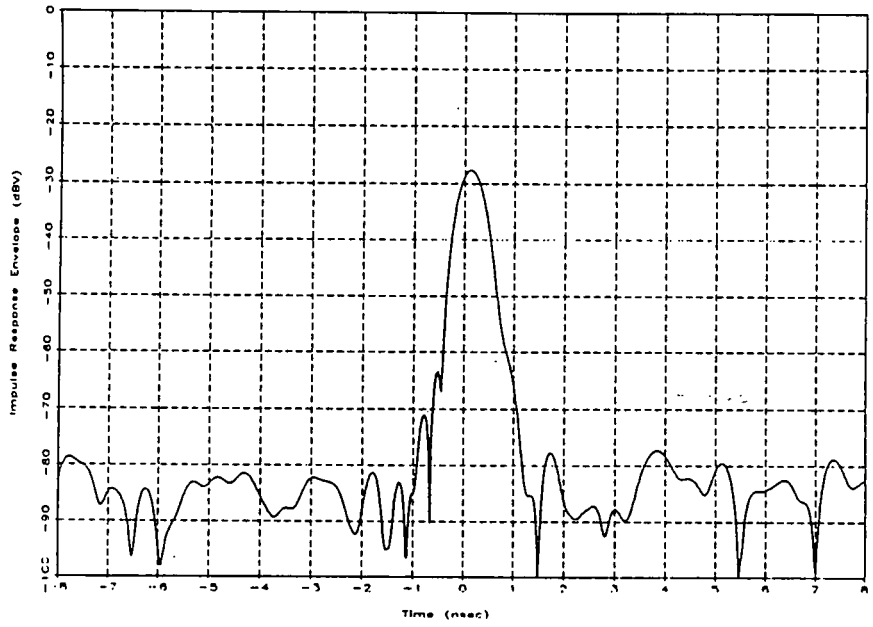

Figure A50

Single Wire Resonant Near 10 GHz with -30 dBsm Noise
Hann Weighting

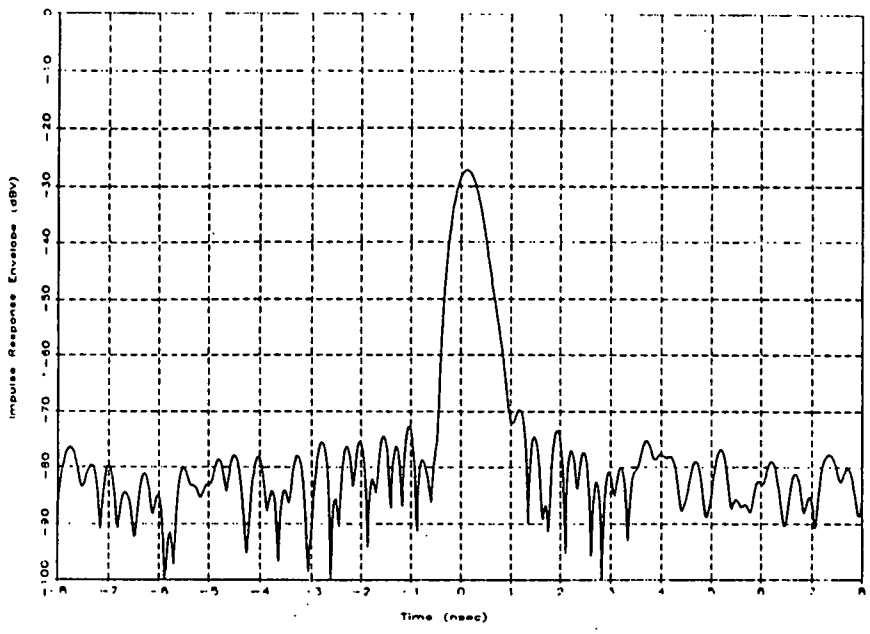

Figure A51

Single Wire Resonant Near 10 GHz with -30 dBsm Noise
Hamming Weighting

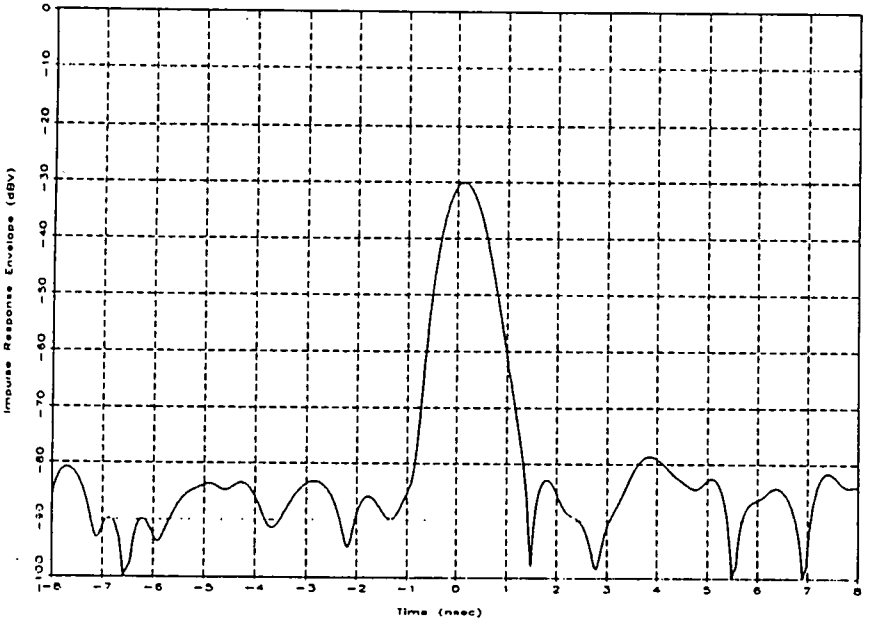

Figure A52

Single Wire Resonant Near 10 GHz with -30 dBsm Noise
Blackman-Harris Weighting

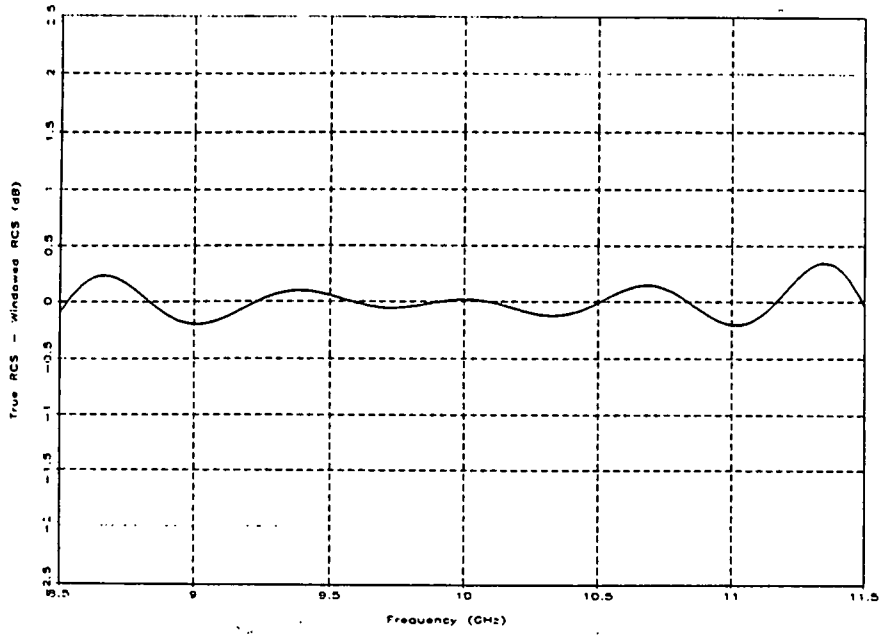

Figure A53

Single Wire Resonant Near 10 GHz with -30 dBsm Noise
Uniform Weighting Edit Gate = 12/B

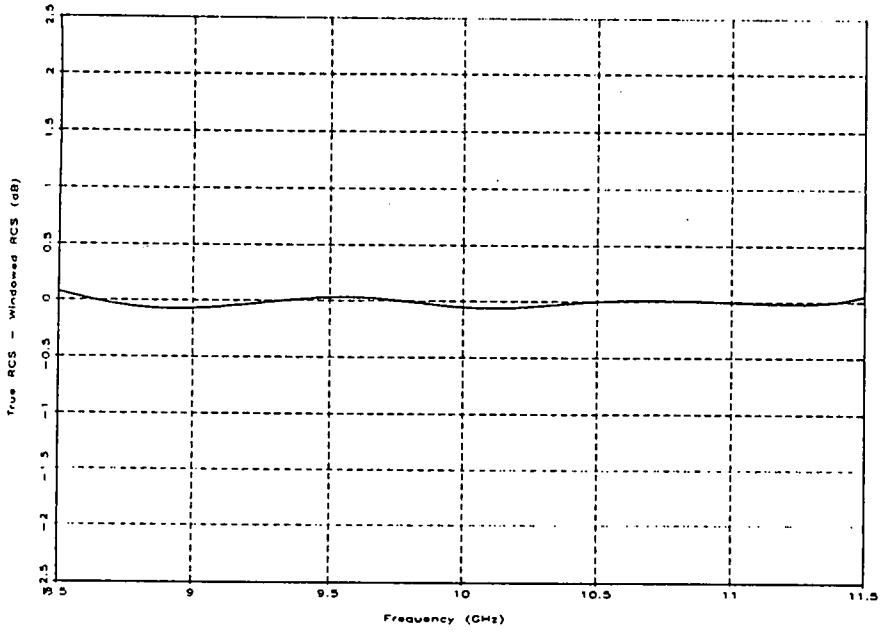

Figure A54

Single Wire Resonant Near 10 GHz with -30 dBsm Noise
Hann Weighting Edit Gate = 12/B

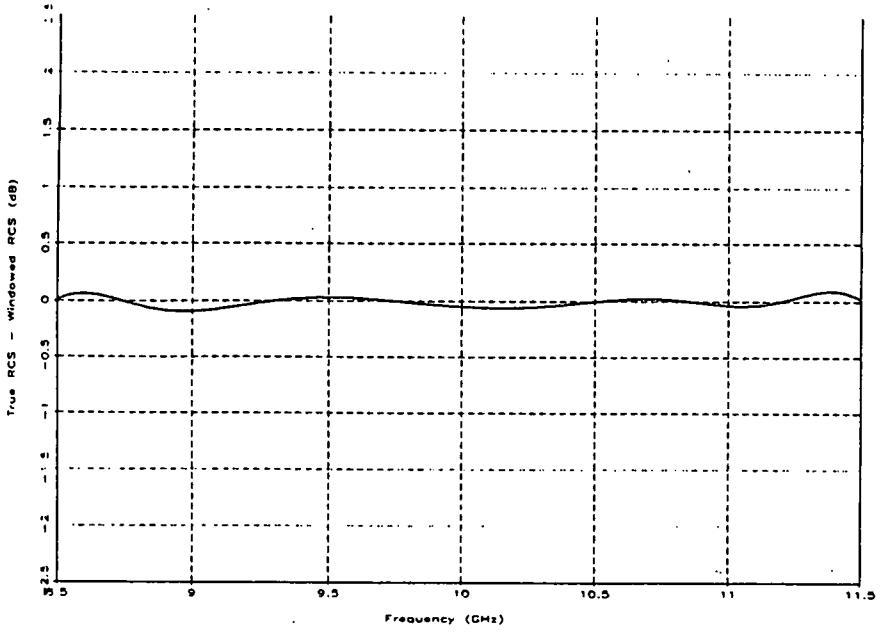

Figure A55

Single Wire Resonant Near 10 GHz with -30 dBsm Noise
Hamming Weighting Edit Gate = 12/B

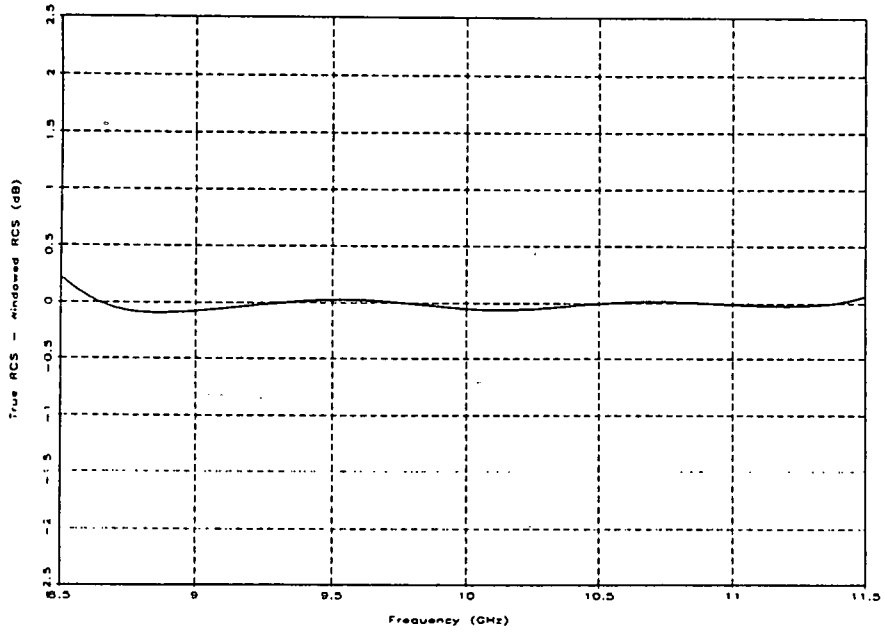

Figure A56

Single Wire Resonant Near 10 GHz with -30 dBsm Noise
Blackman-Harris Weighting Edit Gate = 12/B

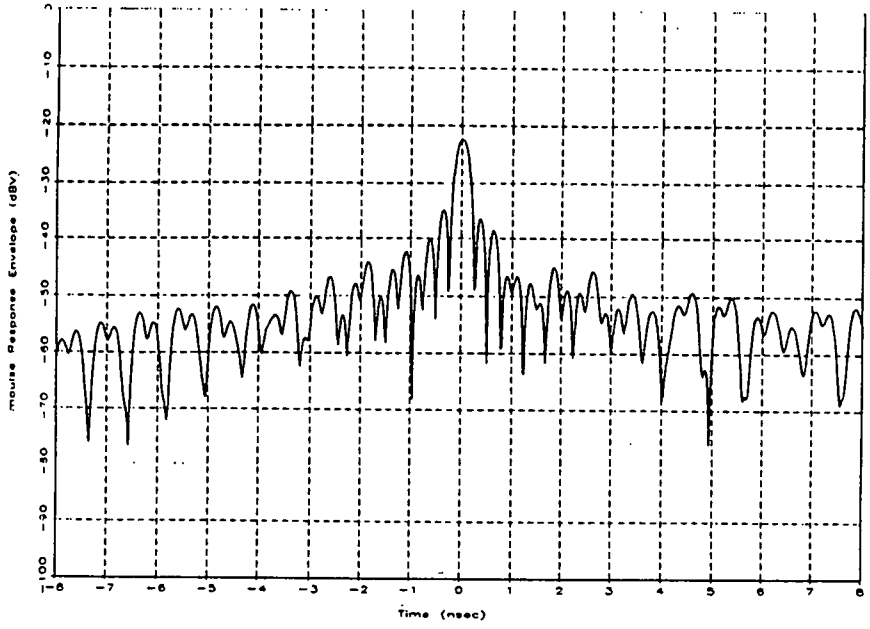

Figure A57

Single Wire Resonant Near 500 MHz with -30 dBsm Noise
Uniform Weighting

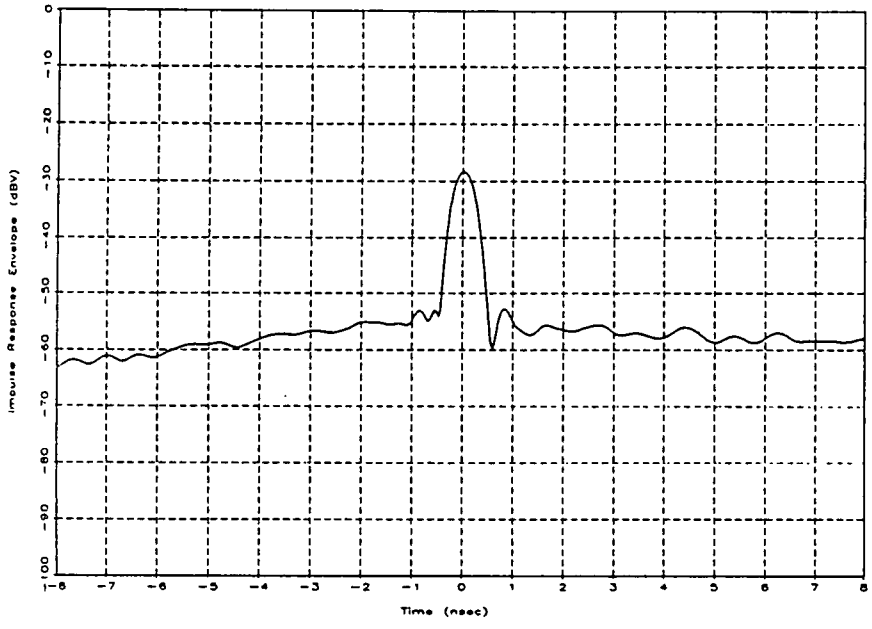

Figure A58

Single Wire Resonant Near 500 MHz with -30 dBsm Noise
Hann Weighting

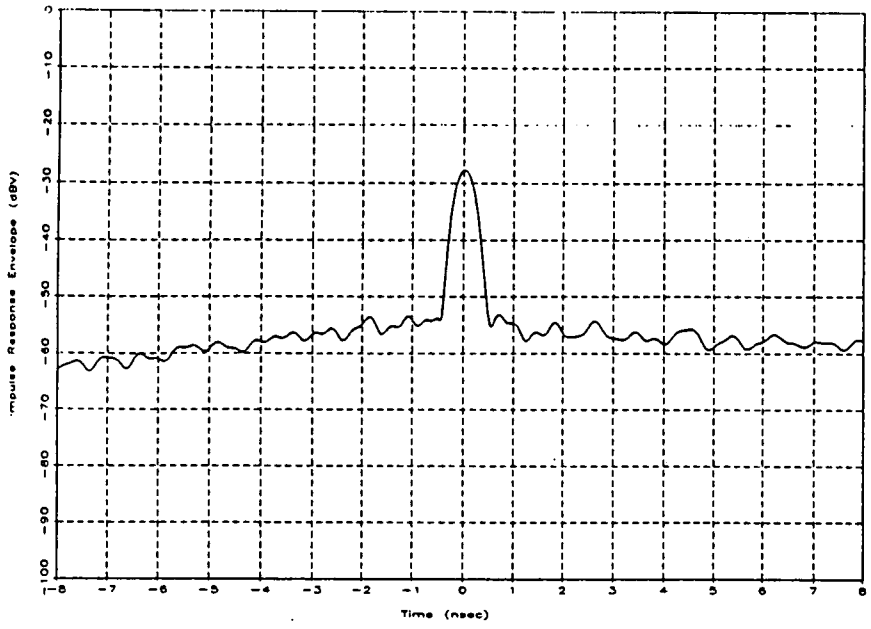

Figure A59

Single Wire Resonant Near 500 MHz with -30 dBsm Noise
Hamming Weighting

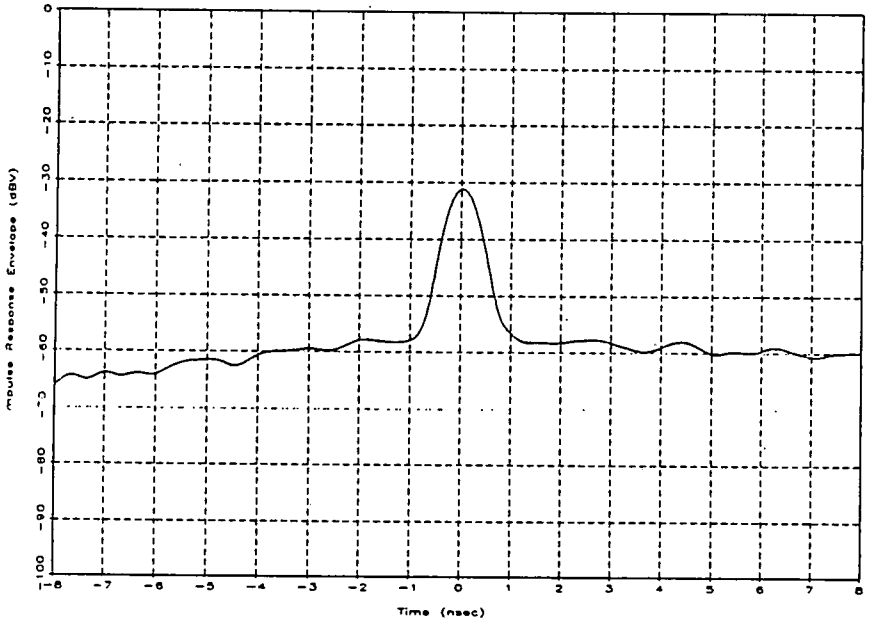

Figure A60

Single Wire Resonant Near 500 MHz with -30 dBsm Noise
Blackman-Harris Weighting

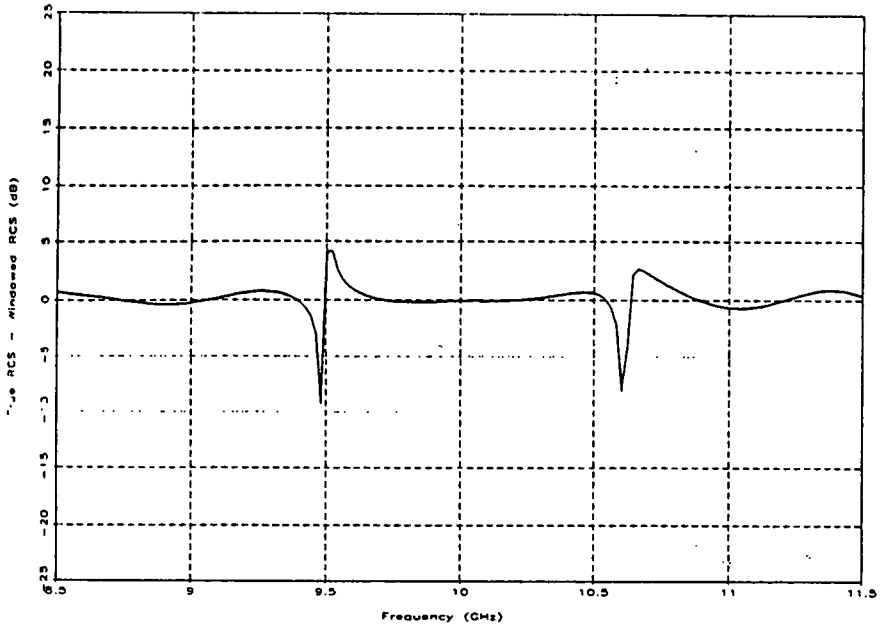

Figure A61

Single Wire Resonant Near 500 MHz with -30 dBsm Noise
Uniform Weighting Edit Gate = 12/B

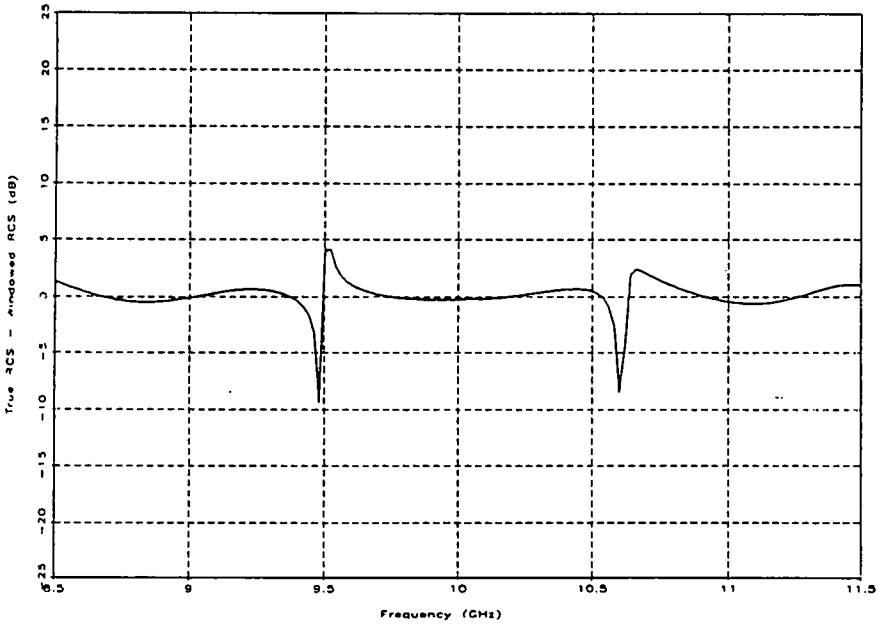

Figure A62

Single Wire Resonant Near 500 MHz with -30 dBsm Noise
Hann Weighting Edit Gate = 12/B

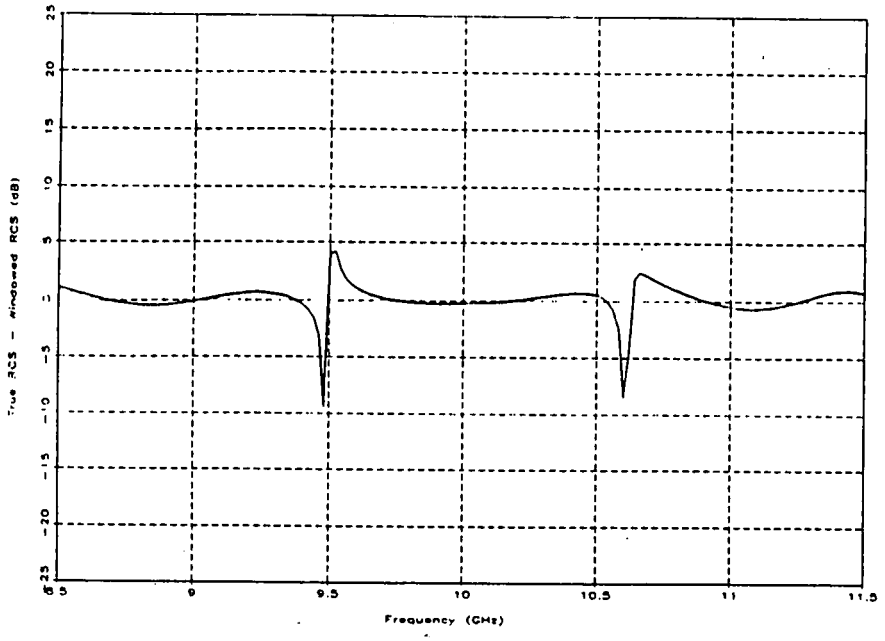

Figure A63

Single Wire Resonant Near 500 MHz with -30 dBsm Noise
Hamming Weighting Edit Gate = 12/B

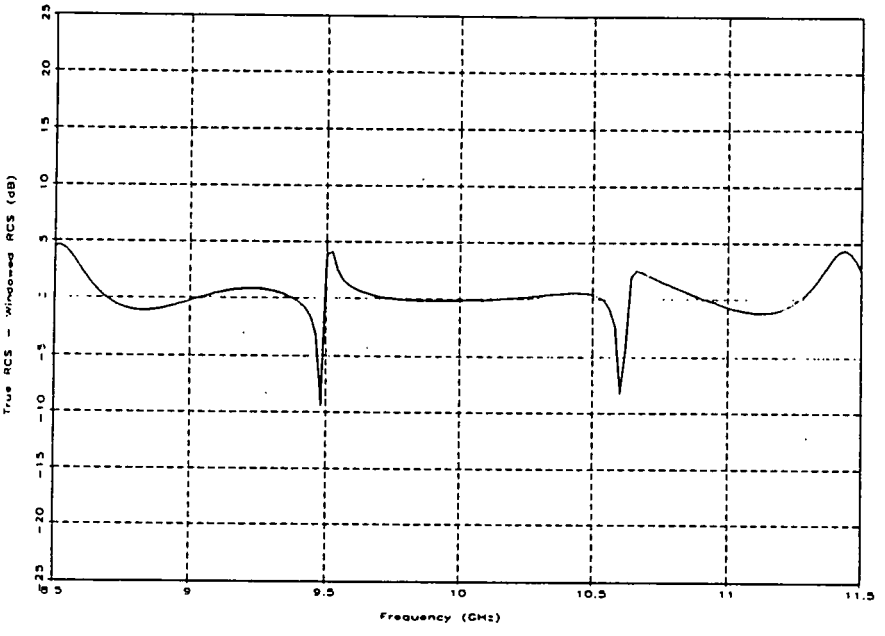

Figure A64

Single Wire Resonant Near 500 MHz with -30 dBsm Noise
Blackman-Harris Weighting Edit Gate = 12/B

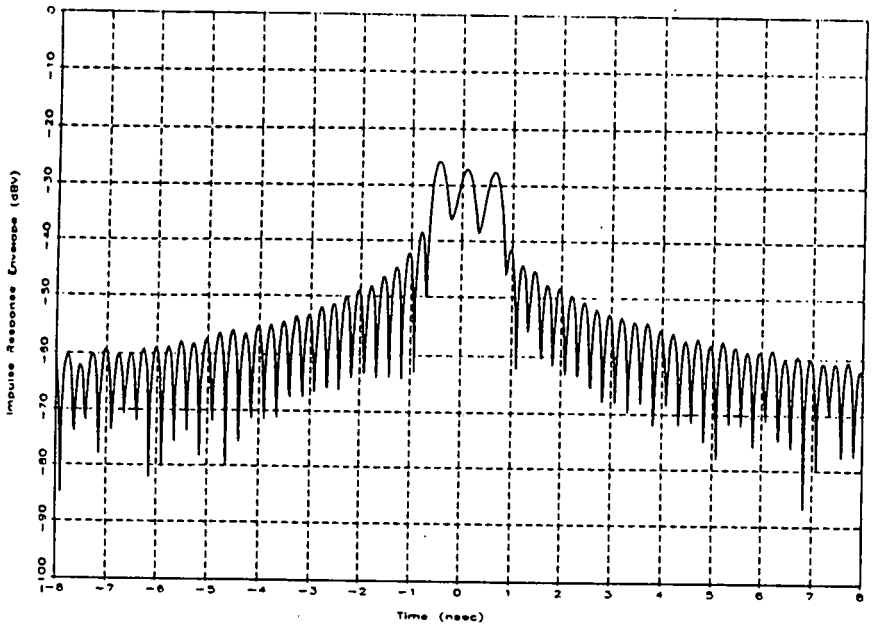

Figure A65

Three Wires Resonant Near 10 GHz with -30 dBsm Noise
Uniform Weighting

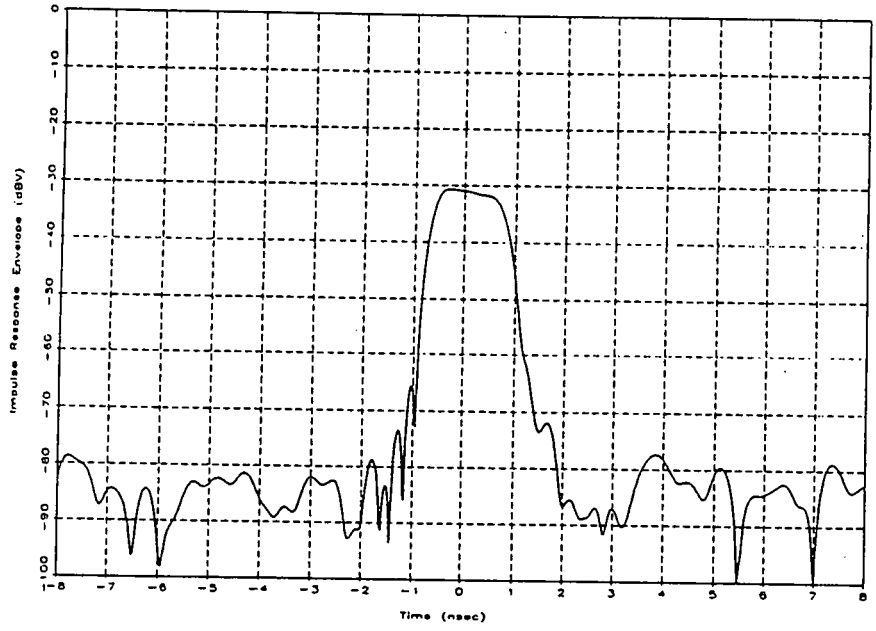

Figure A66

Three Wires Resonant Near 10 GHz with -30 dBsm Noise
Hann Weighting

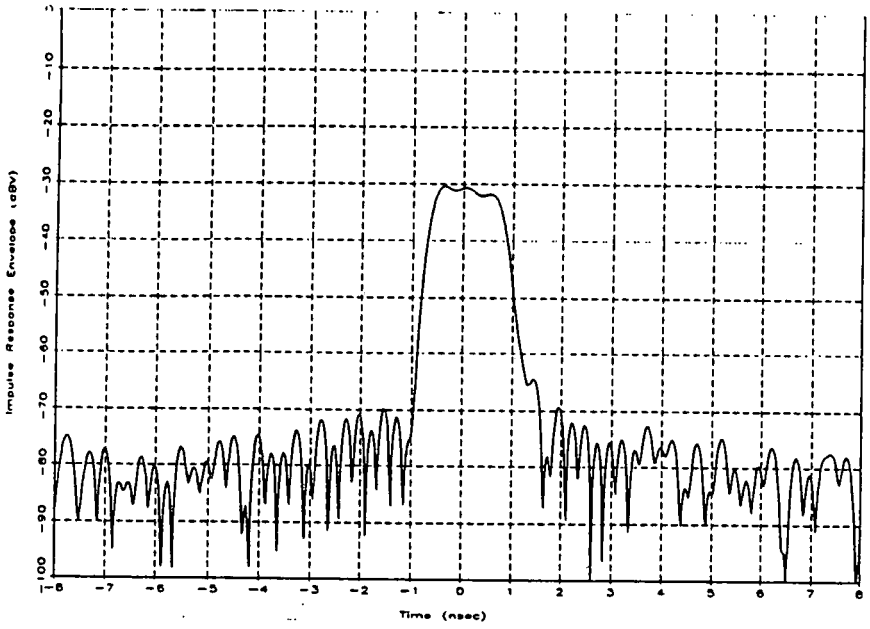

Figure A67

Three Wires Resonant Near 10 GHz with -30 dBsm Noise
Hamming Weighting

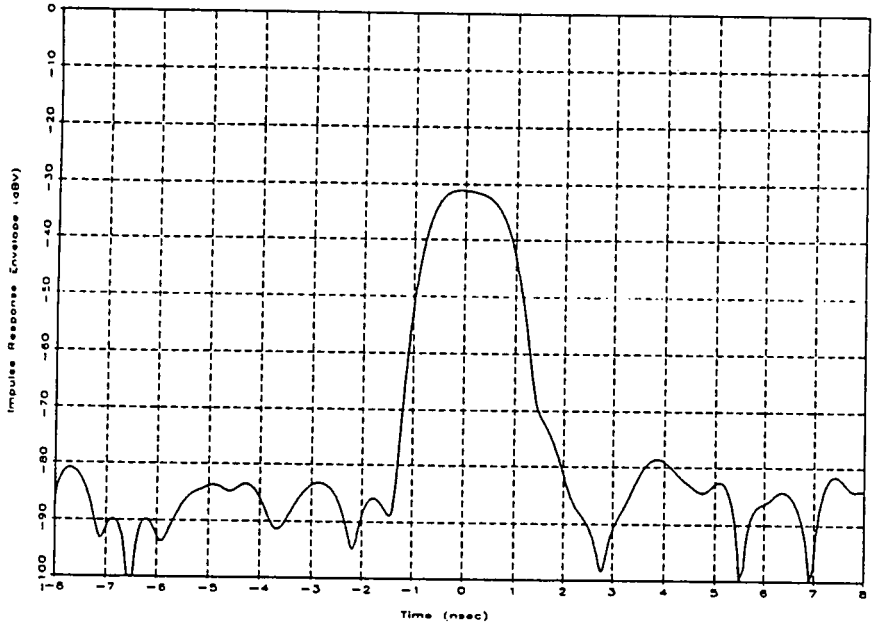

Figure A68

Three Wires Resonant Near 10 GHz with -30 dBsm Noise
Blackman-Harris Weighting

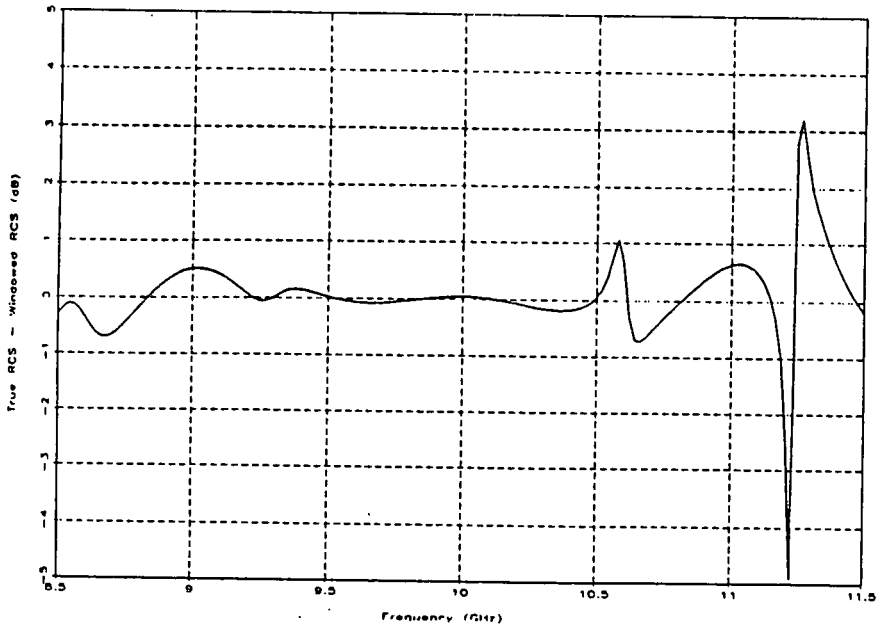

Figure A69

Three Wires Resonant Near 10 GHz with -30 dBsm Noise
Uniform Weighting Edit Gate = 12/B

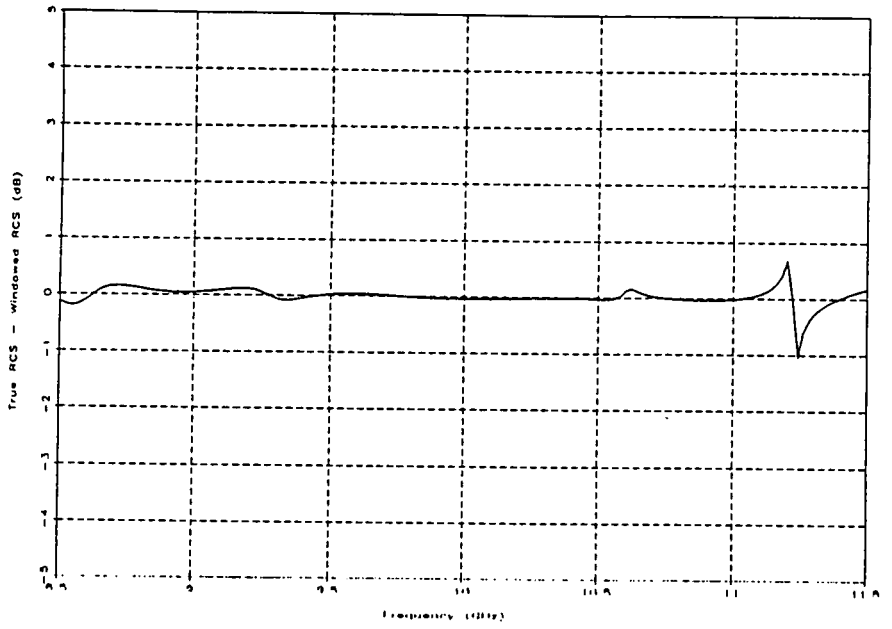

Figure A70

Three Wires Resonant Near 10 GHz with -30 dBsm Noise
Hann Weighting Edit Gate = 12/B

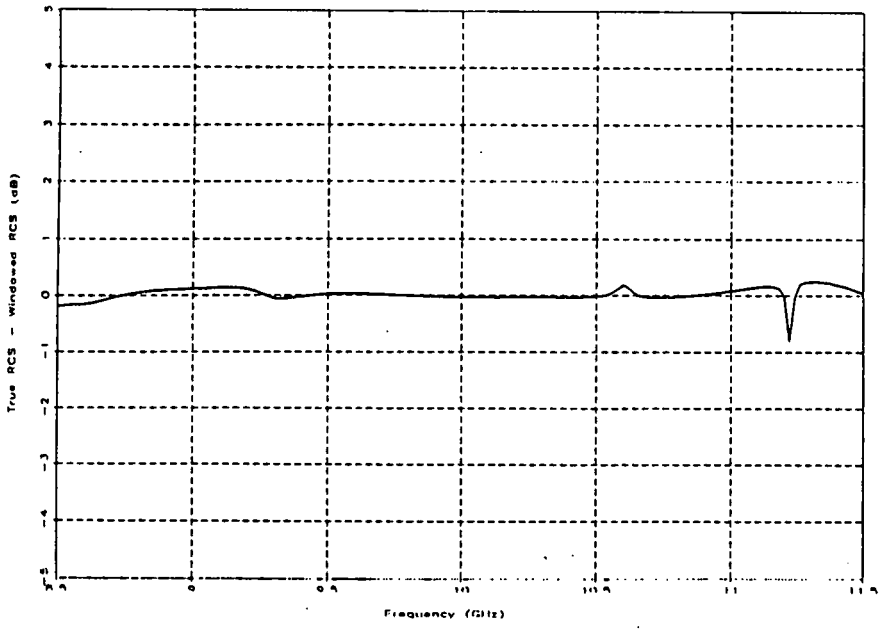

Figure A71

Three Wires Resonant Near 10 GHz with -30 dBsm Noise
Hamming Weighting Edit Gate = 12/B

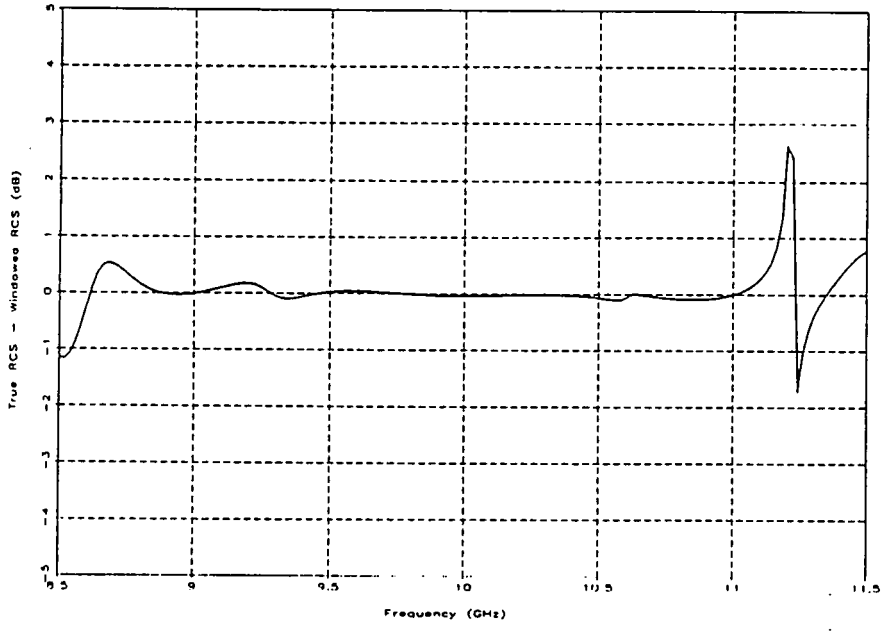

Figure A72

Three Wires Resonant Near 10 GHz with -30 dBsm Noise
Blackman-Harris Weighting Edit Gate = 12/B

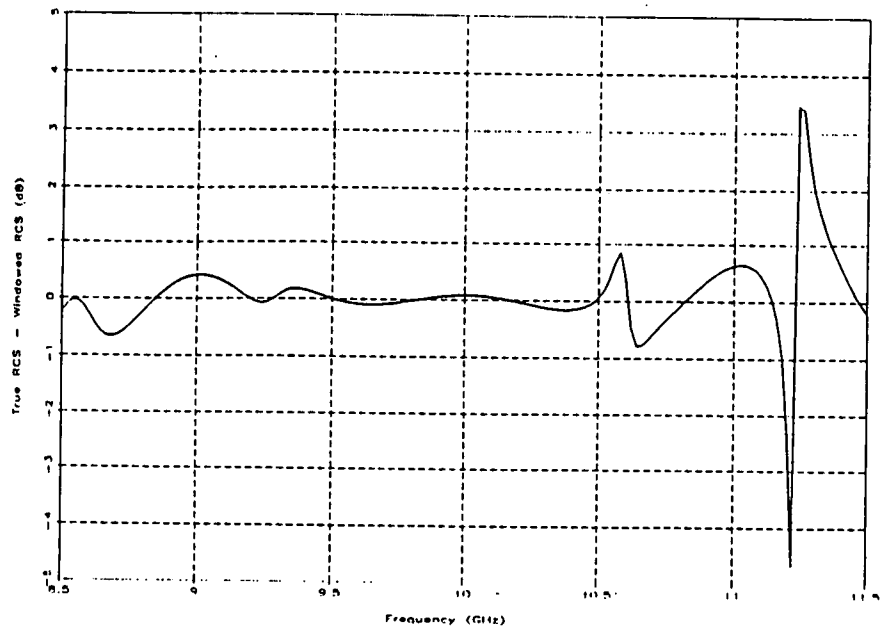

Figure A73

Three Wires Resonant Near 10 GHz without Noise
Uniform Weighting Edit Gate = 12/B

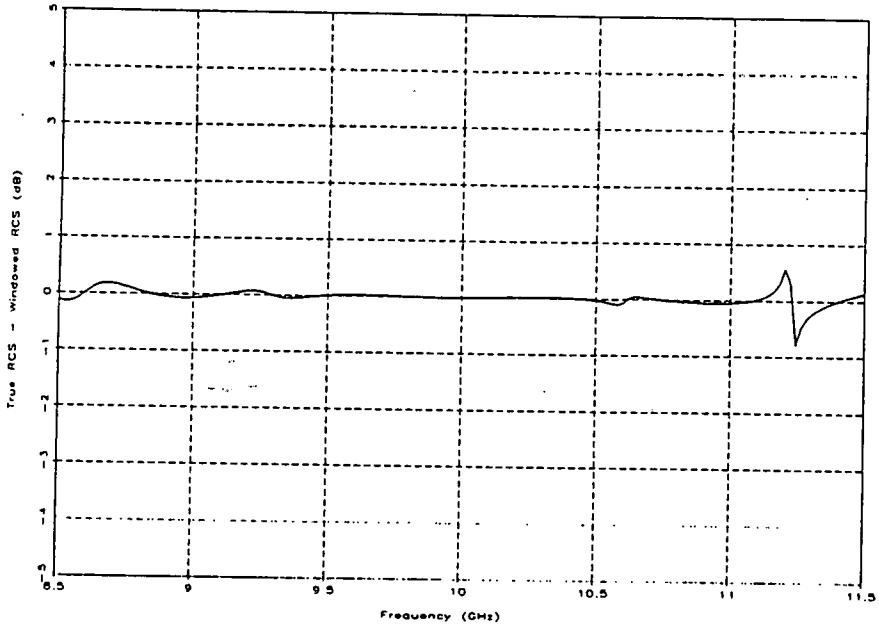

Figure A74

Three Wires Resonant Near 10 GHz without Noise
Hann Weighting Edit Gate = 12/B

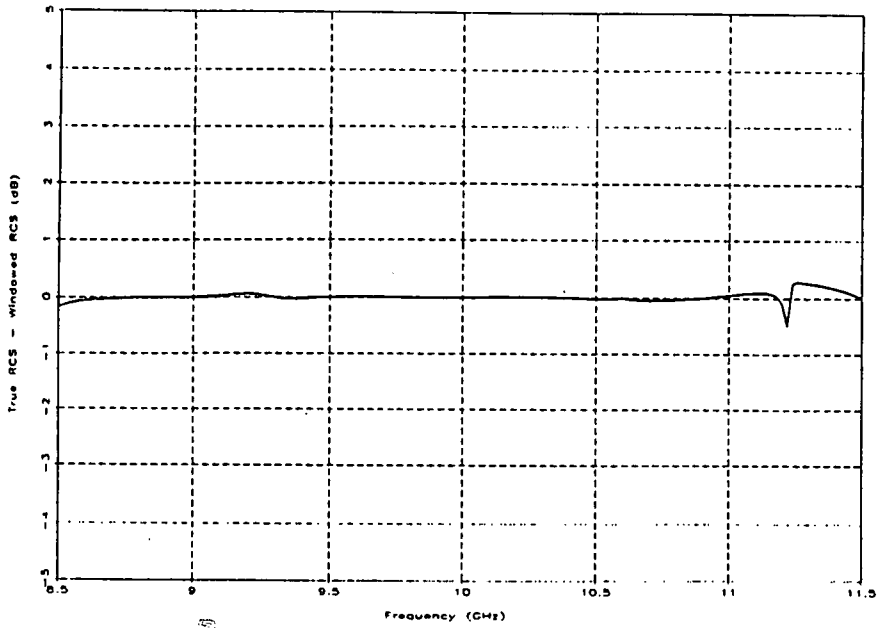

Figure A75

Three Wires Resonant Near 10 GHz without Noise
Hamming Weighting Edit Gate = 12/B

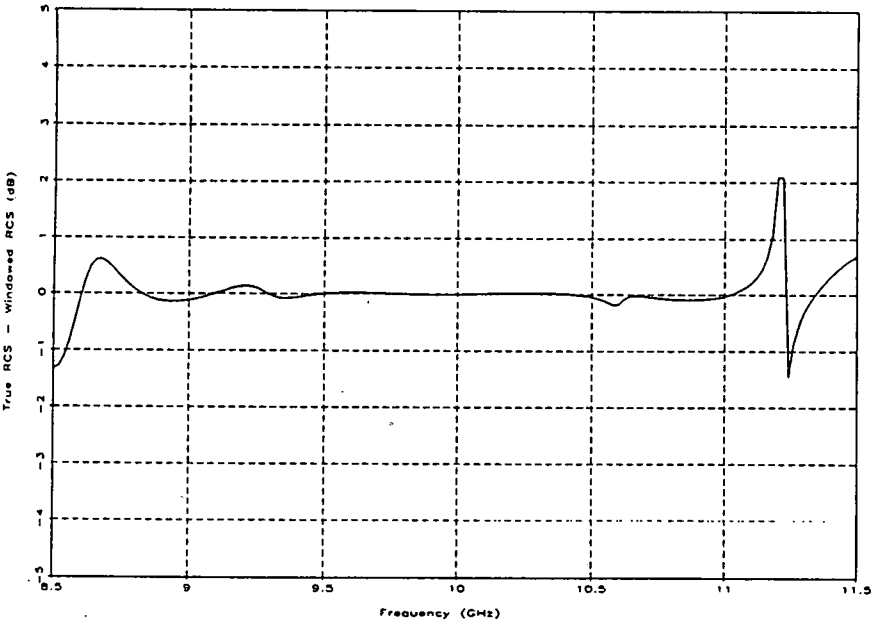

Figure A76

Three Wires Resonant Near 10 GHz without Noise
Blackman-Harris Weighting Edit Gate = 12/B

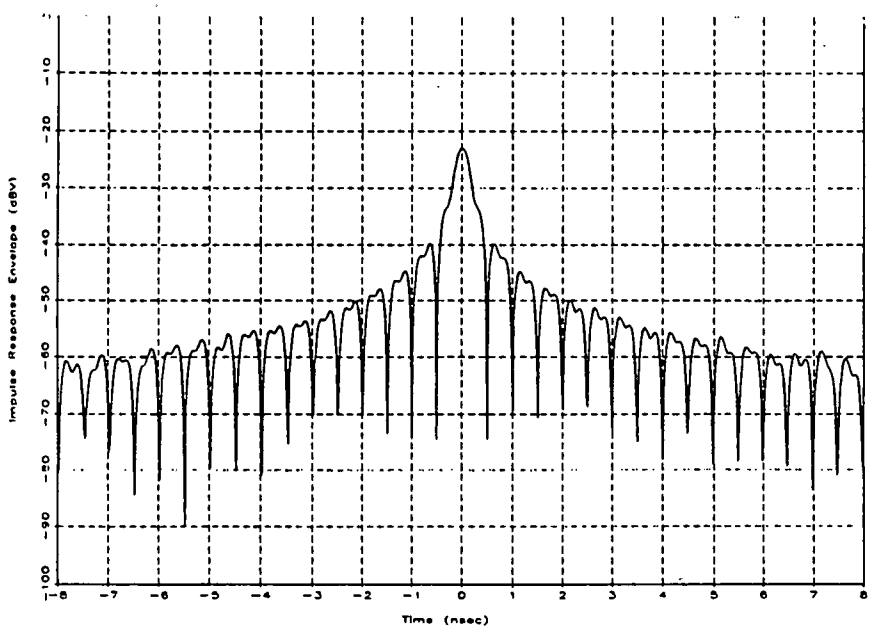

Figure A77

10 dB Ideal Step Source with -30 dBsm Noise
Uniform Weighting

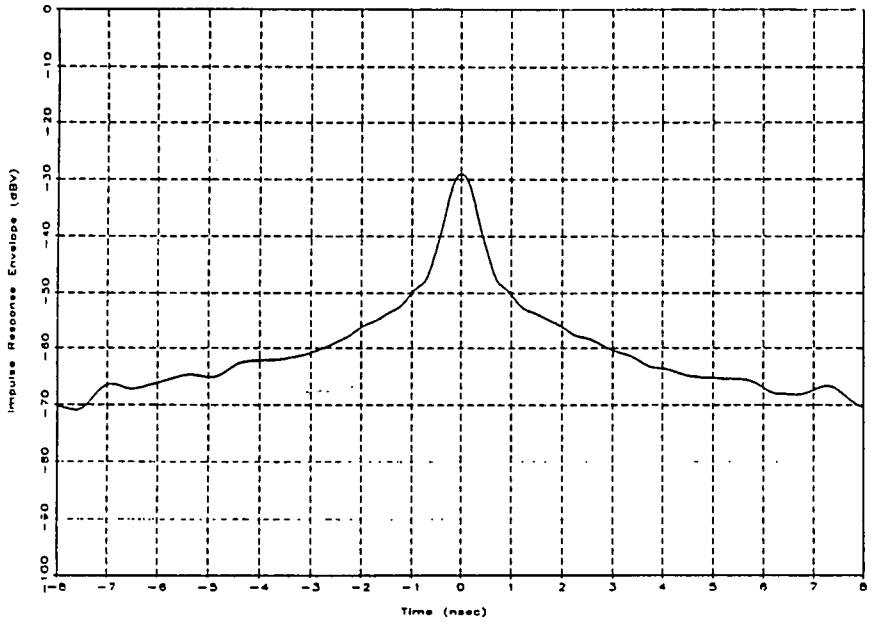

Figure A78

10 dB Ideal Step Source with -30 dBsm Noise
Hann Weighting

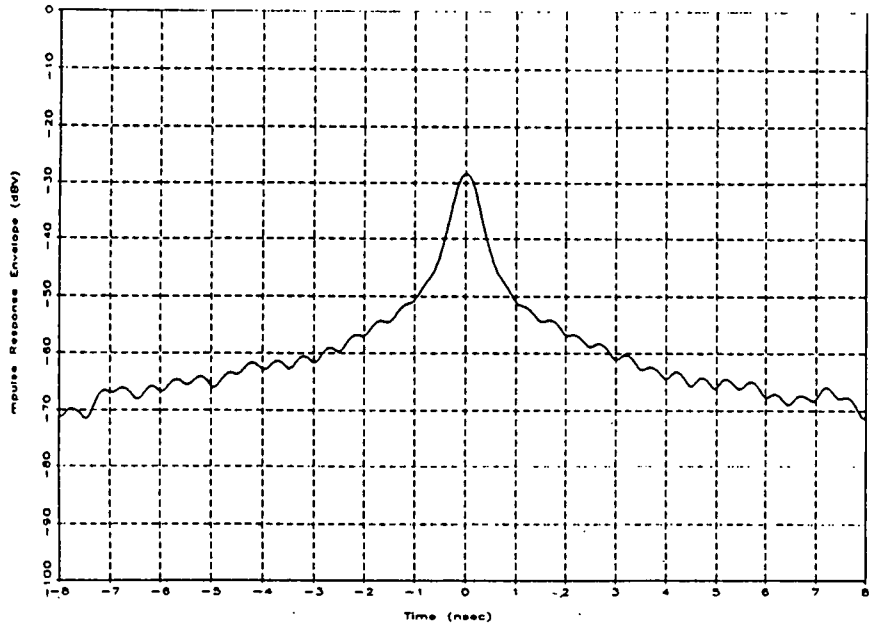

Figure A79

10 dB Ideal Step Source with -30 dBsm Noise
Hamming Weighting

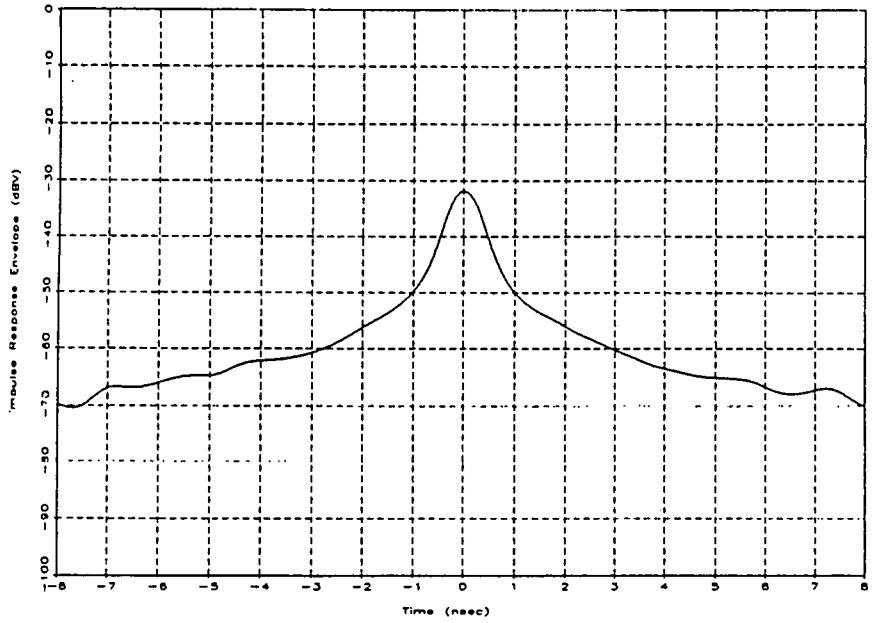

Figure A80

10 dB Ideal Step Source with -30 dBsm Noise
Blackman-Harris Weighting

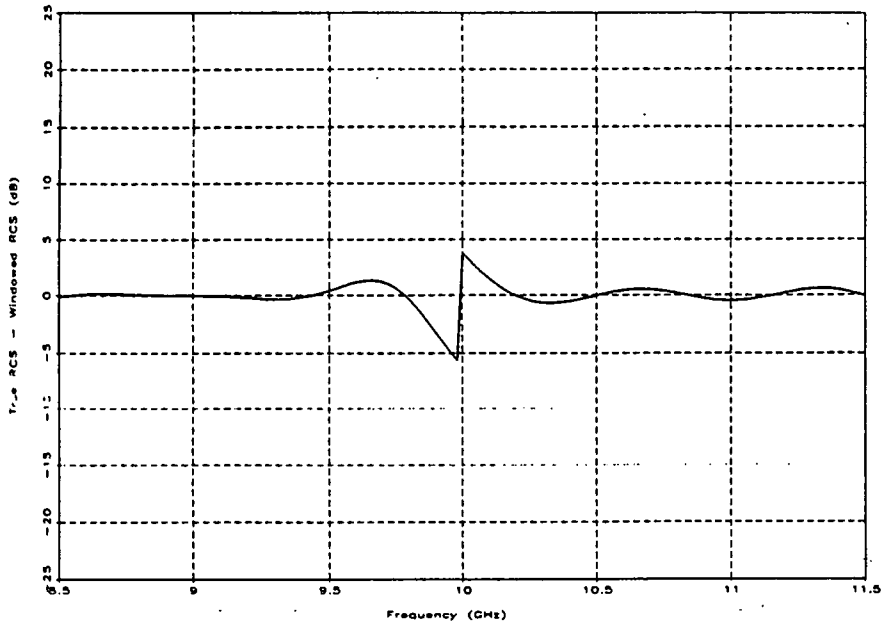

Figure A81

10 dB Ideal Step Source with -30 dBsm Noise
Uniform Weighting Edit Gate = 12/B

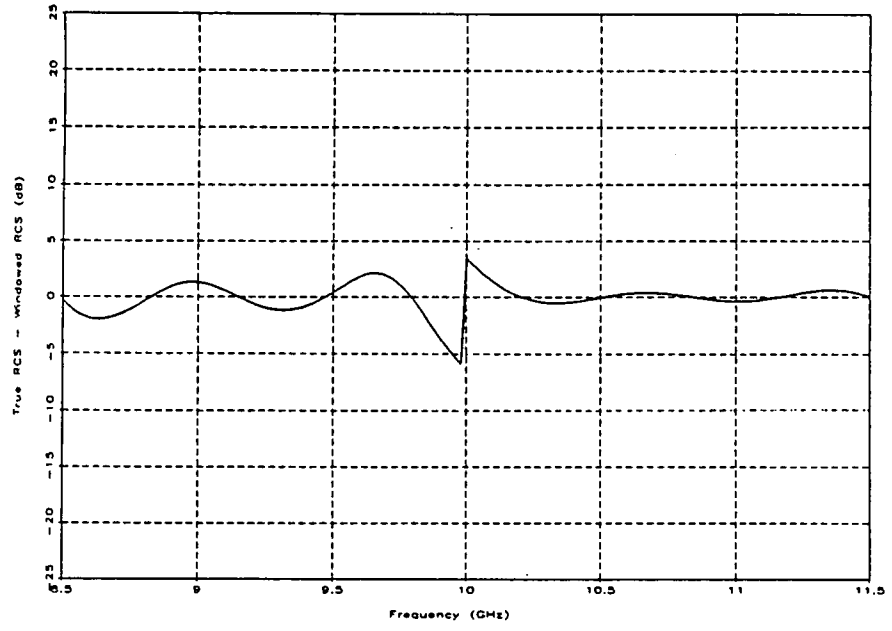

Figure A82

10 dB Ideal Step Source with -30 dBsm Noise
Hann Weighting Edit Gate = 12/B

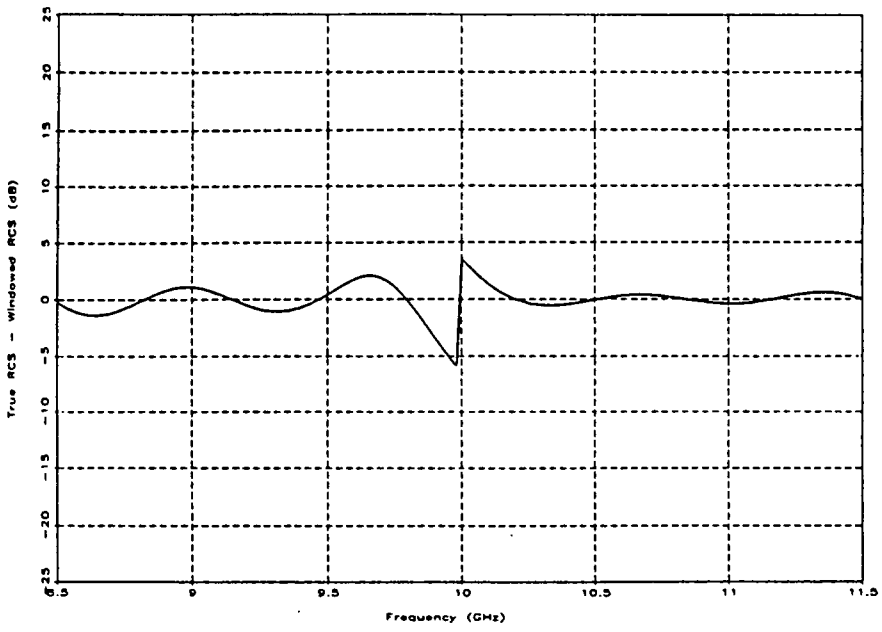

Figure A83

10 dB Ideal Step Source with -30 dBsm Noise
Hamming Weighting Edit Gate = 12/B

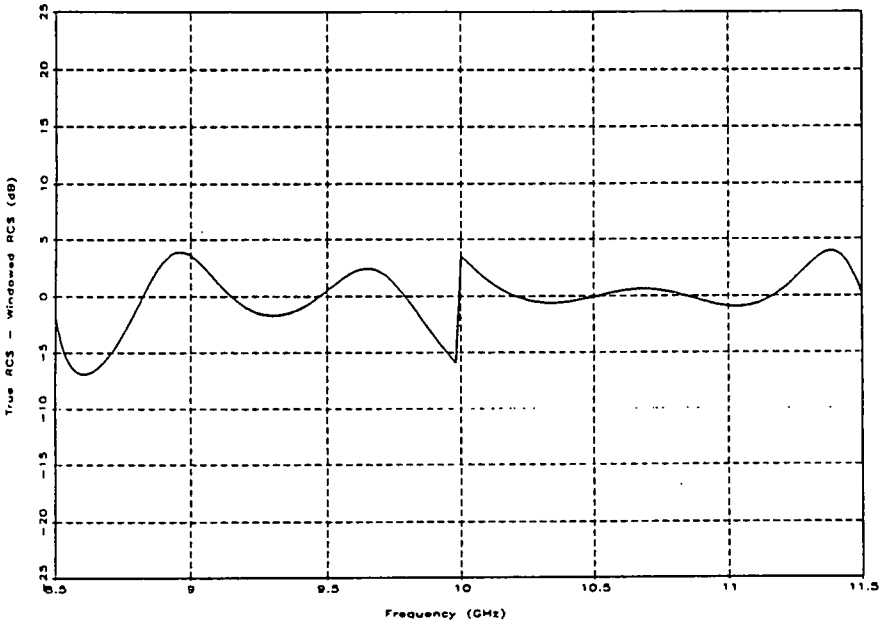

Figure A84

10 dB Ideal Step Source with -30 dBsm Noise
Blackman-Harris Weighting Edit Gate = 12/B

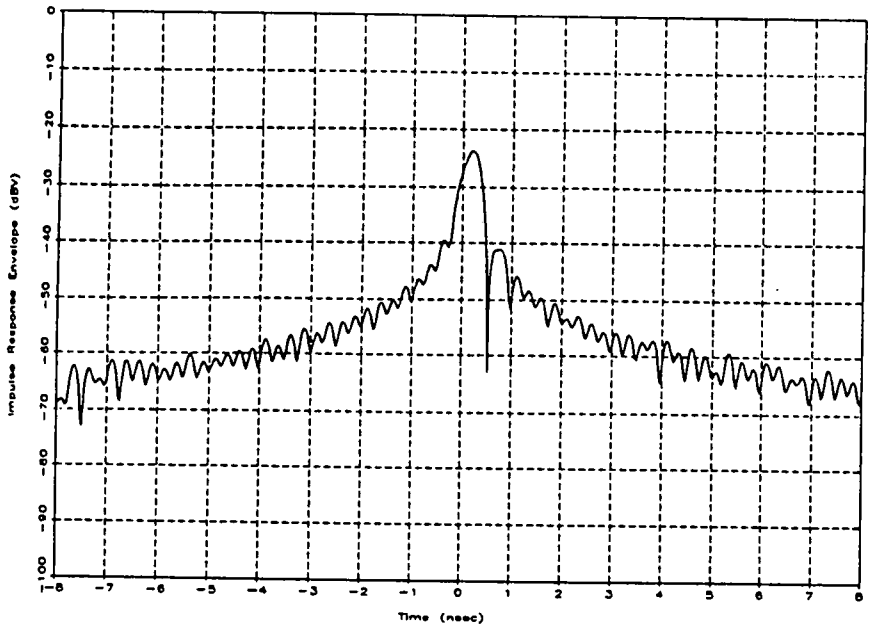

Figure A85

FSS Step Source with -30 dBsm Noise
Uniform Weighting

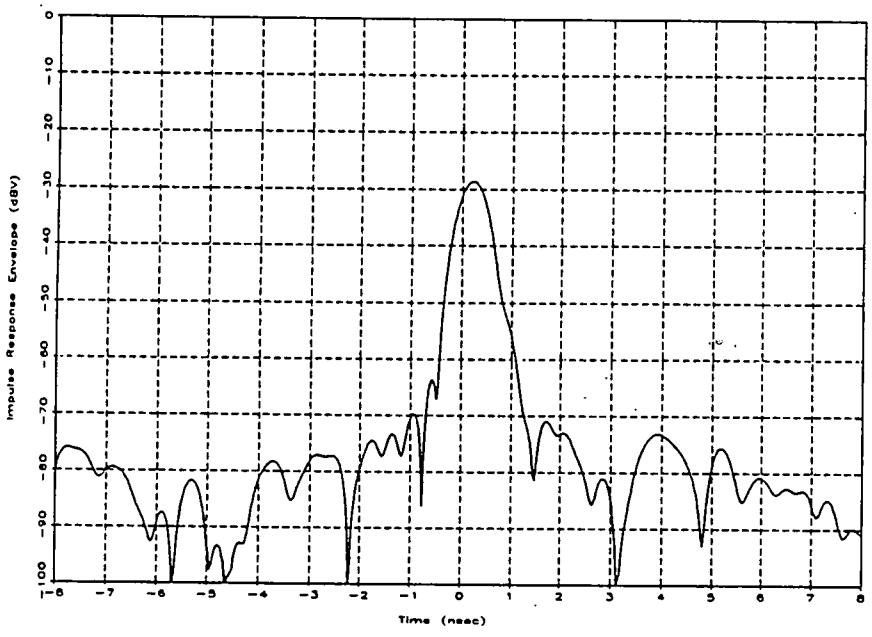

Figure A86

FSS Step Source with -30 dBsm Noise
Hann Weighting

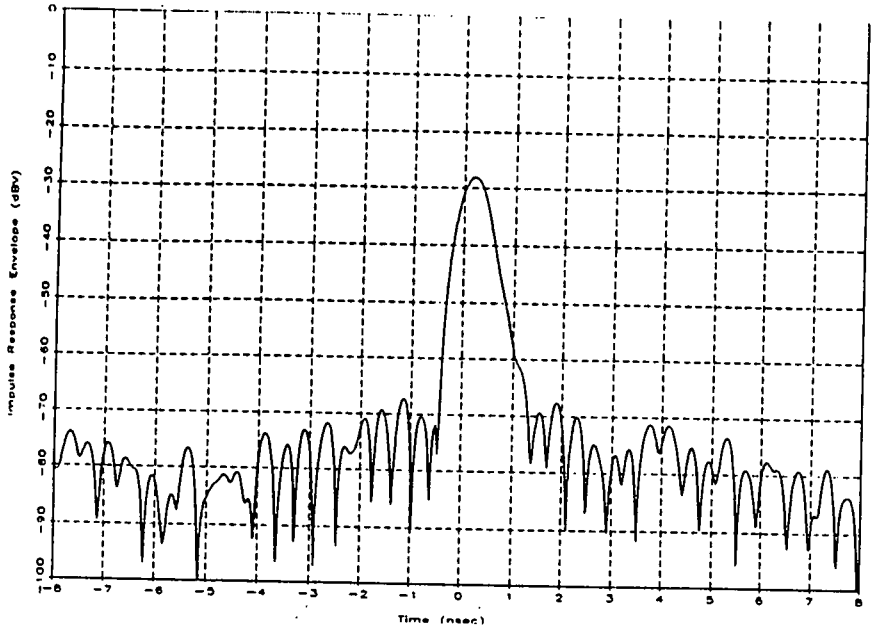

Figure A87

FSS Step Source with -30 dBsm Noise
Hamming Weighting

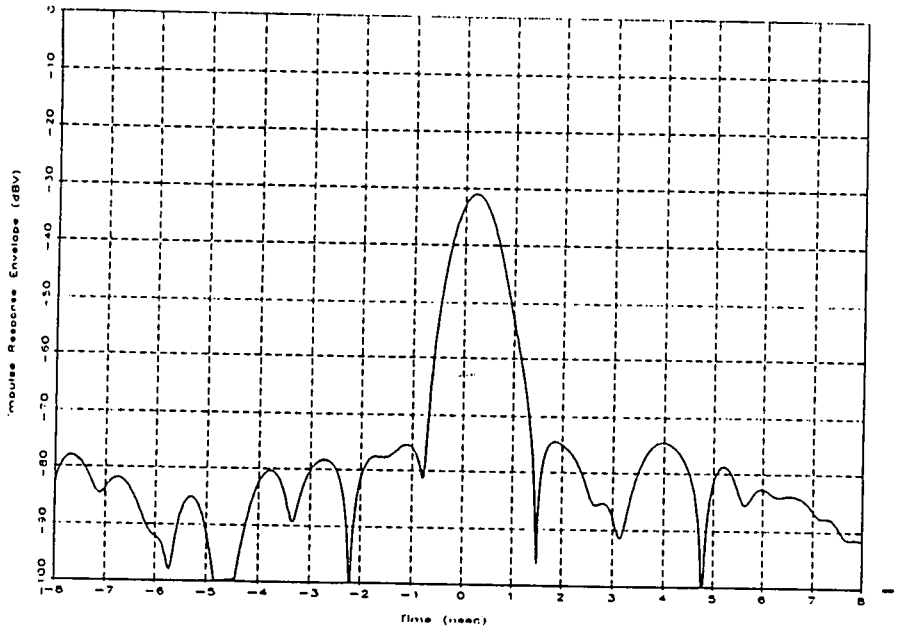

Figure A88

FSS Step Source with -30 dBsm Noise
Blackman-Harris Weighting

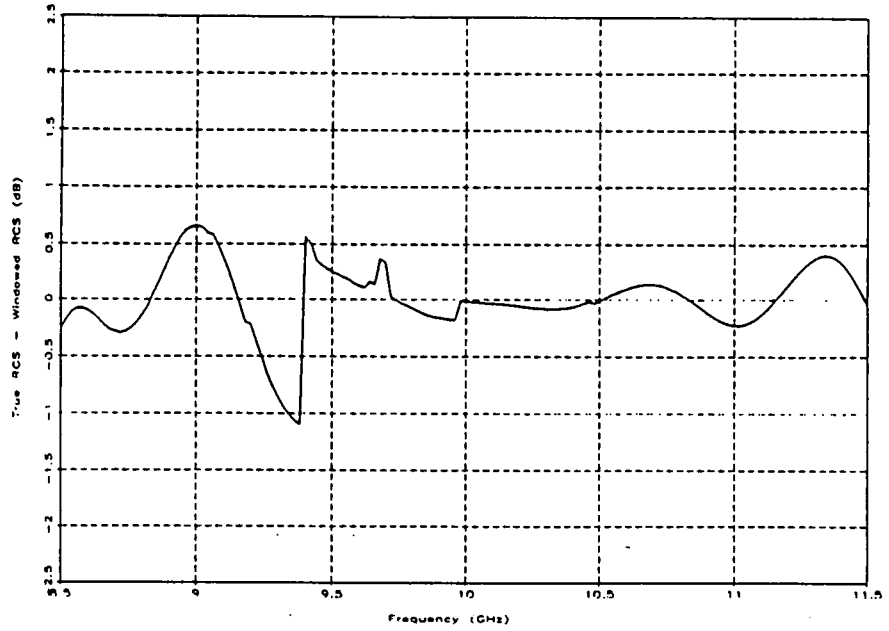

Figure A89

FSS Step Source with -30 dBsm Noise
Uniform Weighting Edit Gate = 12/B

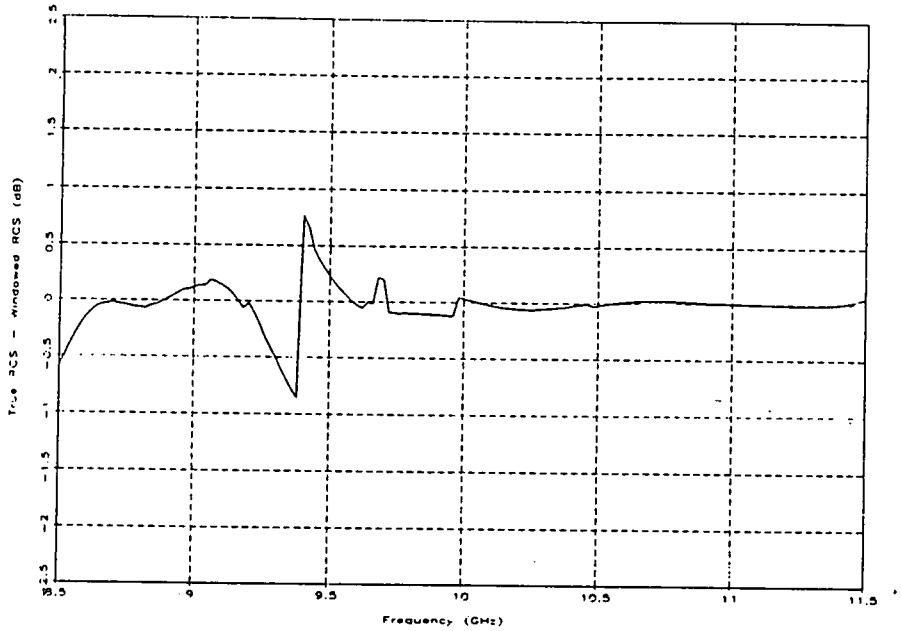

Figure A90

FSS Step Source with -30 dBsm Noise
Hann Weighting Edit Gate = 12/B

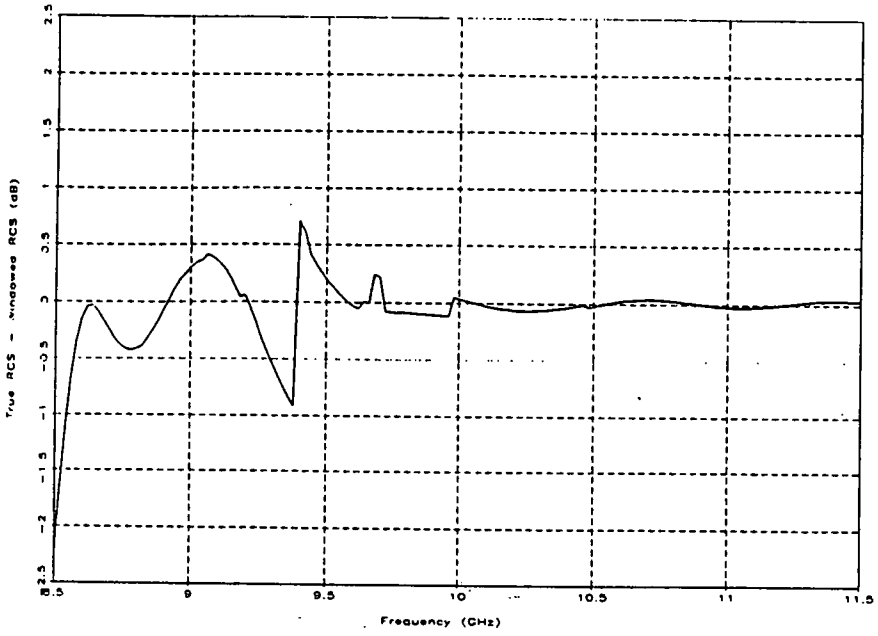

Figure A91

FSS Step Source with -30 dBsm Noise
Hamming Weighting Edit Gate = 12/B

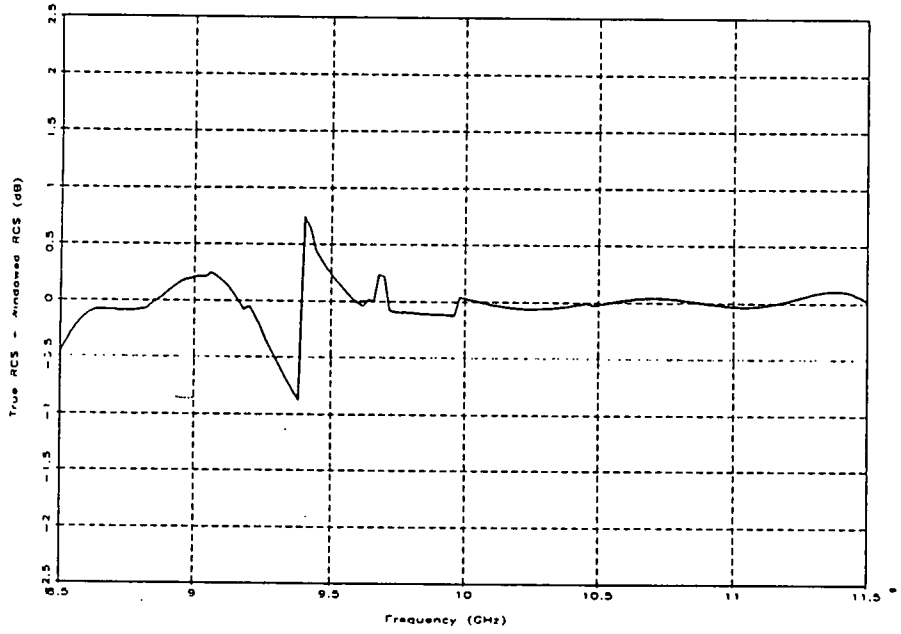

Figure A92

FSS Step Source with -30 dBsm Noise
Blackman-Harris Weighting Edit Gate = 12/B

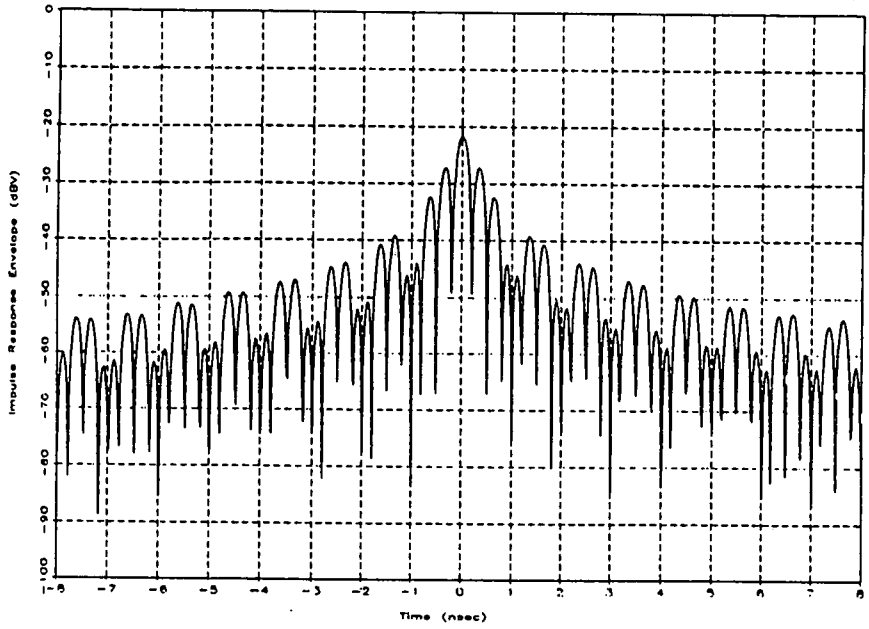

Figure A93

-10 dB Ideal Dip Source with -30 dBsm Noise
Uniform Weighting

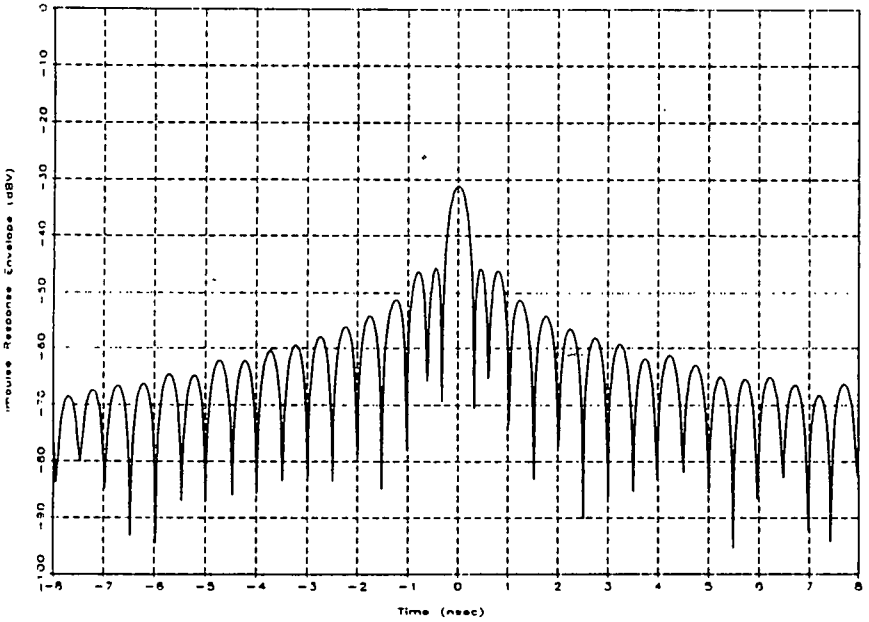

Figure A94

-10 dB Ideal Dip Source with -30 dBsm Noise
Hann Weighting

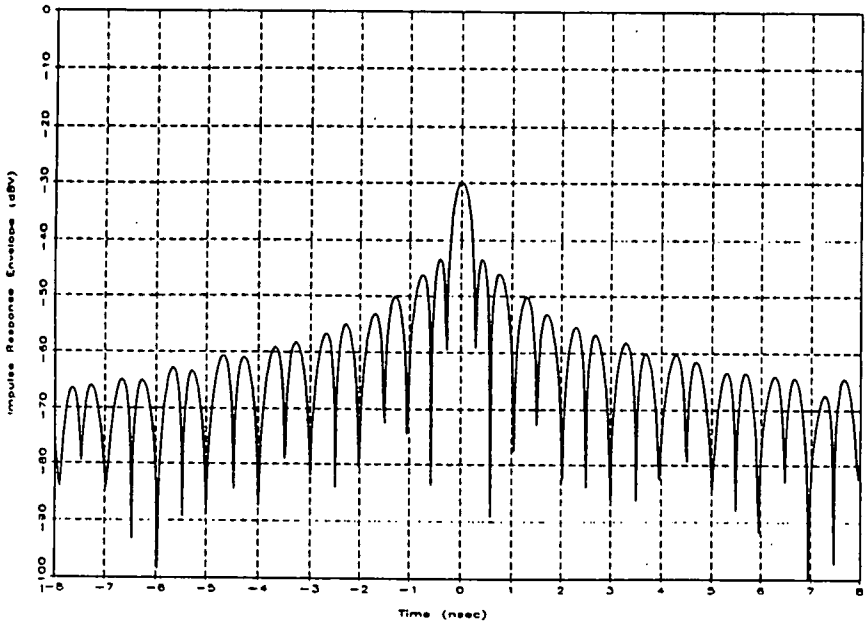

Figure A95

-10 dB Ideal Dip Source with -30 dBsm Noise
Hamming Weighting

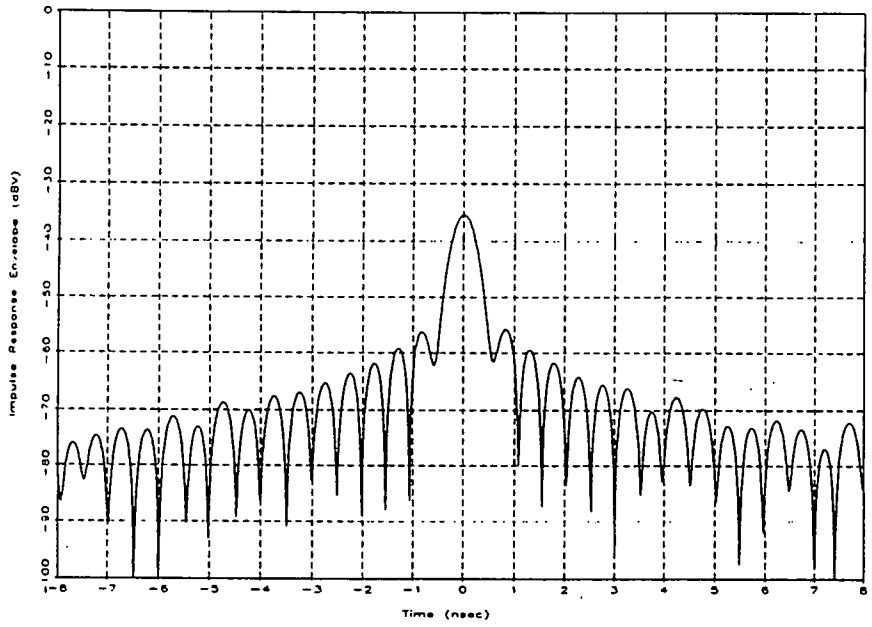

Figure A96

-10 dB Ideal Dip Source with -30 dBsm Noise
Blackman-Harris Weighting

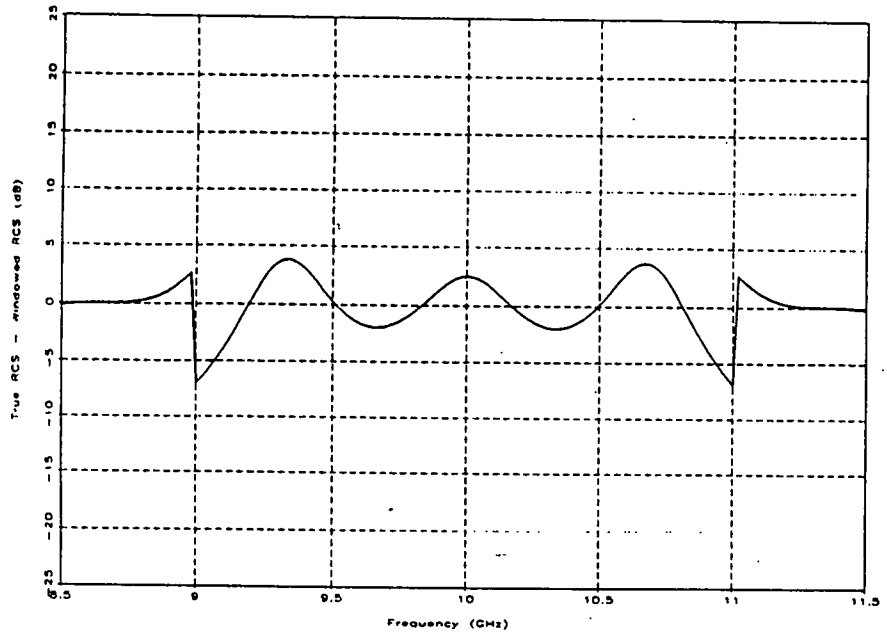

Figure A97

-10 dB Ideal Dip Source with -30 dBsm Noise
Uniform Weighting Edit Gate = 12/B

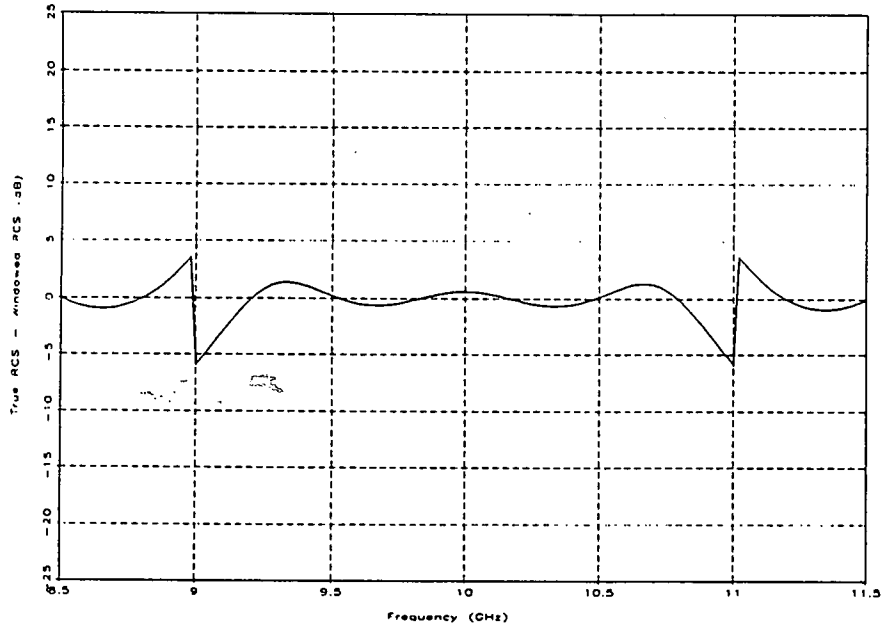

Figure A98

-10 dB Ideal Dip Source with -30 dBsm Noise
Hann Weighting Edit Gate = 12/B

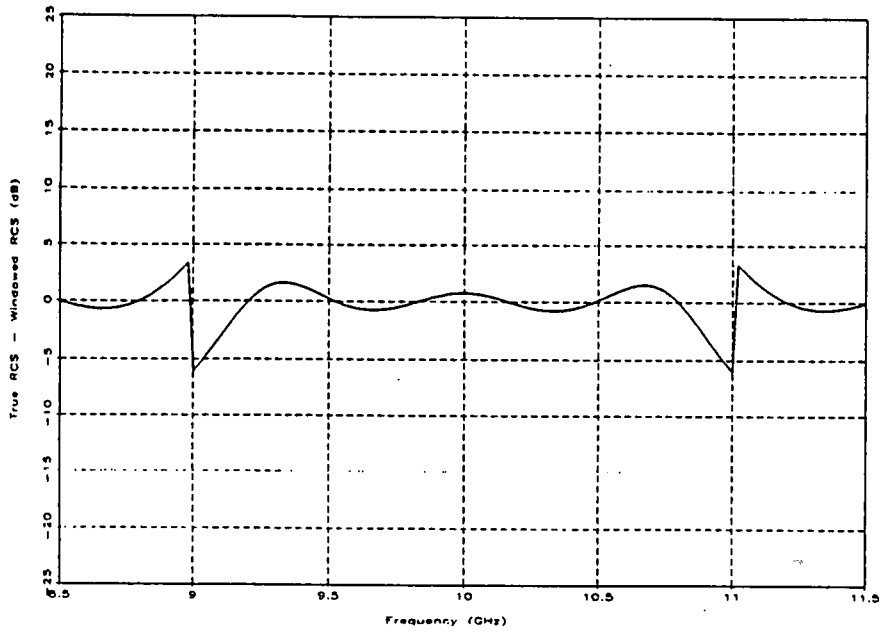

Figure A99

-10 dB Ideal Dip Source with -30 dBsm Noise
Hamming Weighting Edit Gate = 12/B

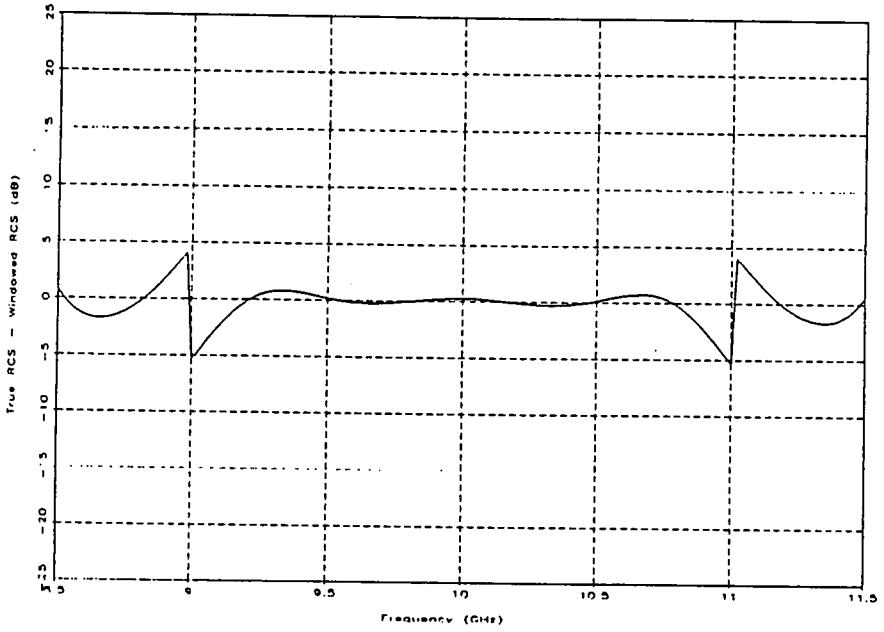

Figure A100

-10 dB Ideal Dip Source with -30 dBsm Noise
Blackman-Harris Weighting Edit Gate = 12/B

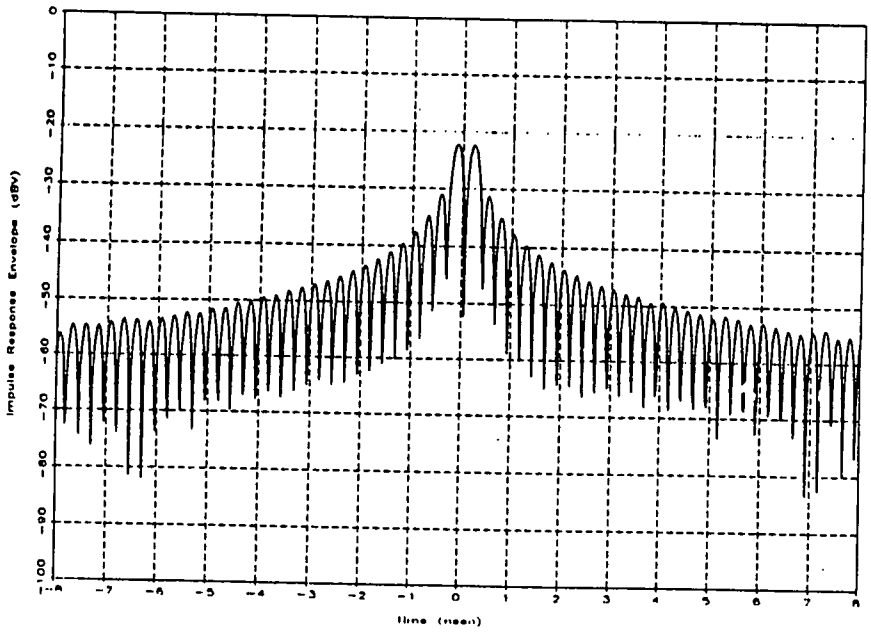

Figure A101

FSS Dip Source with -30 dBsm Noise
Uniform Weighting

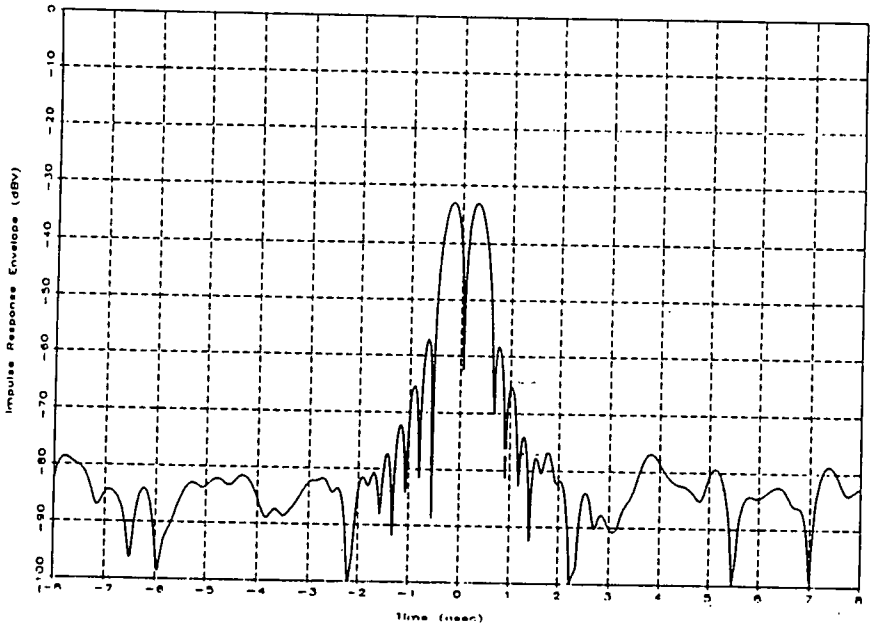

Figure A102

FSS Dip Source with -30 dBsm Noise
Hann Weighting

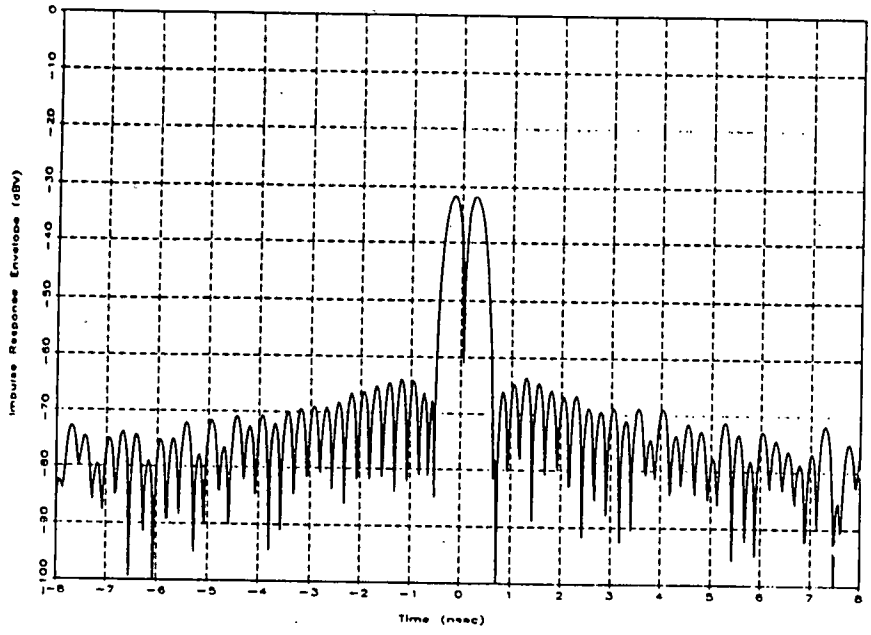

Figure A103

FSS Dip Source with -30 dBsm Noise
Hamming Weighting

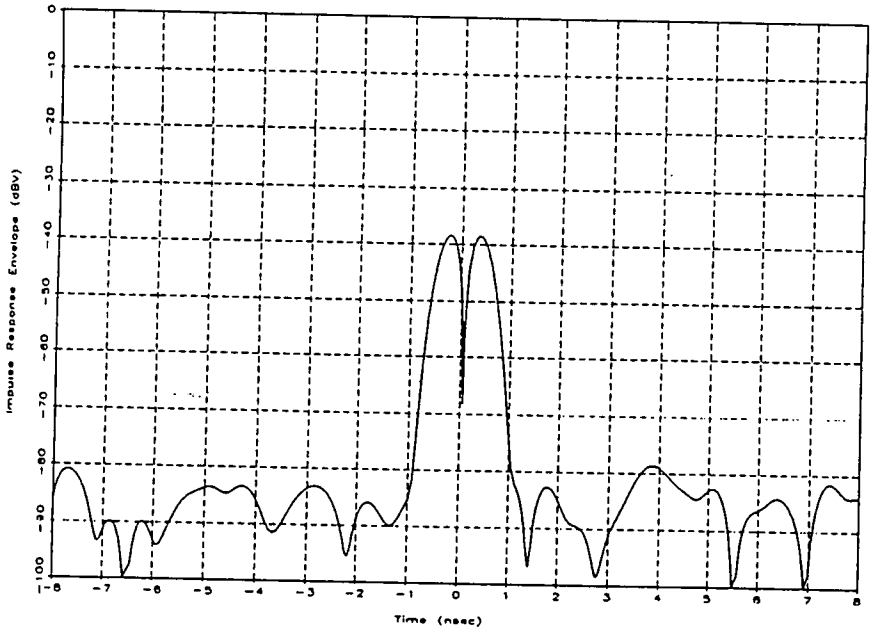

Figure A104

FSS Dip Source with -30 dBsm Noise
Blackman-Harris Weighting

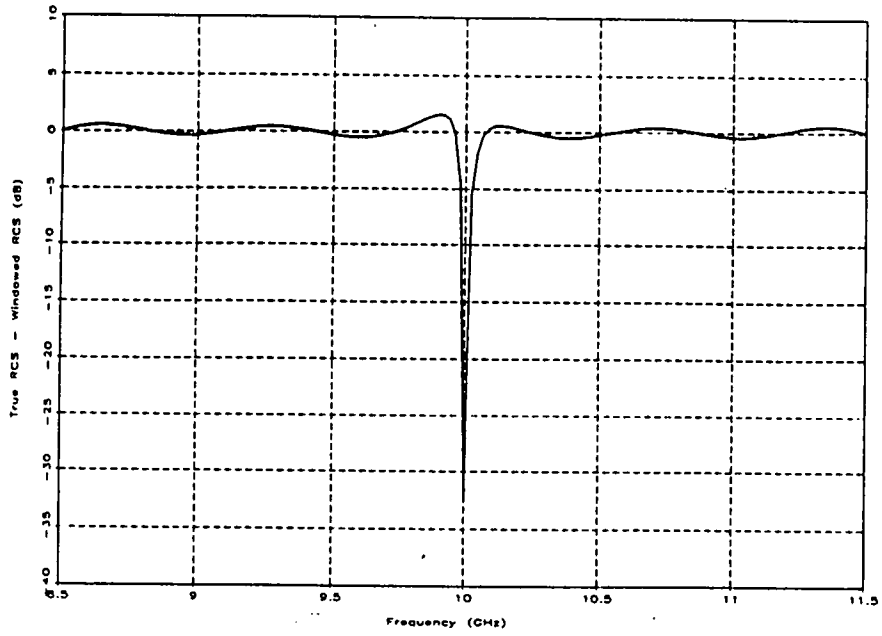

Figure A105

FSS Dip Source with -30 dBsm Noise
Uniform Weighting Edit Gate = 12/B

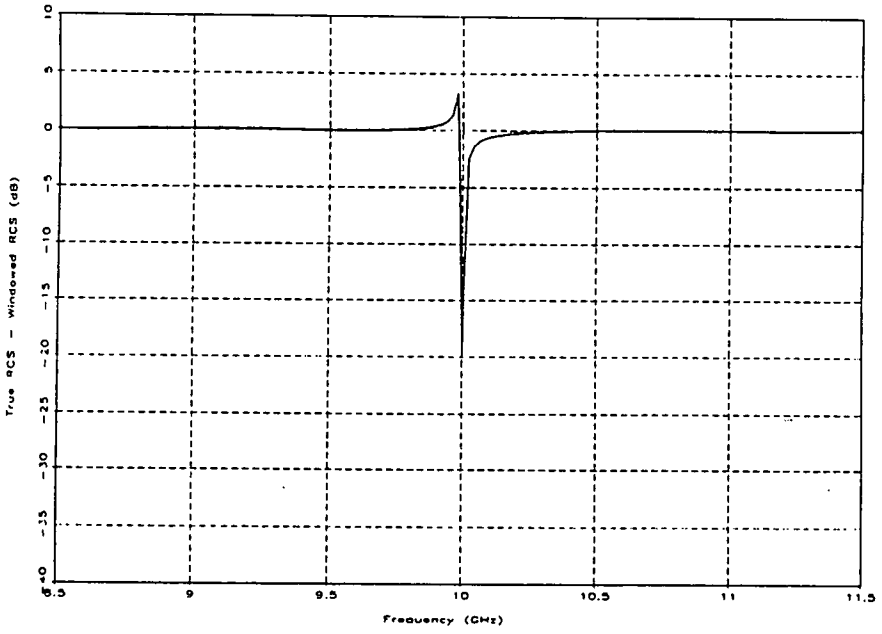

Figure A106

FSS Dip Source with -30 dBsm Noise
Hann Weighting Edit Gate = 12/B

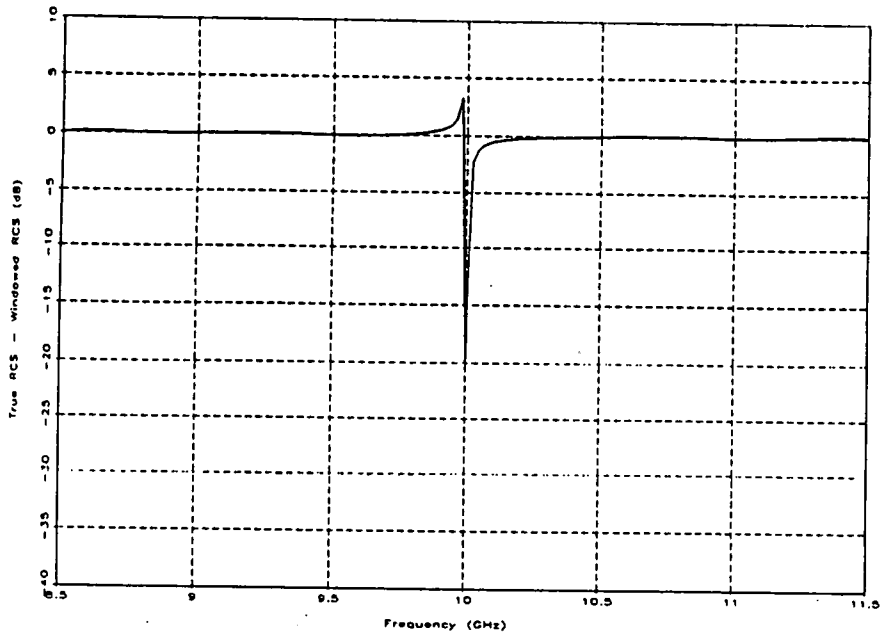

Figure A107

FSS Dip Source with -30 dBsm Noise
Hamming Weighting Edit Gate = 12/B

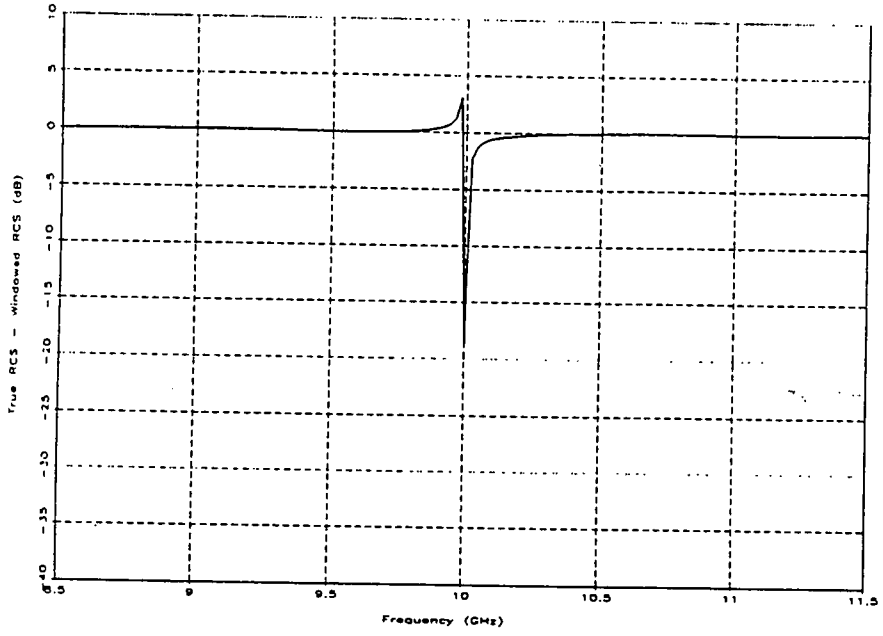

Figure A108

FSS Dip Source with -30 dBsm Noise
Blackman-Harris Weighting Edit Gate = 12/B

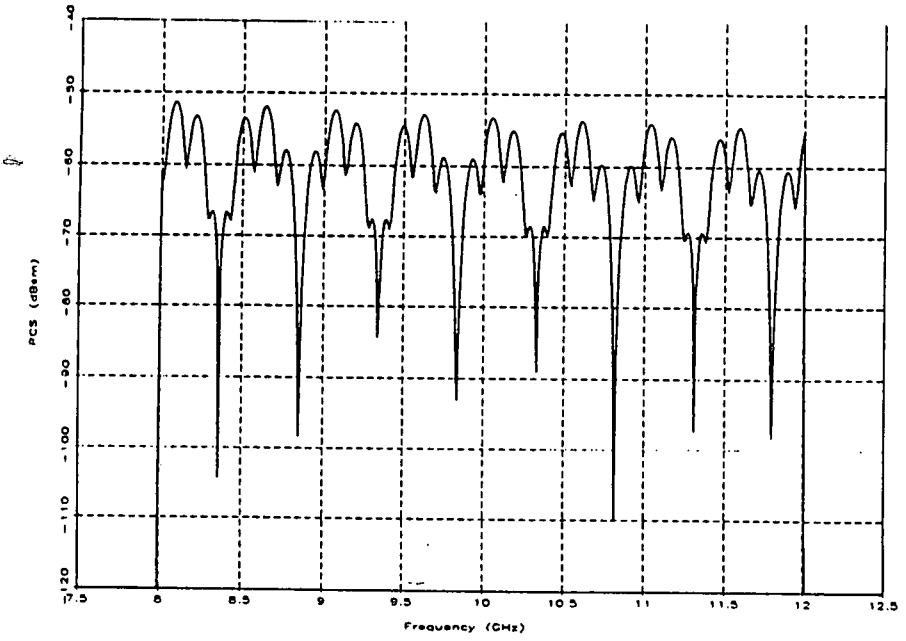

Figure A109
Test Fixture Before Normalization

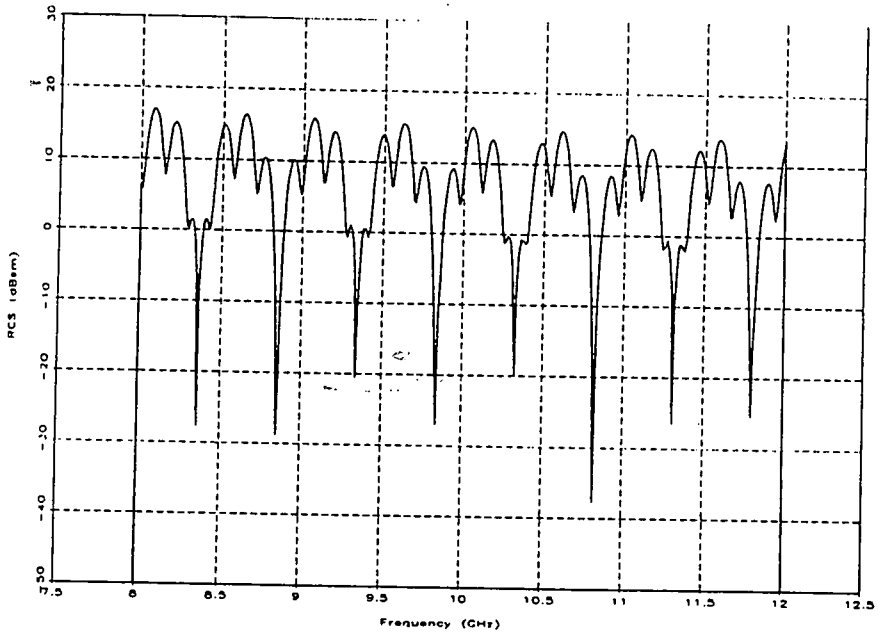

Figure A110
Test Fixture with -30 dBsm Noise

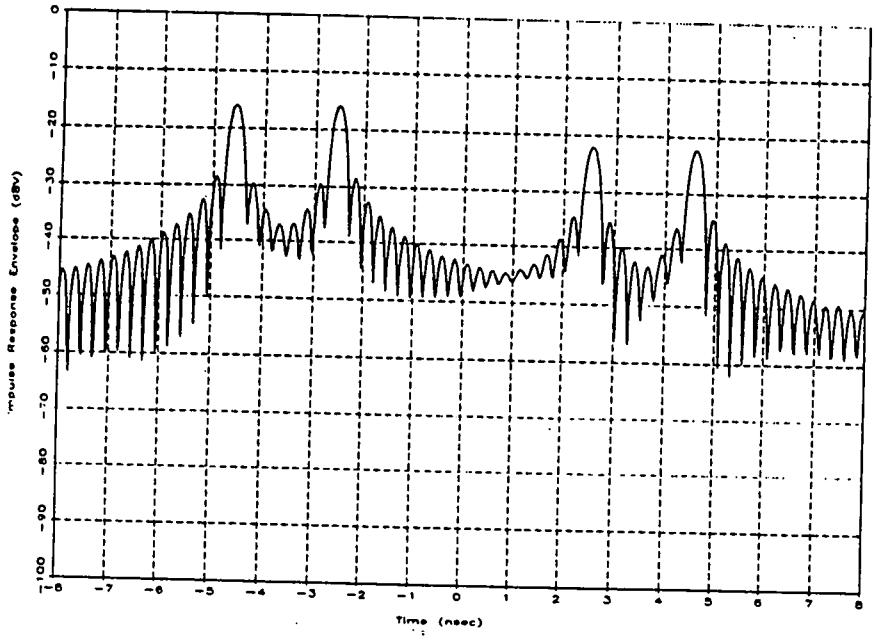

Figure A111

Test Fixture with -30 dBsm Noise
Uniform Weighting

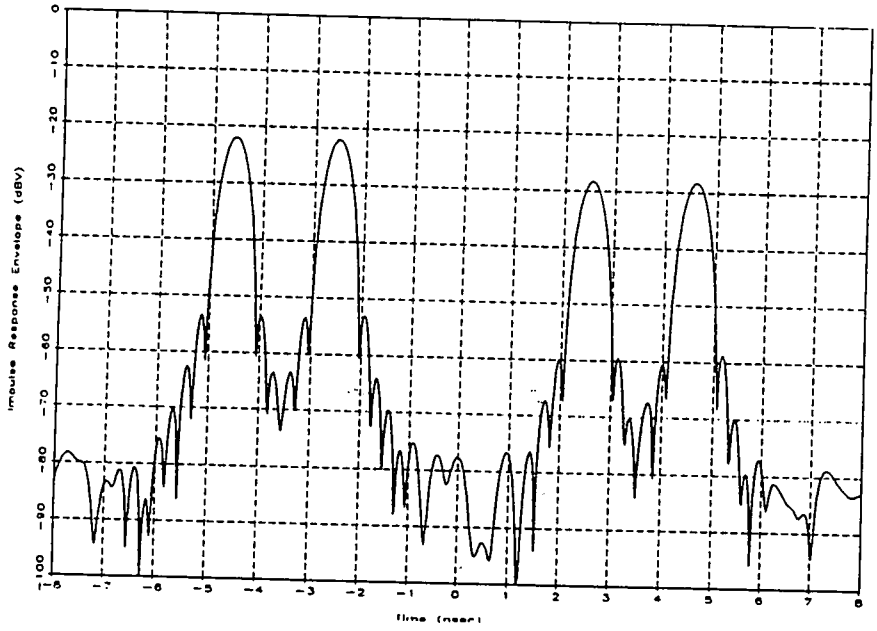

Figure A112

Test Fixture with -30 dBsm Noise
Hann Weighting

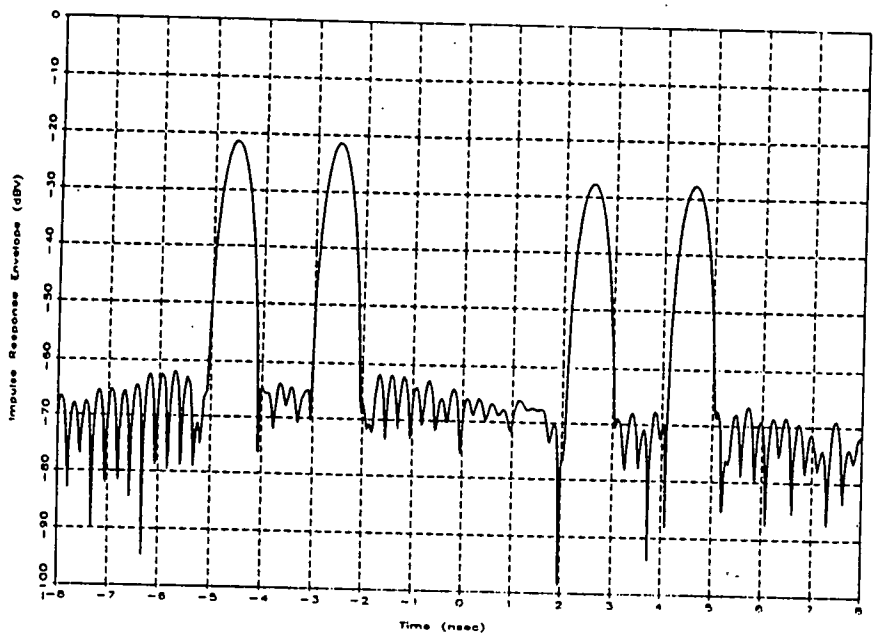

Figure A113

Test Fixture with -30 dBsm Noise
Hamming Weighting

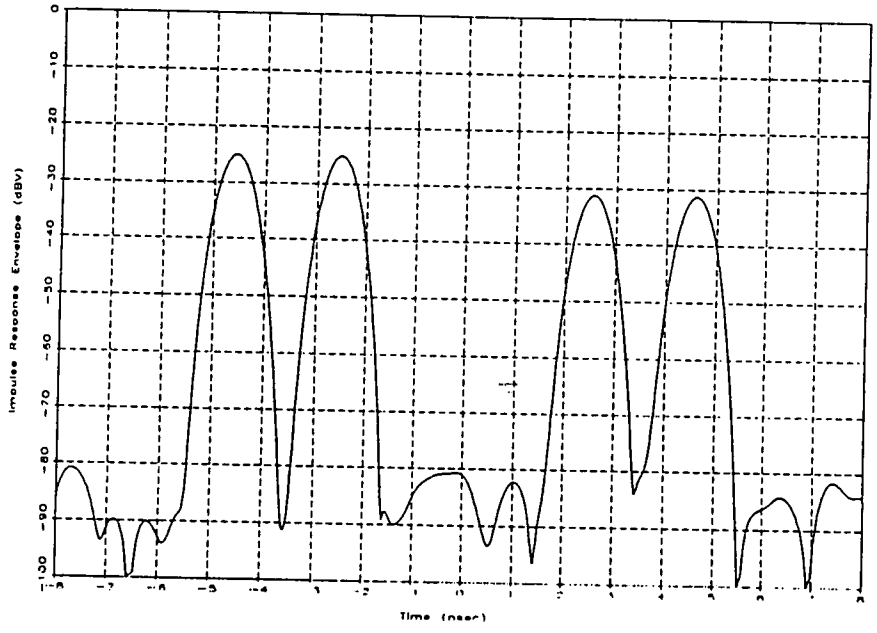

Figure A114

Test Fixture with -30 dBsm Noise
Blackman-Harris Weighting

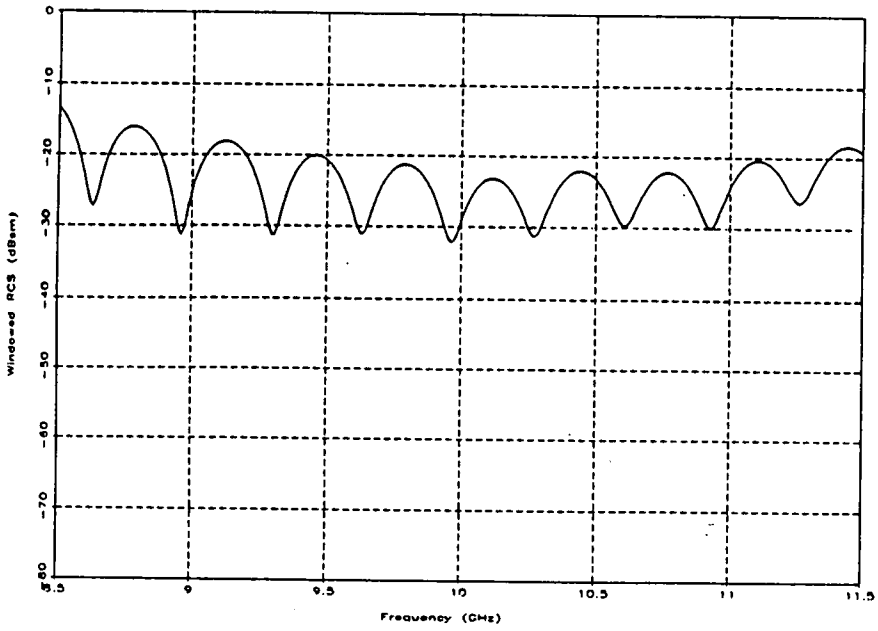

Figure A115

Test Fixture with -30 dBsm Noise
Uniform Weighting Edit Gate = 12/B

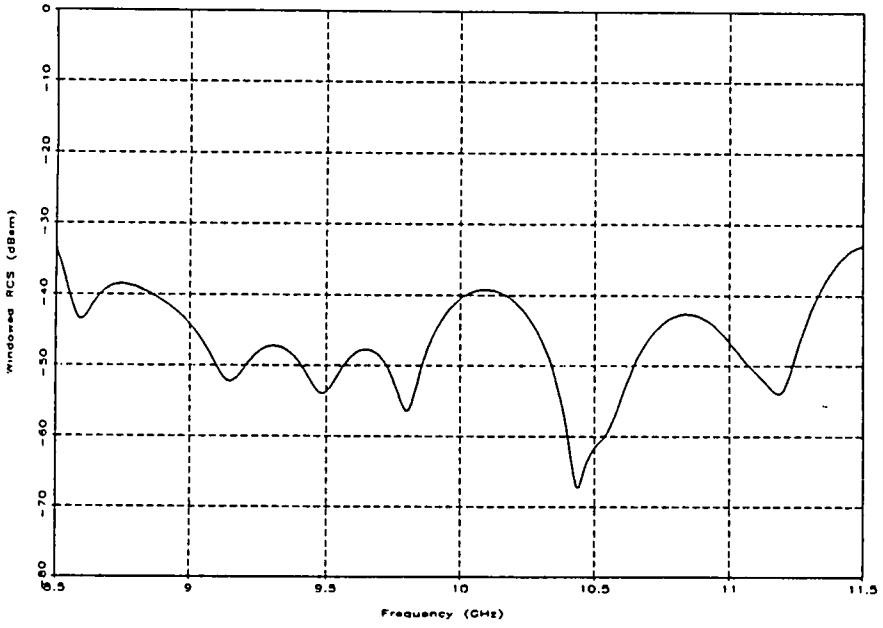

Figure A116

Test Fixture with -30 dBsm Noise
Hann Weighting Edit Gate = 12/B

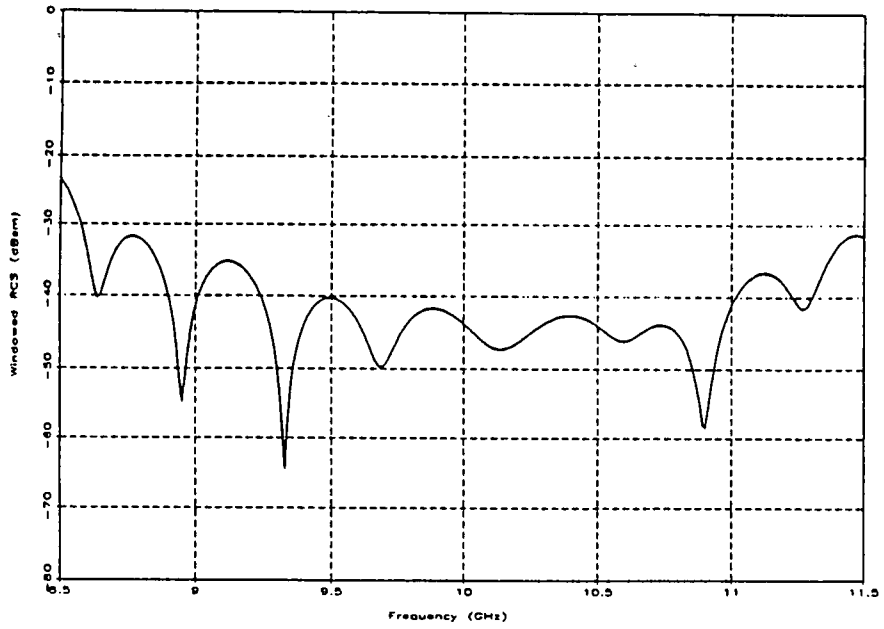

Figure A117

Test Fixture with -30 dBsm Noise
Hamming Weighting Edit Gate = 12/B

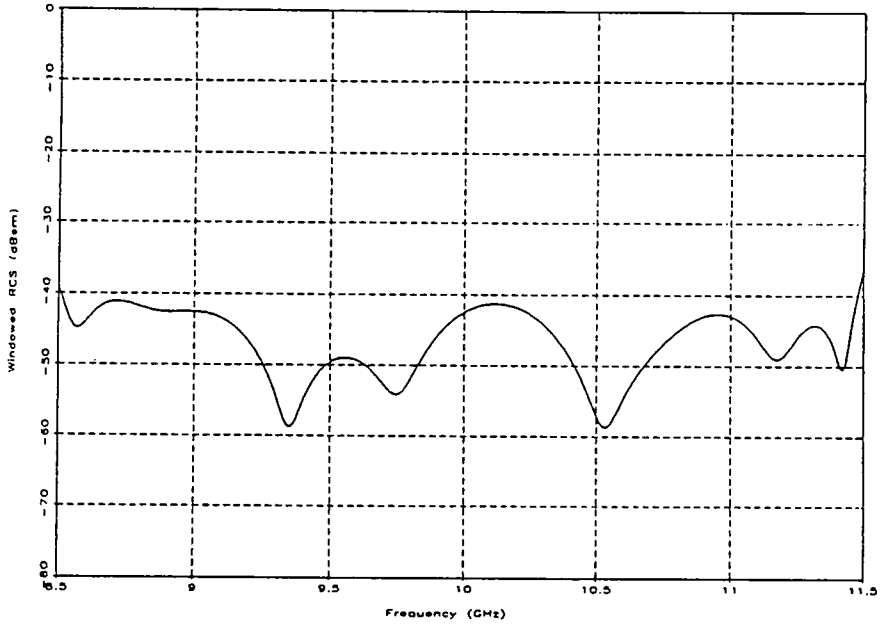

Figure A118

Test Fixture with -30 dBsm Noise
Blackman-Harris Weighting Edit Gate = 12/B

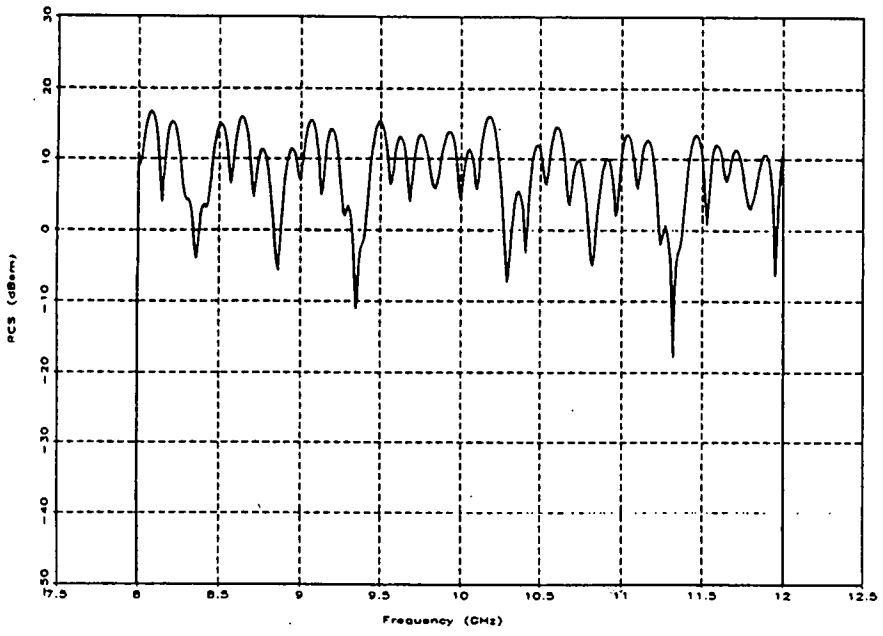

Figure A119

Three Wire Source Plus Test Fixture with -30 dBsm Noise

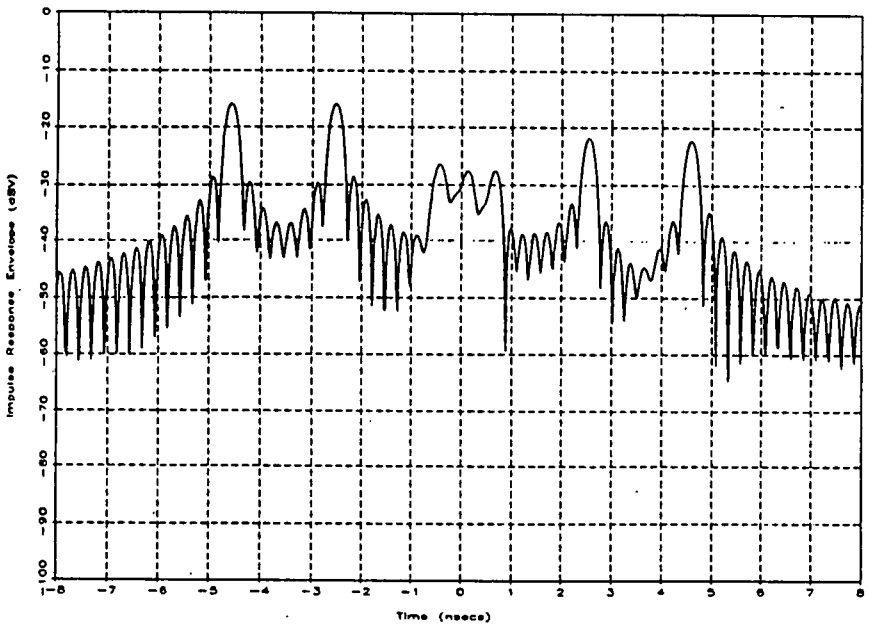

Figure A120

Three Wire Source Plus Test Fixture with -30 dBsm Noise
Uniform Weighting

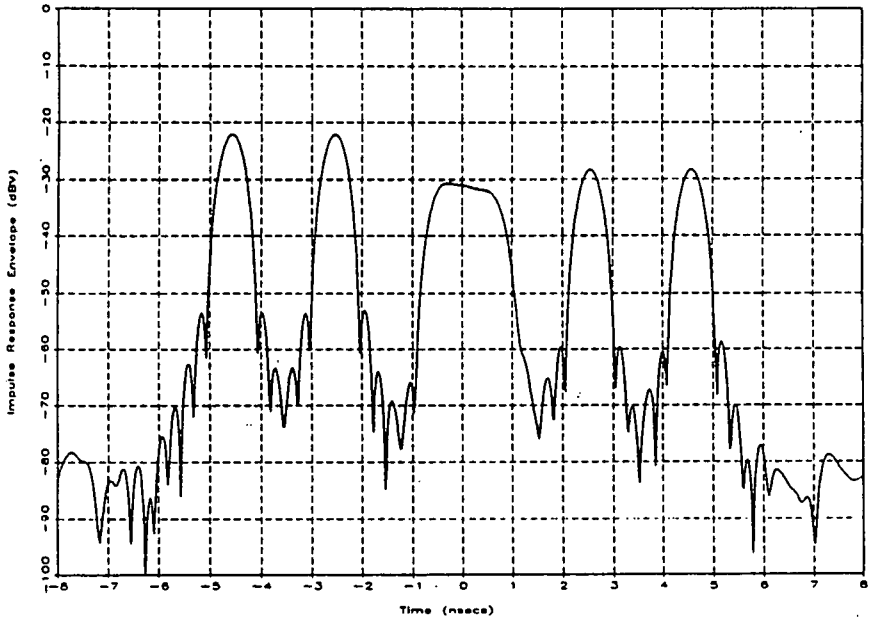

Figure A121

Three Wire Source Plus Test Fixture with -30 dBsm Noise
Hann Weighting

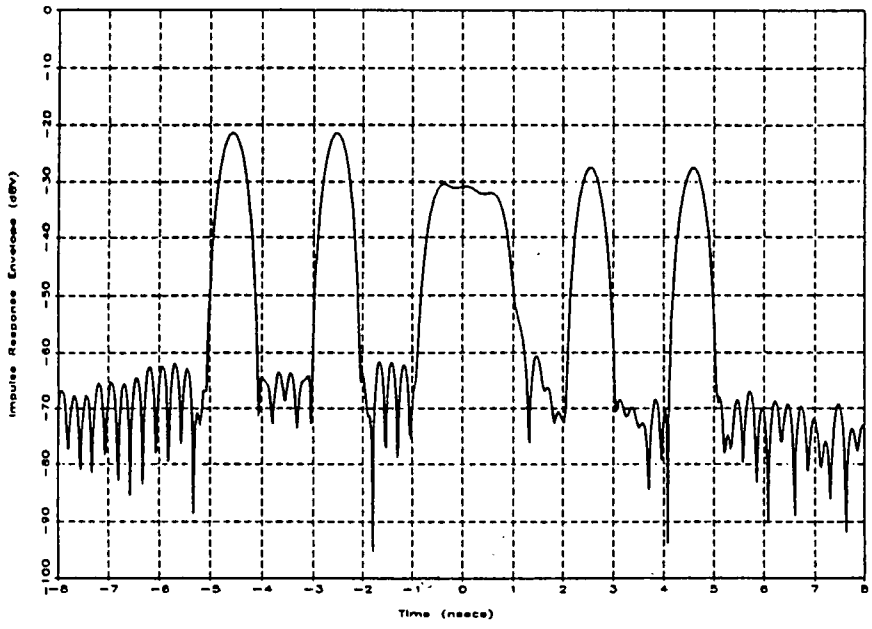

Figure A122

Three Wire Source Plus Test Fixture with -30 dBsm Noise
Hamming Weighting

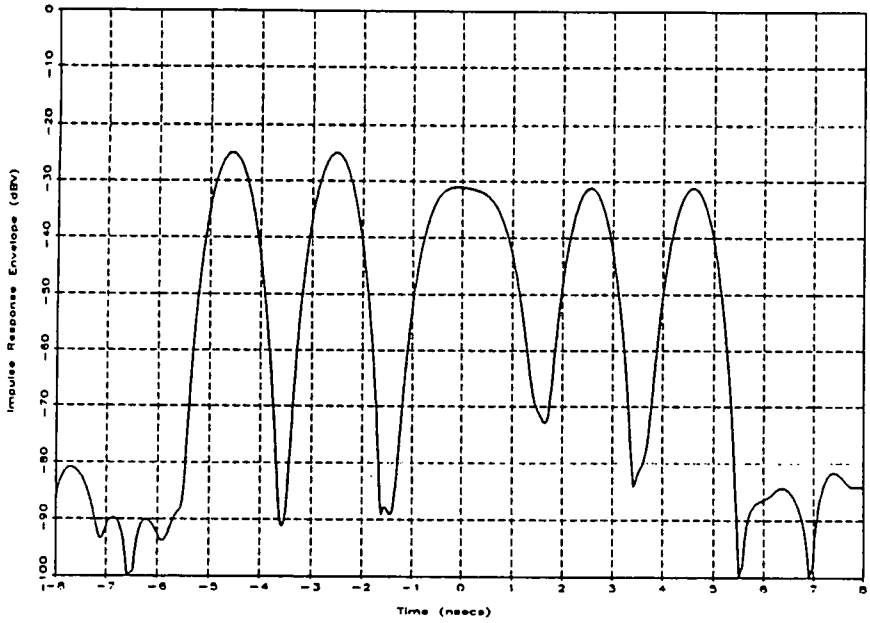

Figure A123

Three Wire Source Plus Test Fixture with -30 dBsm Noise
Blackman-Harris Weighting

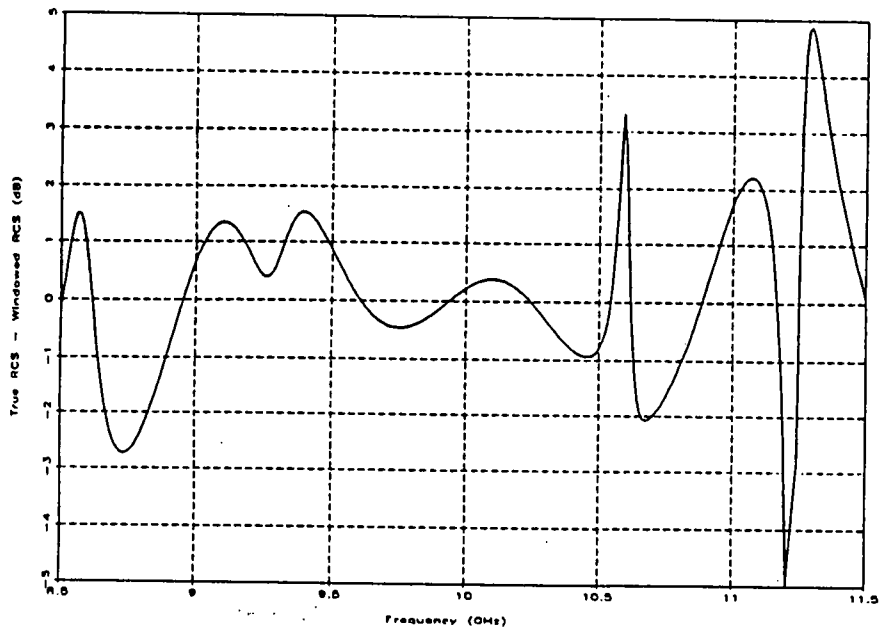

Figure A124

Three Wire Source Plus Test Fixture with -30 dBsm Noise
Uniform Weighting Edit Gate = 12/B

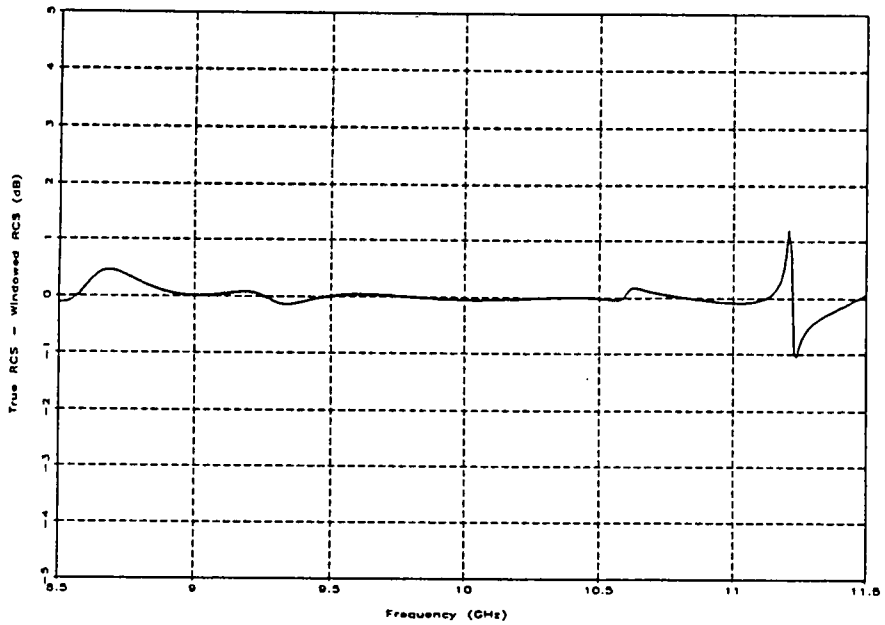

Figure A125

Three Wire Source Plus Test Fixture with -30 dBsm Noise
Hann Weighting Edit Gate = 12/B

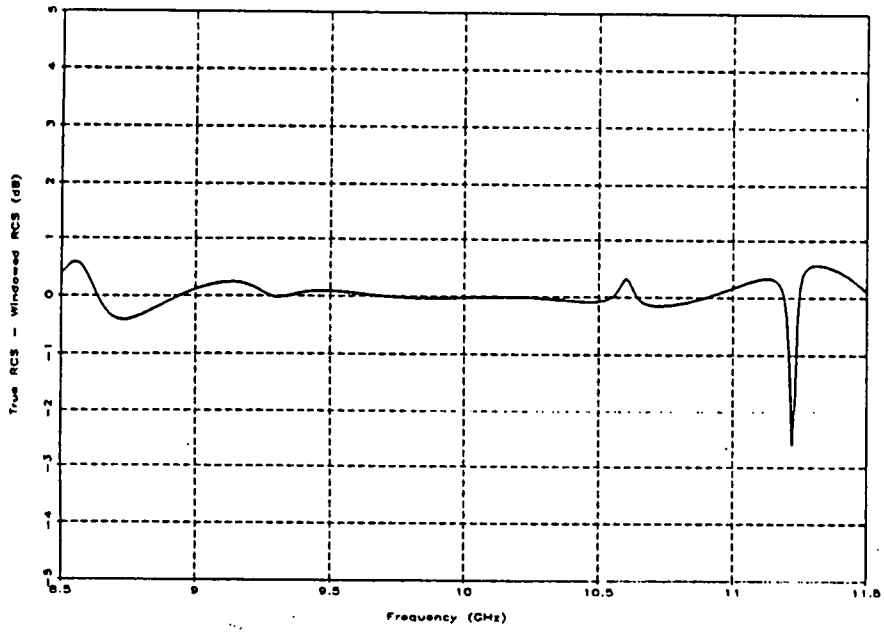

Figure A126

Three Wire Source Plus Test Fixture with -30 dBsm Noise
Hamming Weighting Edit Gate = 12/B

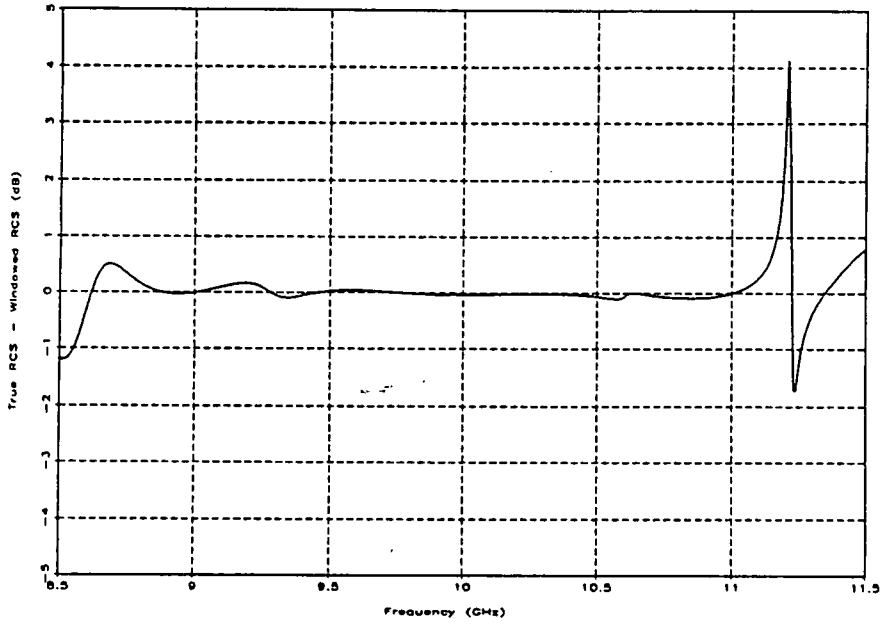

Figure A127

Three Wire Source Plus Test Fixture with -30 dBsm Noise
Blackman-Harris Weighting Edit Gate = 12/B

APPENDIX B

LISTINGS OF INPUT FILES

Included in the following figures are listings of the input files referenced in chapter 3 of the main body for the codes NEC-MOM, PMM, and RCSBSC for the wire sources, FSS sources, and test fixture, respectively

```
CM  NEC-MOM Input File for the Short Wire Source
CM
CM  One Wire  Positioned at 0  Resonant near 10 GHz
CE
GW  1    9         0         0    -.0067         0         0     .0067   .000167
GE  0
FR  0  401    0    0     8000.       10.
EX  1    1    1    0       90        0         0         0         0         0
PT -1
RP  0    1    1 1000       90        0         0         0
EN
```

Figure B1

NEC-MOM Input File for the Short Wire Source

```
CM  NEC-MOM Input File for the Long Wire Source
CM
CM  One Wire  Positioned at 0  Resonant near 500 MHz
CE
GW  1    9         0         0     -.134         0         0      .134   .000167
GE  0
FR  0  401    0    0     8000.       10.
EX  1    1    1    0       90        0         0         0         0         0
PT -1
RP  0    1    1 1000       90        0         0         0
EN
```

Figure B2

NEC-MOM Input File for the Long Wire Source

```
CM  NEC-MOM Input File for the Multi-Wire Source
CM
CM  Three Wires  Spaced .25 feet apart  All resonant near 10 GHz
CE
GW  1    9    -.0762         0    -.0062    -.0762         0     .0062   .000167
GW  1    9         0         0    -.0067         0         0     .0067   .000167
GW  1    9     .0762         0    -.0072     .0762         0     .0072   .000167
GE  0
FR  0  401    0    0     8000.       10.
EX  1    1    1    0       90        0         0         0         0         0
PT -1
RP  0    1    1 1000       90        0         0         0
EN
```

Figure B3

NEC-MOM Input File for the Multi-Wire Source

```
TITLE 'FSS STEP'
NOPLOTFILE
ANGLE 0.,0.01
FREQUENCY 8.,12.,.01
THICK = .59
DX = 1.
L = 0.63
DZ = L+1.2
WIDTH = L/10
DX2 = 1.
L2 = 0.68
DZ2 = L2+1.2
WIDTH2 = L2/10
X1 = 0.
SKEWED GRID DX,DZ=DZ
DIPOLE ARRAY WIDTH,0.0006
 NODE 1,X1,-L
 NODE 2,X1,-L/2
 NODE 3,X1,0
 NODE 4,X1,L/2
 NODE 5,X1,L
 SEGMENT 1,1,2
 SEGMENT 2,2,3
 SEGMENT 3,3,4
 SEGMENT 4,4,5
 MODE 2,1,2
 MODE 3,2,3
 MODE 4,3,4
END ARRAY
SLAB THICK,(1.,0.),(1.,0.)
SKEWED GRID DX2,DZ=DZ2
DIPOLE ARRAY WIDTH2,0.0006
 NODE 1,X1,-L2
 NODE 2,X1,-L2/2
 NODE 3,X1,0
 NODE 4,X1,L2/2
 NODE 5,X1,L2
 SEGMENT 1,1,2
 SEGMENT 2,2,3
 SEGMENT 3,3,4
 SEGMENT 4,4,5
 MODE 2,1,2
 MODE 3,2,3
 MODE 4,3,4
END ARRAY
XEQ
EXIT
```

Figure B4

PMM Input File for the FSS Step Source

```
TITLE 'FSS DIP'
NOPLOTFILE
ANGLE 0.,0.01
FREQUENCY 8.0,12.0,.01
DZ = 2.265
DX = 1.5
WIDTH =.75
X1 = .75
Z1 = 0.
SKEWED GRID DX,DZ=DZ
SLOT ARRAY WIDTH,0.0006
 NODE 1,-X1,Z1
 NODE 2,0,Z1
 NODE 3,X1,Z1
 SEGMENT 1,1,2
 SEGMENT 2,2,3
 MODE 2,1,2
END ARRAY
XEQ
EXIT
```

Figure B5

PMM Input File for the FSS Dip Source

```
CM: 8 FT TEST FIXTURE
CE: 8-12 GHZ SWEEP (PO + Frill Equiv Sol'n)
TO:
  F,F,F,F
  T,F,F
  F
  T,F,T,F,F,F
  F,F,F
  F,F,F,F
UN: UNITS IN FEET
  2
UF: SCALE FACTOR
  .5
FM: FREQUENCY SWEEP
  401,8.0,0.01
PD: FAR FIELD RETURN AT 0,0
  0.,0.,90.,0.
  T,90.
  0,0,0
PG: Plate geometry
  6
  4.5, 0.,0.
  2.5, 2.,0.
 -2.5, 2.,0.
 -4.5, 0.,0.
 -2.5,-2.,0.
  2.5,-2.,0.
BK: E-PHI POLARIZATION (H-POL)
  90.
LP: LINE PRINTER
  T
LD: DIPLOT OUTPUT
  T
XQ:
EN:
```

Figure B6

RCSBSC Input File for the Test Fixture

R0096115S9